Division of Biomedical Engineering

Department of Human Biology

University of Cape Town

Pulsatile Flow in Computational Modelling of Thrombosis in Cerebral Aneurysms

By

Student: Struan Hume

HMXSTR001

SUBMITTED TO THE UNIVERSITY OF CAPE TOWN

In fulfilment of the requirements for the degree:

MSc in Biomedical Engineering

Faculty of Health Sciences

UNIVERSITY OF CAPE TOWN

Submitted: 11/02/2019

The Centre for Research in Computational and Applied Mechanics (CERECAM)

Supervised by:

Dr. Malebogo Ngoepe
Department of Mechanical Engineering
Faculty of Engineering & the Built Environment
UCT

&

Associate Professor Wei Hua Ho
Department of Mechanical and Industrial Engineering
School of Engineering
UNISA

In Collaboration with:

Mr. Jean-Marc Tshimanga at UNISA

DECLARATION

I, Struan Hume, hereby declare that the work on which this dissertation/thesis is based is my original work (except where acknowledgements indicate otherwise) and that neither the whole work nor any part of it has been, is being, or is to be submitted for another degree in this or any other university.

I empower the university to reproduce for the purpose of research either the whole or any portion of the contents in any manner whatsoever.

Signature: Signed by candidate

Date: 11/02/2019

Abstract

Ngoepe and Ventikos have developed one of a growing number of computational models of thrombosis of cerebral aneurysms designed with consideration towards clinical use and research. Their model, amongst many others, utilizes computationally inexpensive steady flow conditions. However, pulsatile flow better characterizes blood flow in-vivo. Steady flow is an acceptable approximation of pulsatile flow from a fluid dynamics perspective, but there is no prior evidence suggesting whether it is an acceptable approximation when considering clot formation within a flowing environment. To this end a pulsatile flow model has been created in ANSYS® Fluent, and a function from Ngoepe and Ventikos's computational model that simulates the release of thrombin, a chemical responsible for clotting activation, has been implemented. The output of this simulation is compared to the output of an otherwise identical simulation utilizing Particle-Image-Velocimetry (PIV) validated steady flow conditions, to determine whether clotting outcome of Ngoepe and Ventikos's model, amongst others, differs with pulsatile flow

This experiment revealed that the concentration of thrombin required for clotting activation is generated in nearly half the time when utilizing pulsatile flow over steady flow. Pulsatile flow creates unsteady flow patterns within the aneurysm, which create an environment where less thrombin is carried out of the aneurysm and into the regular bloodstream. This indicates that steady flow approximations for realistic clotting in computational models of thrombosis of cerebral aneurysms without strong consideration for the effects of pulsatile flow are inaccurate.

Contents

Tables

Figures

1. Introduction

There is a growing number of computational models of thrombosis in cerebral aneurysms that have been designed with consideration towards clinical use and research. The primary limitation of these models arises from validation, since ethical concerns prevent the observation and documentation of the clotting of flowing blood *in-vivo* to which the output of these models can be compared. Validation must therefore be accomplished by examining groups of variables in isolation and proving that they operate together realistically. Many of these computational models rely on assumptions to simplify what would otherwise be computationally expensive and slow simulations. A common assumption for these models is that from a fluid-dynamics perspective, steady flow is an acceptable simplification of pulsatile flow, which characterizes blood flow *in-vivo*. There has, however, been no research that sought to address whether pulsatile flow has a significant effect on thrombus development by comparison to steady flow. There is therefore a need to compare the potential clotting outcomes of a computational model of thrombosis with and without the steady flow simplification.

2. Rationale

There is evidence suggesting that steady continuous flow is an acceptable approximation of pulsatile flow from a fluid dynamics perspective (Augsburger et al., 2009). However, there are limitations to this simplification that create uncertainty regarding the clotting process.

To date, mechanics of clot development and surrounding flow within a naturally-occurring cerebral aneurysm has not been quantified in-vivo. This is due to a variety of constraints related to ethics and technology. There are few instances where significant clotting within an aneurysm does not pose a serious health risk. Observation of a growing clot *in-vivo* is therefore rarely ethically acceptable. To accurately measure clotting and the surrounding flow conditions *in-vivo*, it is necessary that measurement tools do not interfere with blood flow. This means that such measurements must occur externally to the vessel. Magnetic resonance velocimetry is the best available *in-vivo* technology for specific blood velocity measurement per unit time, since it is the only technology that gives detailed flow information regardless of obstruction by the skull. While it could conceivably capture clot formation and the flow field around it, it requires invasive methods to measure the blood pressure accurately. Attempts have been made to evaluate the efficacy and output of intravascular devices using animal models, but the dissimilarity between animal and human physiology, the lack of prevalence of naturally occurring aneurysms in

animals, and the lack of standardization for testing has made these models an unreliable standard for comparison to human cerebral aneurysm models thus far (Bouzeghrane et al., 2009).

Attempts to model clot formation in-vitro have met a level of success with microfluidic devices. Li et al., for instance, used this method under steady flow conditions to successfully measure clot stability in relation to fibrin (Li et al., 2012). Experiments of this nature, however, have only been able to document clot formation, and don't provide insight into how velocity flow fields around the aneurysm interact with and develop the clot, and how that clot in turn interacts with and develops the flow field.

This shortcoming has been addressed to a degree, in recent research using particle image velocimetry (PIV) (Clauser et al., 2018). PIV experiments require transparent fluids for the microparticles to reflect light generated by the laser, so they can be detected in the camera images. Normal blood is opaque, but the experiment worked around this using platelet-rich blood plasma, which is both transparent, and the part of blood that is primarily responsible for the clotting process. Saline mixed with xanthane was combined with this plasma to accurately represent kinematic viscosity and density of the normal blood. This experiment was designed to measure the efficacy of flow diverters and is the first to incorporate biological components of flow into a high-accuracy in-vitro analysis of blood flow using PIV. This experiment however does not include pulsatile flow, and more crucially resulted in complete platelet embolization within seconds of the addition of clotting agents; an extreme departure of what occurs in-vivo.

Without a well-measured, and well-observed aneurysmal clot formation in-vivo or in-vitro, there is no conclusive consensus on how thrombi form in cerebral aneurysms under pulsatile flow conditions, and therefore there is no way to conclusively assume that thrombus formation in cerebral aneurysms under steady flow conditions is not significantly different. It is conceivable that periodically low flow rates give blood platelets opportunities to aggregate in ways that might not be possible in steady flow, as low flow rate and low shear rates are associated with increased rates of clot aggregation. Since blood flow is pulsatile in-vivo, it is reasonable to include it in a computational model of thrombosis in cerebral aneurysms designed for clinical use, provided that the computational cost is justified by the increase in accuracy.

3. Aim

To create a pulsatile flow function and determine whether the use of pulsatile flow in a computational thrombosis model results in a significantly different outcomes than steady flow.

4. Objectives

- Create a pulsatile flow function appropriate for implementation into a computational model of cerebral aneurysm thrombosis
- Implement the pulsatile flow function within a computational thrombosis model
- Compare thrombin concentration output of computational model with pulsatile flow to original steady flow output
- Confirm accuracy of steady flow model with outcomes of a PIV study
- Determine the efficacy of 2D simulations against the 3D PIV study outcome, and determine its accuracy for potential use in subsequent thrombosis studies

5. Literature Review

5.1. Cerebral Aneurysm Background

Cerebral aneurysms are the symptom of weaknesses in cerebral arteries, and are localized expansions in these blood vessels (Lawton et al., 2005). Cerebral aneurysms can rupture, causing subarachnoid hemorrhaging. Subarachnoid hemorrhaging can result in a hemorrhagic stroke, and possibly ischemic stroke via cerebral vasospasm.

5.2. Health Statistics

Cerebral aneurysm development and rupture are linked to a variety of risk factors, including genetic disorders and prevalent lifestyle diseases including hypertension, obesity, smoking and alcoholism. Cerebral aneurysm rupture is therefore a significant problem in any population where lifestyle diseases are common.

In 2016, the World Health Organization (WHO) reported global estimates made by the Global Health Observatory (GHO) of total alcohol consumption per capita, and prevalence of tobacco smoking for persons over the age of 15. In 2015, 1.1 billion of the world's population smoked tobacco, and in 2016 6.3 liters of pure alcohol were consumed per capita worldwide (GHO | … | Harmful use of alcohol, 2016; GHO

| … | Tobacco Smoking, 2016). Similar estimates were made in 2015 for the prevalence of obesity (body mass ≥ 30kg/m^2) and raised blood pressure (systolic blood pressure ≥ 140 and/or diastolic blood pressure ≥ 90) for persons over the age of 18. It was estimated that 22.1% of the world's population suffered from raised blood pressure in 2015, and more than 13.2% were obese during 2016 (GHO | Blood Pressure, 2015; GHO | Prevalence of obesity among adults…, 2016). Of the 56.4 million deaths in 2015, strokes accounted for 6.24 million; making it the 2nd leading cause of death in the world behind ischemic heart disease, which was responsible for 8.76 million deaths (GHO | Mortality and Global Health Estimates, 2016).

Statistics from South Africa taken in 2015 show that tobacco smoking was prevalent in 32.5% of males and 8% of females (Mortality and causes of death in South Africa …, 2015). In 2016, 9.3 liters of pure alcohol per capita was consumed. It was also estimated that raised blood pressure was prevalent in 26.9% of the population over 18 years old in 2015, and that 27% of the population was obese in 2016. Of 460 000 deaths in 2015, 23 000 were the direct result of cerebrovascular disease. This accounts for 5% of deaths that year, making cerebrovascular disease the third leading cause of natural death in South Africa during 2015.

5.3. Thrombosis in Cerebral Aneurysms

Thrombosis is the clotting of blood within the circulatory system and is tied closely to cerebral aneurysms (Lawton et al., 2005). According to multiple experts, thrombosis can occur in aneurysms regardless of whether rupture has occurred (Eller et al. 1986, Ishikawa et al. 2006, Calviere et al. 2011). With concern to aneurysms that have not ruptured, aneurysm stabilization can result from thrombosis, though it is also possible for thrombosis to increase an aneurysm's risk of rupture. There is consensus that this is the case for clots that occur naturally and with the aid of clot-inducing implanted devices (Ngoepe et al. 2018).

In standard physiological clotting, von Willebrand's factor (vWF) is expressed after a blood vessel is damaged, which allows platelets to attach to themselves to the subendothelial collagen layer of the blood vessel (Sakariassen et al., 1979, Stel et al., 1985). Platelet recruitment at the injury facilitates the healing process and prevents further extravasation of blood. The presence of blood cells coupled with hemodynamics influences the transportation and interaction of platelets with the vessel wall at the site of injury (Goldsmith and Karino, 1987). Platelets undergo four key stages during thrombogenesis (Kuwahara, 2002). These stages are deposition, activation, adhesion, and aggregation (2002). During deposition, when platelets initially deposit at the injury site, they extrude filaments on their surface. The

activation phase follows and involves the interaction between the GP Ib platelet receptors and vWF, resulting in a strong but reversible adhesion caused by the activation of the platelet's integrin $\alpha_{IIB}\beta_3$. The adhesion stage occurs with extensive growth of the platelet. During the adhesion stage interaction between vWF and activated integrin occurs, causing the formation of bond adhesions that are both irreversible and permanent. Platelets that have been activated promote further platelet recruitment, and a platelet plug is formed; this is the aggregation phase.

A coagulation cascade of reactions happens simultaneously to platelet activity. This coagulation cascade secures the platelet plug with the formation of a mesh consisting of fibrin. This platelet plug lasts for the duration of the healing process. The coagulation cascade process includes clot initiation, amplification, and propagation (Falati et al., 2002; Hoffman et al., 2004; Furie and Furie et al., 2005). Initiation involves a small amount of thrombin being formed when the injury site is exposed to and subsequently reacts with tissue factor (Orfeo et al., 2005). This results in amplification, where platelets, co-factor V, and co-factor VIII are activated via thrombin (Hoffman, 2004). The activation of these elements results in the propagation phase, where platelet recruitment and thrombin production is accelerated. Thrombin is responsible for platelet activation and is an important enzyme in the reaction that forms fibrin. Since many coagulation reactions occur on platelet membranes, platelets also support some key enzyme-related reactions that are responsible for fibrin mesh formation (Brinkman et al., 1994; Rosing et al., 1985).

There is a significant amount of evidence suggesting that there are differences between how thrombosis occurs in cerebral aneurysms and standard physiological thrombosis (Ngoepe et al, 2018). Factors concerning blood, such as the involvement and interactions of platelets and coagulation proteins, are largely the same in both processes (Davie and Ratnoff, 1964; Macfarlane, 1964; Furie & Furie, 1992; Falati et al., 2002; Hoffman, 2003). Deviation between thrombosis and physiological clotting occurs where the vascular endothelium and geometry-related local hemodynamics are concerned. These factors are related to the initiation phase of the coagulation cascade (Scanarini et al., 1978; Humphrey and Canham, 2000; Ngoepe, 2018).

Regardless of the process, tissue factor is a requirement to initiate the clotting reactions that cause the fibrin mesh to form. There is, however, much speculation that this tissue factor's origin differs for thrombosis in cerebral aneurysms (Bugge et al., 1996; Carmeliet et al., 1996; Toomey et al., 1996; Hoffman, 2003, 2004; Hoffman et al., 2006; Furie & Furie, 2008; Morel et al., 2011; Ngoepe et al., 2018). For clotting to initiate, tissue factor of the subendothelium must be exposed, which is typically the result of vessel wall injuries. This subendothelium, however, is absent for large parts of the vessel wall of

cerebral aneurysms (Humphrey & Canham, 2000). The damage to the endothelium within the aneurysm is connected to clot initiation (Sutherland et al., 1982). Studies have confirmed the existence of blood-borne tissue factor. This tissue factor circulates with blood and is involved with the processes behind clotting (Giesen et al., 1999; Hathcoc & Nemerson, 2004; Morel et al., 2006). There is consensus that this tissue-factor takes effect where there is abnormal stimulus, though there is speculation upon the actual role of the tissue factor (Butenas et al., 2005, 2009; Hoffman et al., 2006; Mann, 2006; Morel et al., 2006; Okorie et al., 2008). This is significant, because cerebral aneurysms create an environment where complex hemodynamics and varying shear rates are common (Peach et al., 2014).

The hemodynamics and platelet activity associated with aneurysmal environments are a significant departure from physiological clotting as well. Platelet activation can occur in abnormal blood flow patterns. Platelet activation can also occur in the high shear stress environment in stenosis that is caused by arterial diseases (Einav, 2004). Platelets are attracted to activated platelets, which results in platelet plug formation, and since recirculation is prominent within aneurysmal geometries, the mixture of coagulation proteins is prominent as well; resulting in an environment where the formation of fibrin is encouraged (Rayz et al., 2008; Di Achille et al., 2014; Peach T. et al., 2014; Ngoepe et al., 2016).

5.4. Cerebral Aneurysm Rupture Prevention

From a public health perspective, cerebral aneurysm rupture is being addressed indirectly through the promotion of healthy living. There is consensus that abstinence from tobacco smoking, moderation of the consumption of alcohol, and healthy dieting are each lifestyle choices that significantly reduce risk factor. Information sources found on the internet also serve as a prevention tool through societal awareness building.

Unruptured cerebral aneurysms are often asymptomatic and can be difficult to detect without the aid of brain CTA or MRA. These specialized scans are expensive and are not frequently used on patients who don't exhibit symptoms that necessitate their use. Consequently, cerebral aneurysms are often sighted when patients are being scanned for a different disease. Even though only a small proportion of aneurysms rupture, diagnosis often takes place only after rupture, which lowers odds of survival and quality of life considerably. If an unruptured cerebral aneurysm is found, it can be difficult to determine whether to surgically intervene due to the possibility of iatrogenic outcomes; especially when an aneurysm may be harmless (Wardlaw and White, 2000; Brisman et al., 2006). The opposite outcome is also possible, where ignoring an asymptomatic aneurysm could result in rupture, with potentially fatal outcomes for the patient. Consideration towards morphological factors such as location, size, shape,

bottle-neck factor, and aspect ratio are applied when gauging the necessity of treatment (Wiebers et al., 2003; Morita et al., 2005; Raghavan et al., 2005; Wiebers, 2005; Wermer et al., 2007; You et al., 2010; Ngoepe et al., 2018).

5.5. Cerebral Aneurysm Treatment

Common treatments for brain aneurysm treatment include surgical clipping, endovascular coiling, and flow diversion. Surgical clipping involves the removal of a section of skull for aneurysm access, so that a metal clip can be placed on the neck of the aneurysm to prevent blood from flowing into it. Endovascular coiling involves the insertion of a catheter into an artery. The catheter is guided through the body to the aneurysm to allow a wire to be pushed through it to the aneurysm, where it can coil and then clot; sealing the aneurysm from the artery. Flow diversion involves a similar procedure, where a catheter is guided through the body past an unruptured aneurysm, to deploy a flow diverter across the neck of the aneurysm, which in turn significantly reduces flow of blood to the aneurysm. Endovascular coiling is significantly less invasive than surgical clipping and is considered reasonably safe for patients with either ruptured or unruptured aneurysms (Brisman et al., 2006). The most dangerous part of endovascular coiling is the process of inserting the catheter into the aneurysm, which comes with the risk of accidental aneurysm rupture. Subsequently, flow diversion is an effective means of treatment where there is difficulty in treating using other methods (Becske et al., 2013).

5.6. Cerebral Aneurysm Treatment Outcomes

5.6.1. Surgical Clipping

One study compared survival outcomes of patients with one or more unruptured cerebral aneurysms who either had corrective surgical clipping, or no surgical intervention (Krisht et al., 2006). Outcomes were measured by two prior studies, one of which published by the International Study on Unruptured Intracranial Aneurysms. From these sources it used data on 116 surgically treated patients with 148 unruptured intracranial aneurysms, where follow-up was available in 108 patients. The study found that surgical clipping had a 0.8% mortality rate, and 3.4% permanent morbidity, suggesting surgical clipping has a superior outcome to non-intervention, which over a 10-year period has a mortality and severe morbidity of 7.5%.

5.6.2. Endovascular Coiling

An early study by Bavinzski et al. explored the formation of thrombi post-endovascular coiling, by investigating 17 aneurysms that were excised at autopsy (1999). Where fibrous tissue did not entirely

replace a clot, it was found that the clot could continue to grow and lead to aneurysm rupture. Another study found in 451 cases, aneurysms occluded fully in 55% of cases, partially occluded in 24% of cases, and didn't occlude in 18% of cases (Wiebers et al., 2003). In a review of aneurysm treatment by embolization of coils, morbidity, fatality, and bleeding prevention effectiveness were examined by a review that enrolled 1,379 patients with 1,621 aneurysms at minimum (Lanterna et al., 2004). Bleeding did not occur in any fully-occluded aneurysm after coil embolization. Bleeding was observed in partially occluded aneurysms of 10 mm or greater in size. A meta-analysis was performed of medical literature of endovascular treatment between January 2003 and July 2008, where 71 publications met all inclusion criteria, containing 5,044 patients with 5,771 unruptured aneurysms (Naggara, 2010). Amongst the aims was the estimation of treatment efficacy via results obtained immediately after treatment, and at follow-up. 86.1% of the unruptured aneurysms were fully-occluded or had a neck remnant immediately after treatment, and partial occlusion occurred in 10.3% of aneurysms. In 3.6% of cases, endovascular coiling failed. In 24.4% of patients, flow to the aneurysm was reestablished over a 0.4 to 3.2-year period in follow-up.

5.6.3. Flow Diversion

108 patients with either giant or wide-necked aneurysms were enrolled in a study to determine the safety and efficacy of flow diverters, of whom 73.6% of aneurysms occluded after 180 days (Becske et al., 2013). After a year, full occlusion was noted in 86.8% of aneurysms, neck remnants were noted in 5.5%, partial occlusion was noted in 5.5%. The absence of occlusion was noted in 2.2% of aneurysms. 5.6% of neurological outcomes were adverse.

101 unruptured aneurysms were enrolled in a study by establishing "the safety and efficacy in Pipeline endovascular devices and Silk stents" (Piano et al., 2013). 86% of aneurysms were fully-occluded six months after treatment. Of the 53 aneurysms examined a year after intervention, flow into the aneurysm was not reestablished in 61% of assessed specimens, where total reduction of the aneurysm was noted. Mortality and morbidity were both found to be 3%.

A meta-analysis of flow-diverter efficacy enrolled 1654 aneurysms from 29 studies and found that aneurysms fully-occluded in 76% of cases (Brinjiki et al., 2013). Occlusion was considered for different sized aneurysms. 76% of giant aneurysms were observed as having fully-occluded, as well as 74% of large aneurysms, and 80% of small aneurysms. Mortality and morbidity were 4% and 5% respectively.

5.7. Cerebral Aneurysm Thrombosis Model's

There are two major categories of cerebral aneurysm thrombosis models; thrombosis potential models, and direct thrombosis models. The difference between these categories is in their application of physiological models. Thrombosis potential models predict clotting outcomes by identifying conditions in flow that create potential for thrombosis to occur. Direct thrombosis models directly apply physiological models into their solution. Physiological models are used to mathematically define subsystems of the overall clotting process, and their inclusion allows direct thrombosis models to directly simulate the growth of a clot.

5.7.1. Thrombosis Potential Models

From arteriographic cerebral aneurysm data derived from five patients and an in vitro experiment involving a side-wall aneurysm model, a mathematical model was created that explores washout of angiographic contrast mediums from these aneurysms after the placement of a stent to predict the stability of thrombus formation (Sadasivan et al., 2002). The in-vitro experiment implemented an idealized aneurysm geometry with a pulsatile flow. Flow within the aneurysm was measured via arteriography in both the experiment and the patient-derived data and was further applied to generate grayscale curves. Based on the results, a mathematical model was developed and parameters concerning transport (convection and diffusion) within cerebral aneurysms and connected blood vessels were established.

One model explored increasing flow residence time within MRI-derived cerebral aneurysm geometries and correlated obtained wall shear stress with thrombus location; applying each as indicators for locations within intracranial aneurysms prone to thrombus development (Rayz et al., 2010). In this model, Navier-Stokes equations are approximated and solved via a finite volume method and describe the flow within the aneurysm and connected vessel. Pressure-velocity coupling is accomplished via a PISO scheme, and Navier-Stokes equations are solved with an implicit solver. Flow residence was monitored via the implementation of a virtual ink technique. The ink is represented by a passive scalar that is injected at the flow inlet of the geometry, and its transportation is tracked via a convection-diffusion equation. Computational results were compared with MRI results.

A computational fluid dynamics model was explored that employs hemodynamic properties and aneurysm geometry as indicators to predict thrombus formation. In this model, growth is considered spontaneous, and may result from an implanted device (De Sousa et al., 2015). Patient geometries derived from CTA are implemented in this model for cases of spontaneous thrombosis. For cases involving flow

diverters, digital subtraction angiography was employed. The implanted device (a flow diverter) is represented by a virtual grid, which was placed at the neck of the aneurysmal geometries. Navier-Stokes equations describes flow in the model. The governing equations are solved with a finite element approach. Aspect ratio of the aneurysm's dome and neck were compared, as were scan-calculated clot volumes, which appeared to be associated with one-another.

5.7.2. Direct Thrombosis Models

Local hemodynamics are combined with elements of physiological clotting in direct thrombosis models (Ngoepe et al., 2018). In these types of models, activity by blood platelets and surrounding biochemical reactions are directly accounted for. The growing clot's effect on the flow vector field is often accounted for in direct thrombosis models.

One of the earliest models of this kind was developed by Bedekar et al. Within realistic patient-derived aneurysm geometries, it considers hemodynamics with platelet activity and coagulation proteins. This model was the first to couple these factors together in a realistic patient-derived geometry from CTA. Hemodynamics are accounted for using Navier-Stokes equations. The shifting concentration of coagulation and platelet species are addressed with convection-diffusion-reaction equations. The platelet activity and coagulation protein reaction components of the model are built upon an integrated physiological model by Sorenson et al. (1999a, 1999b).

Another important computational model of thrombosis was developed by Ouared et al., and it is noteworthy for its development of approaches presented by thrombosis potential models (2008). Specifically, this model contributed a method where clot growth affects the field of flow, and inversely the flow field affects clot growth. This was accomplished via a shear regulation mechanism, where local shear rate is calculated, and clotting is initiated where shear rate drops below 100 s^{-1}. Clot growth occurs subsequently, and after formation the clot region becomes a solid through which flow cannot occur. Blood flow is modelled via the lattice Boltzmann numerical model for hydrodynamics, where forces resulting from particles movement and collision within a discrete space-time framework are calculated.

The model created by Ngoepe et al. builds further on Bedekar et al., where biochemical reactions and hemodynamics are accounted for in patient angiography-derived cerebral aneurysm geometries (Bedekar et al., 2005; Peach T. W. et al., 2014; Ngoepe & Ventikos, 2016; Ngoepe et al., 2018). This model includes flow diverter placement, and incorporates the model feature developed by Ouared et al., where clot growth affects the flow field, and inversely the flow field affects clot growth via the alteration of porosity

and permeability in the clot region (Ouared et al., 2008; Ngoepe & Ventikos, 2016; Ngoepe et al., 2018). For the incorporation of porosity and permeability, adjusted momentum and continuity are used in this model. This allows the model to determine the difference between blood plasma, and the growing clot. To track the expanding clot's surface, a level-set method is employed. The start of clotting is controlled by the threshold of shear rate, and the concentration of thrombin is linked to the clot's growth. Subsequently, Ngoepe et al.'s model can be used to determine clotting outputs before and after flow diverter placement. Ngoepe et al. have indicated, however, that there is a need for further model validation before it may be applied in clinical studies (Ngoepe & Ventikos, 2016; Ngoepe et al., 2018). Navier-Stokes equations account for the flow behavior of the modelled blood, which in this model is considered Newtonian, incompressible, and of constant density & velocity. An effective diffusivity equation alters protein transportation within the area of clot development. This process results from all but two biochemical reaction and reaction rate equations that were derived from earlier models by Hockin et al. and Wagenvoord et al. (2002, 2006; Ngoepe and Ventikos, 2016; Ngoepe et al., 2018).

5.8. Pulsatile Flow

Pulsatile flow most accurately represents the periodic nature of blood flow *in-vivo*, and there are many models that directly link the volume and mass flow rate of blood to the rate of thrombin generation, fibrin deposition, and growth of thrombi (Rana et al., 2016). Despite this, many computational cerebral aneurysm thrombosis models do not account for the effects of pulsatile flow.

Pulsatile flow is characterized by flow with periodic variations and was first derived by John R. Womersley (Womersley, 1955). Consequently, it is known as Womersley's flow.

$$U(y) = -P_z' \frac{1}{j\rho\omega}\left[1 - \frac{J_0(j^{3/2}\alpha y)}{J_0(j^{3/2}\alpha)}\right]$$

In this characterization of flow, fluid is assumed to be Newtonian, homogenous, and incompressible. The fluid vessel is assumed to be a rigid and circular tube, where motion is laminar, parallel to the tube's axis, and axisymmetric. The assumed boundary conditions are that there is no-slip condition at the tube walls, and that the function is axisymmetric at the center of the tube. Finally, gravity is assumed to be negligible.

The primary driver behind the fluid is the pressure gradient P_z', which is defined as a periodic function. The shape of the flow profile changes based on the Womersley number α, a dimensionless constant. Where $\alpha \leq 2$, pulse is quasi-static with a parabolic profile. Higher values mean that viscous forces are

dominant along the tube wall, and inertial forces are dominant along the tube's central axis, resulting in a flatter velocity profile.

5.9. Particle Image Velocimetry

Particle image velocimetry (PIV) is used to obtain instantaneous velocity vectors of a flowing fluid. It stands as one of a few methods that can be used as a validation tool for computational flow models, (Mulder et al., 2009).

This is accomplished by mixing microparticles into the fluid, which are captured in several images taken in rapid succession by a fixed camera as they flow through a transparent geometry. For these particles to be sufficiently visible by comparison to the surrounding fluid, a laser is directed at the transparent geometry in a dark environment, so that light reflects from the microparticles. For the camera to register the exact location of the microparticles, substances must be added to the fluid so that it matches the refractive index of the transparent geometry. A program is then employed to compare the images in pairs, determining the distance travelled of microparticles and relating this distance to the time at which each image was taken, resulting in detailed velocity vectors. Since high-quality microparticles effectively mimic the flow of the fluid they are mixed with, this method is generally considered highly accurate (Adrian and Westerweel, 2011).

6. Methodology

6.1. Computational Approach

Flow is considered as Newtonian and incompressible for simplicity. It is governed by the following Navier-Stokes derived transport equations:

Mass Conservation Equation:

$$\nabla \cdot \boldsymbol{U} = 0$$

Momentum Conservation Equation:

$$\rho \frac{\partial \boldsymbol{U}}{\partial t} + \rho \boldsymbol{U} \cdot \nabla \boldsymbol{U} + \nabla \mathrm{P} = \mu \nabla^2 \boldsymbol{U}$$

Where $\boldsymbol{U}$ is a sample velocity vector, ρ is the fluid density, μ is the dynamic fluid viscosity, and P is pressure.

ANSYS® Academic Research Fluent, Release 19.1 is used to implement the pulsatile flow and steady flow simulations into a model developed by Ngoepe and Ventikos (2016). An idealized geometry developed in previous research is employed in SpaceClaim and meshed using Ansys MESHING (Mulder, 2009). The mesh is imported into ANSYS® Fluent. User-defined functions (UDF) define the pulsatile flow boundary conditions within ANSYS® Fluent. A model of thrombus growth is incorporated via a user defined function (UDF), which describes the thrombin release function boundary condition, Ansys Post-Processer is used to analyse simulation results.

6.2. Defining Pulsatile Flow for ANSYS® Fluent

User-Defined Function's (UDF)'s are required for many transient flow cases in ANSYS® Fluent and accommodate most flow-types that are not included in the standard framework. ANSYS® Fluent UDF's work using C-code and use a limited library designed specifically for use in ANSYS® Fluent. Therefore, definitions of pulsatile flow were explored to determine functions compatible with implementation into an ANSYS® Fluent UDF, and *in vivo* blood flow for cerebral aneurysms. To this end, appropriate *in-vivo* data for cerebral aneurysms was sought out as both an input, and confirmation tool for each pulsatile flow function.

6.2.1. Womersley Flow

Pulsatile flow in cylindrical vessels is traditionally characterized by Womersley flow. The Womersley Flow equation outputs longitudinal flow velocity. The input variables of Womersley Flow are time, and pressure-gradient. The Womersley Flow equation adjusts based on the distance of a radial coordinate from the longitudinal axis of flow within the vessel being evaluated.

It was initially deemed appropriate to simplify Womersley flow, so it could be directly supplied to ANSYS® Fluent with a UDF, but it was later determined that blood flow data within cerebral arteries containing simultaneous consecutive measurements for pressure-gradient and velocity over time could not be found in literature. With a lack of input variables and no way feasible way to measure the accuracy of the velocity output, use of the Womersley Flow velocity function could not be justified.

6.2.2. In-Vivo Data-Derived Fourier Transforms

6.2.2.1. In-Vivo Simultaneously Measured Pressure and Velocity Data

Data for simultaneously measured velocity and pressure within arteries is available in literature. Ferns et al. provides data acquired in cerebral arteries with aneurysms present, measured with an intra-arterial guidewire (Ferns et al., 2010). A chart from this study specifically provides graphs of data measured from

the internal carotid artery at the cervical level, proximal to the aneurysm, within the aneurysm, and distal to the aneurysm. This chart also provides x-ray's next to each graph, providing insight into the vessel geometry at the sites where measurement took place. Because the measurements at the internal carotid artery at the cervical level were surrounded by an approximately cylindrical geometry, the data at this site was considered suitable as an input for the mathematical model, since limited geometrical complexity limits factors to consider when evaluating the overall model's output. As such, Figure 1 and Figure 2 were digitized using Graph Grabber v2.0 for data points to be used in the model. 143 data points were extracted from the original velocity graph, and 145 data points were extracted from the original pressure graph.

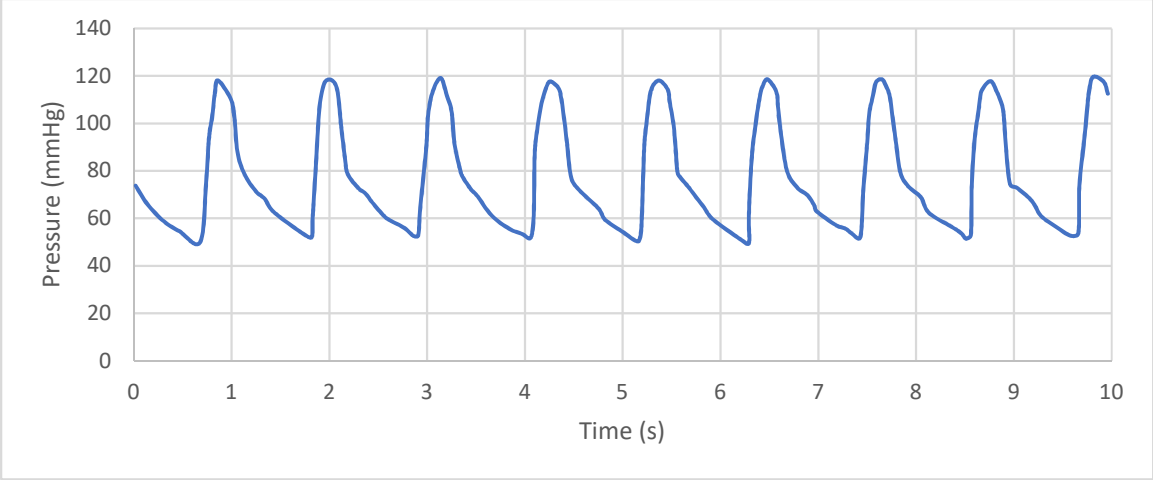

Figure 1: Pressure vs Time Data at Cervical Level of Internal Carotid Artery (obtained from Ferns et al.)

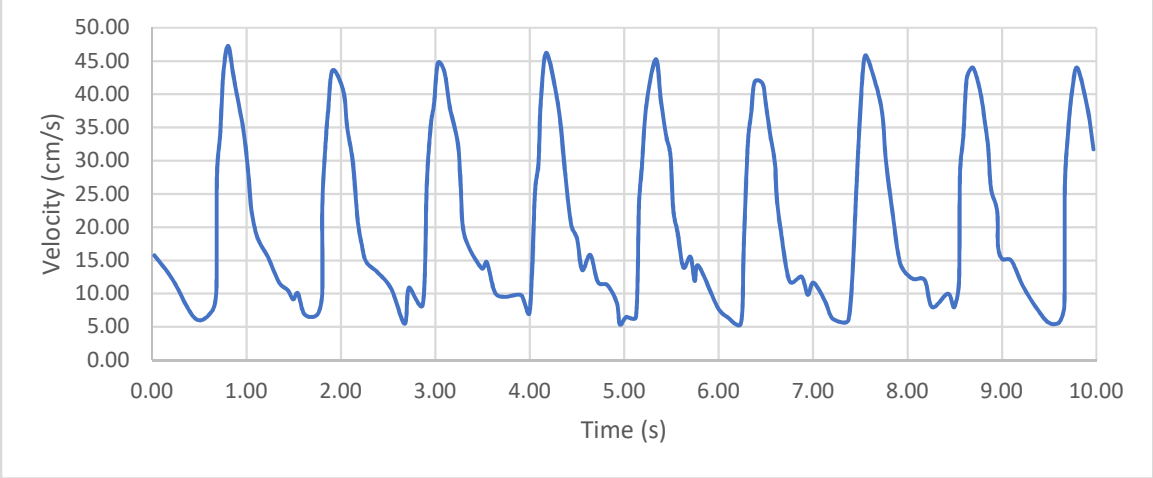

Figure 2: Velocity vs Time Data at Cervical Level of Internal Carotid Artery (obtained from Ferns et al.)

Curve fitting methods were explored to simplify the data into periodic functions that could be used to define the inlet and outlet boundaries of an ANSYS® Fluent flow simulation. Specifically, Fourier Transforms were chosen to accomplish this, because the data appears to represent a composite sinusoid. To accomplish this, the least-squares method was employed using Microsoft Excel, where the sum of least squares of a Fourier Transform and corresponding data was calculated, and the Microsoft Excel Solver tool was used to reduce this number as much as possible by adjusting the amplitude, frequency, and phase shift of each of the three sinusoids, as well as the vertical shift of the Fourier Transform overall. The pressure Fourier Transform illustrated in Figure 3 has an average deviation of 15.20% from the original pressure data points. The velocity Fourier Transform illustrated in Figure 4 has an average deviation of 24.20%.

Pressure Fourier Transform:

$$P(t) = -30.44 * \sin(2\pi(0.89)t - 13.19) + 2.96 * \sin(2\pi(-1.93)t + 0.5) + 1.39 * \sin(2\pi(15.86)t - 2.01) + 75.07$$

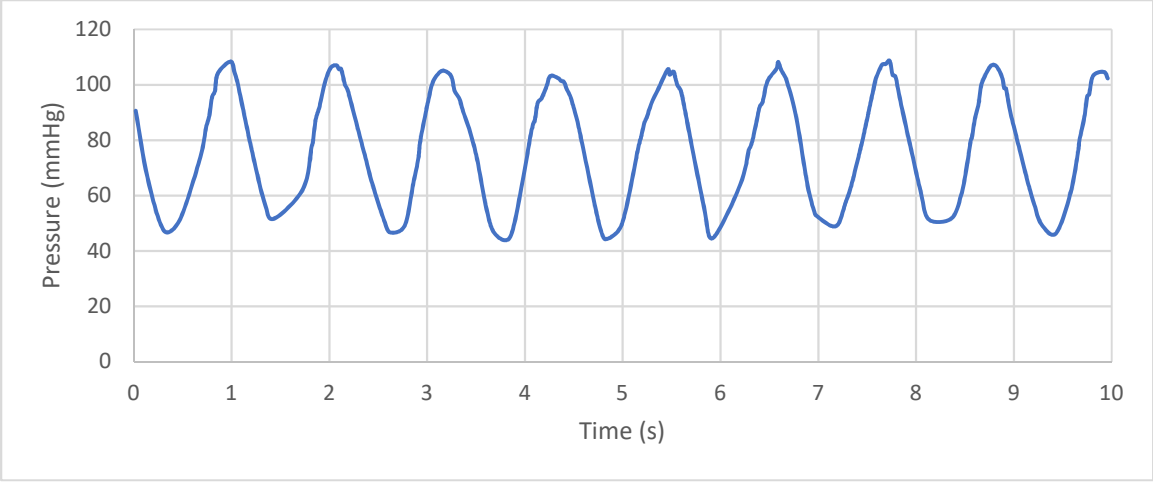

Figure 3: Pressure vs Time Fourier Transform-Based Reconstruction

Velocity Fourier Transform:

$$U(t) = -15.49 * \sin(2\pi(0.89)t - 12.84) + 9.42 * \sin(2\pi(-1.78)t - 1.61) + 0.27 * \sin(2\pi(18.44)t - 1.44) + 19.59\text{p}$$

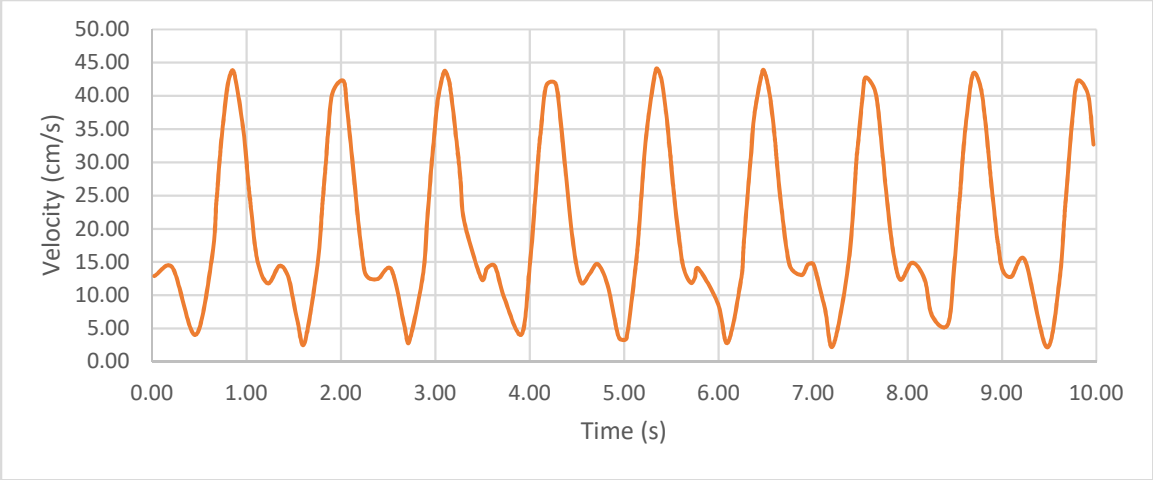

Figure 4: Velocity vs Time Fourier Transform-Based Reconstruction

6.3. Aneurysm Wall Thrombin Release Function

To account for the effect of pulsatility on biochemical protein transportation, the variable thrombin release model was applied at the aneurysm wall. When using this function, differences in rate of clotting and areas of clotting between the steady and pulsatile flow simulations can be obtained without the more complicated biochemistry and porosity functions, which bring unnecessary computational complexity to the scope of the project.

The function is as follows:

$$F(t) = 10^{-9}\left(200sin\left(\frac{\pi}{600}t - \frac{\pi}{2}\right) + 200\right)$$

The sinusoid is a simplified version of Wagenvoords thrombin generation model applied in Ngoepe et al.'s cerebral aneurysm clotting model. Originally Ngoepe et al. used curve fitting methods with exponential functions to reproduce Wagenvoords model for their research, but there was difficulty applying this function in the UDF for the Ansys FLUENT framework, and it was found that applying a sinusoid was more feasible given the scope of the project. It represents roughly the shape of exponential function around 200s when thrombin concentration increases sharply, and excludes the long period of low thrombin generation beforehand as can be seen in Figure 5.

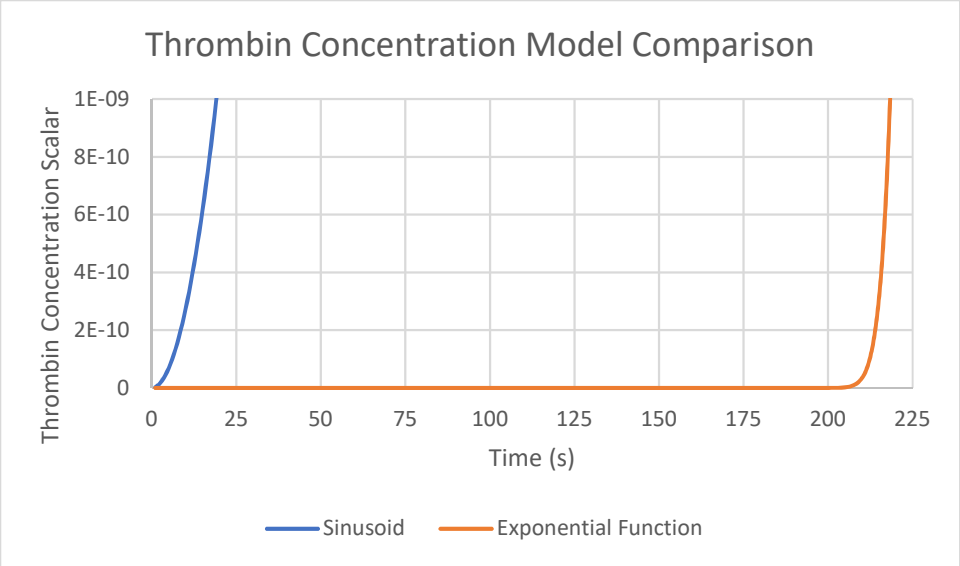

Figure 5: Sinusoidal vs Exponential Thrombin Concentration Functions

The concentration of thrombin released is represented in part by a user-defined scalar (UDS), whose value the aneurysm wall thrombin release function effects by changing the value of the UDS diffusion near the aneurysm wall (ANSYS® Academic Research Fluent 19.1, Help System, Fluent Theory Guide Chapter 1: Basic Fluid Flow | 1.3. User-Defined Scalar (UDS) Transport Equations | 1.3.1. Single Phase Flow).

The aneurysm wall function relates to the diffusion value in the following way:

$$F(t) = \Gamma_k \frac{\partial \phi_k}{\partial x_i} \cdot \vec{n}$$

Where:

ϕ_k Arbitrary Scalar

Γ_k Diffusion coefficient

$\vec{n}$ Vector normal to the surface

It is presumed that conditions for clotting exist once the thrombin concentration scalar ϕ_k reaches a value between 1e-9 and 100.

See section 6.6.11. for the overall UDS equation for the simulation.

6.4. Ideal Aneurysm Geometry

The idealized cerebral aneurysm geometry was recreated using ANSYS® Fluent supporting geometry software. It consists of a cylindrical semi-circle that represents a cerebral artery, topped by a sphere that represents the aneurysmal sac. This is illustrated in Figure 6.

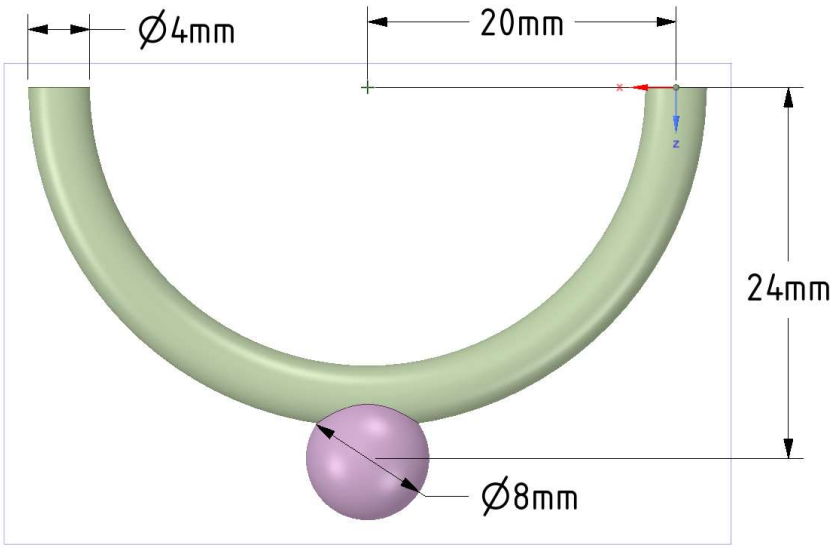

Figure 6: Ideal Aneurysm Geometry

Two fluid zones and three boundaries were labelled in the meshing phase. The fluid zones include the aneurysm zone, and the artery zone. The boundaries include the vessel wall, the inlet, and the outlet.

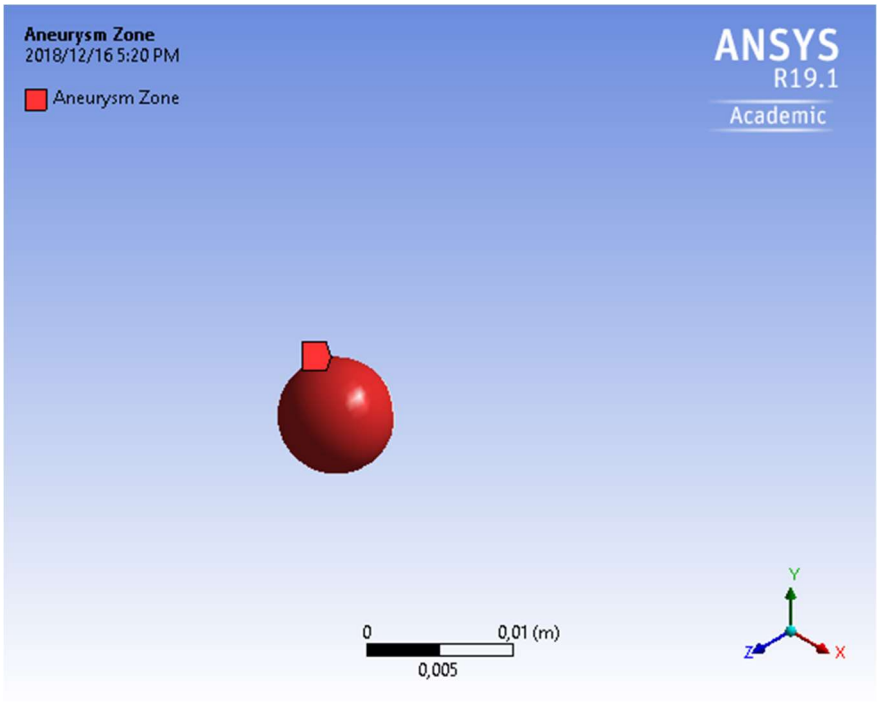

Figure 7: Aneurysm Zone

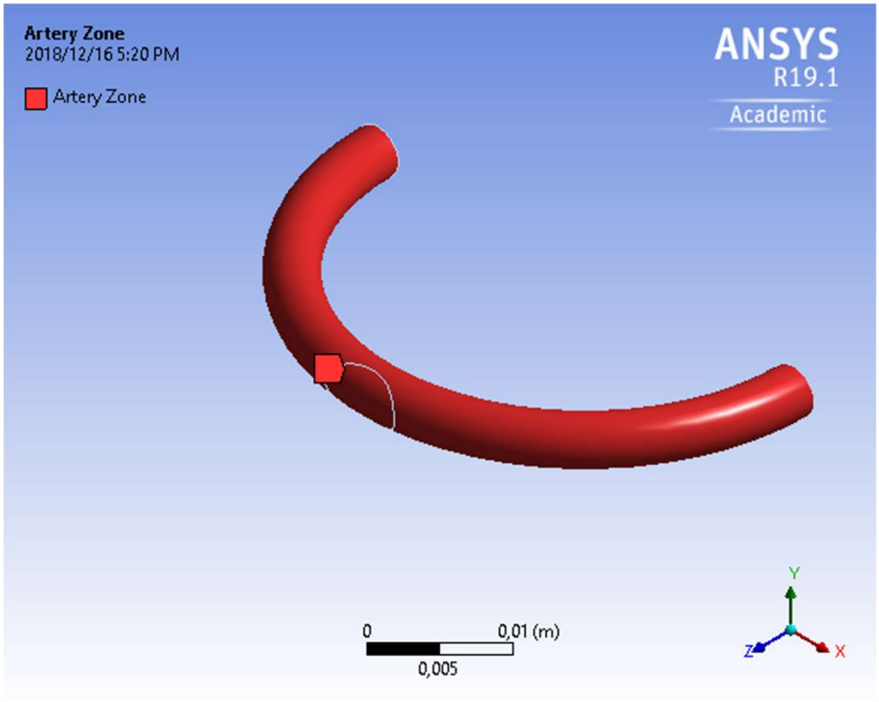

Figure 8: Artery Zone

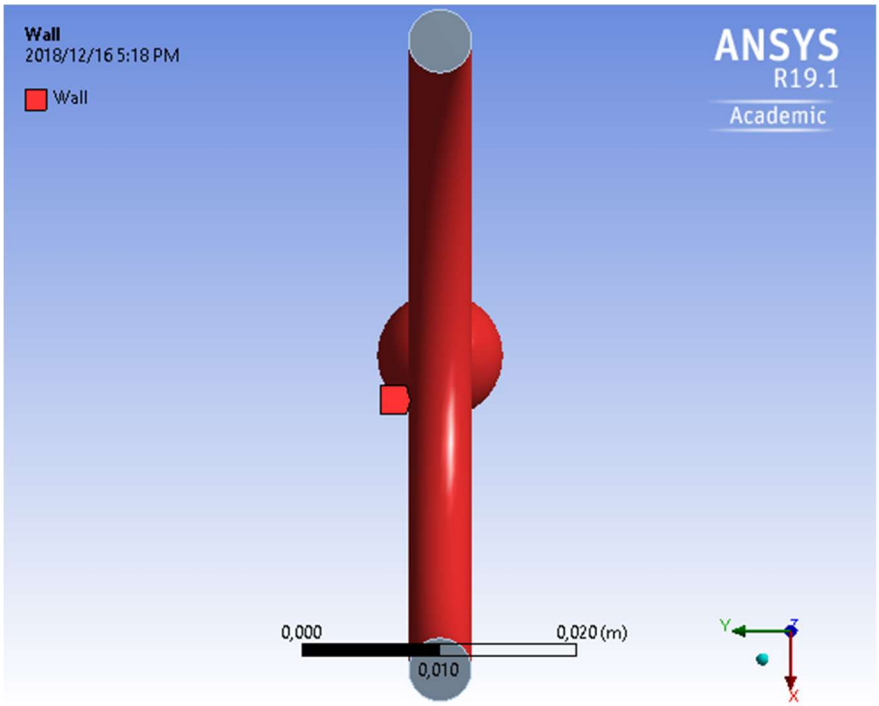

Figure 9: Wall

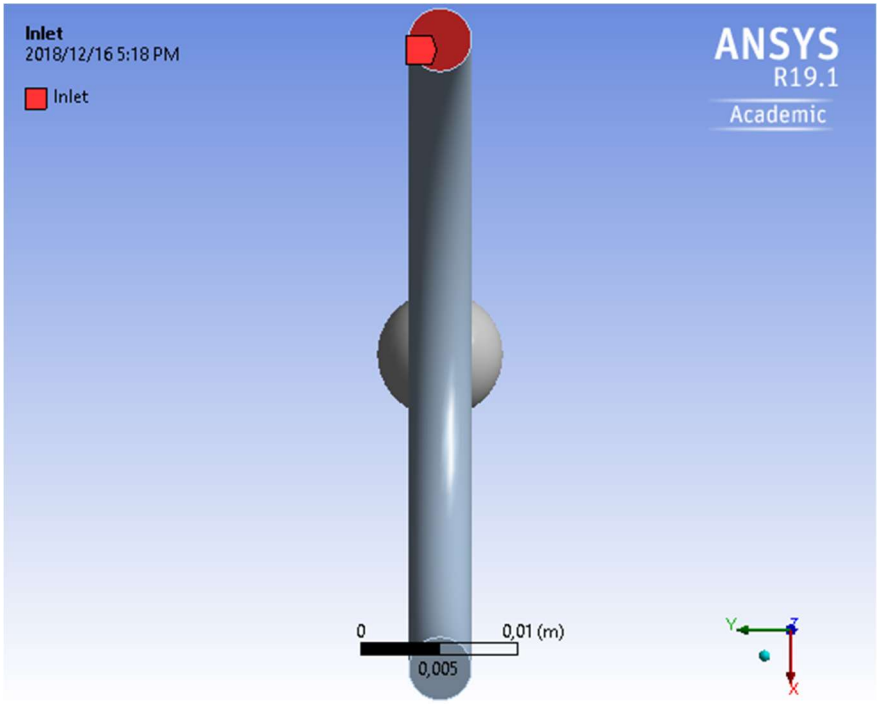

Figure 10: Inlet

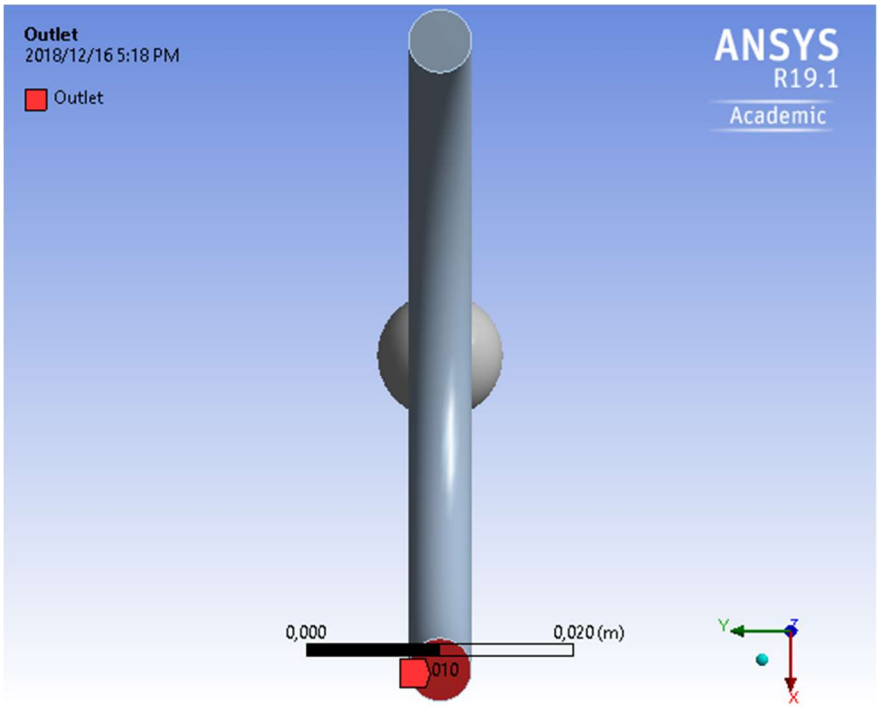

Figure 11: Outlet

6.5. Meshing

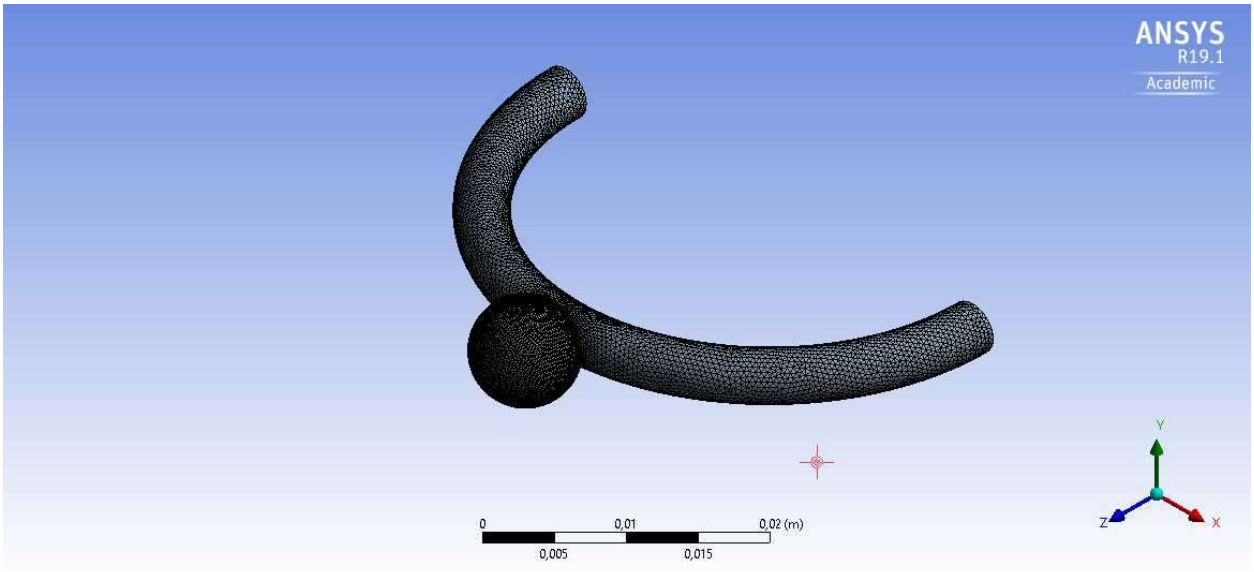

Figure 12: Mesh

To ensure accuracy, the mesh was made as fine as possible, so that optimal accuracy could be achieved, particularly within the aneurysm zone. A mesh was therefore created with 401283 elements and 108346 nodes. Global default element size was set to 4.1630e-004 m. The mesh deviates from this default size at the aneurysm zone, and at the edge connecting the aneurysm zone and the artery zone, where element size is set as 2.0815e-004 m. Inflation of five layers is employed at the walls of the aneurysm zone and artery zone, as well as the connection between the two zones. The skewness and orthogonal quality statistics of the mesh are displayed in table 1.

A mesh independence study is conducted and detailed in section 6.10.1.1.

Mesh Metric	Min	Max	Average	Standard Deviation
Orthogonal Quality	0.20572	0.99411	0.80471	0.12233
Skewness	3.4424e-5	0.79628	0.19372	0.12384

Table 1: Mesh Orthogonal Quality and Skewness

6.6. ANSYS® Fluent Pressure-Based Solver Functionality and Settings

6.6.1. Least-Squared Cell-Based Gradient Evaluation

Gradients are necessary for a variety of tasks, including defining scalar values at cell faces, computing velocity derivatives, and computing secondary diffusion terms. A least-squared cell-based gradient is applied to accomplish this, because its accuracy is comparable to other options, and it is less computationally expensive. Within this method the solution is presumed to exhibit linear variation between $c0$ and ci across δr_i; the center of the cell in question, the center of an adjacent cell, and the vector distance between the two, respectively (ANSYS® Academic Research Fluent 19.1, Help System, Fluent Theory Guide: Chapter 21: Solver Theory | 21.3. Discretization | 21.3.3. Evaluation of Gradients and Derivatives).

Considering all cells surrounding a cell in question, the system is defined as the following:

$$[J](\nabla\phi)_{c0} = \Delta\phi$$

Where:

$[J]$ The coefficient matrix which is purely a function of geometry

When solving the minimization problem for a system in a least-squares sense, the objective is to determine the cell gradient. This is done using the Gram-Schmidt process, which decomposes the coefficient matrix and yields a matrix of weights for each cell. So, for each face of cell c0, three

components of weights $({W^x}_{i0}, {W^y}_{i0}, {W^z}_{i0})$ is produced (ANSYS® Academic Research Fluent 19.1, Help System, Fluent Theory Guide Chapter 21: Solver Theory | 21.3. Discretization | 21.3.3.4. Least Squares Cell-Based Gradient Evaluation).

The cell center gradient can afterwards be computed by multiplying by the difference vector $\Delta\phi = (\phi_{ci} - \phi_{c0})$:

$$(\phi_x)_{c0} = \sum_{i=1}^{n} {W^x}_{i0} \cdot (\phi_{ci} - \phi_{c0})$$

$$(\phi_y)_{c0} = \sum_{i=1}^{n} {W^y}_{i0} \cdot (\phi_{ci} - \phi_{c0})$$

$$(\phi_z)_{c0} = \sum_{i=1}^{n} {W^z}_{i0} \cdot (\phi_{ci} - \phi_{c0})$$

6.6.2. General Scalar Transport Equation

A control-volume-based technique is applied in ANSYS® Fluent to convert a general scalar transport equation to a numerically solvable algebraic equation. This technique entails the integration of the transport equation about a control volume, outputting a discrete equation representing the conservation law based upon control-volume (ANSYS® Academic Research Fluent 19.1, Help System, Fluent Theory Guide Chapter 21: Solver Theory | 21.2. General Scalar Transport Equation: Discretization and Solution).

The general scalar transport equation is as follows:

$$\int_V \frac{\partial \rho\phi}{\partial t} dV + \oint \rho\phi\, \vec{v} \cdot d\vec{A} = \oint \Gamma_\phi \nabla_\phi \cdot d\vec{A} + \int_V S_\phi dV$$

Where:

ρ	density
$\vec{v}$	velocity vector
Γ_ϕ	diffusion coefficient of ϕ
∇_ϕ	gradient of ϕ
S_ϕ	Source of ϕ per unit volume

6.6.3. Standard Gradient Limiter

In second-order upwind discretization schemes, gradient limiters are employed to prevent oscillations that could appear in the solution flow field that are not representative of the true solution behavior (ANSYS® Academic Research Fluent 19.1, Help System, Fluent Theory Guide Chapter 21: Solver Theory | 21.3. Discretization | 21.3.4. Gradient Limiters). The simulation utilizes the default standard gradient limiter. This limiter applies the minimum modulus to limit solution overshoots and undershoots on the cell faces (ANSYS® Fluent 19.1, Help System, Fluent Theory Guide Chapter 21: Solver Theory | 21.3. Discretization | 21.3.4.1. Standard Limiter).

6.6.4. Momentum Equation

The steady-state integral-form of the momentum equation for the pressure-based solver is represented as follows (ANSYS® Academic Research Fluent 19.1, Help System, Fluent Theory Guide Chapter 21: Solver Theory | 21.4. Pressure-Based Solver).

$$\oint \rho \vec{v}\, \vec{v} \cdot d\vec{A} = -\oint p\boldsymbol{I} \cdot d\vec{A} + \oint \bar{\bar{\tau}} \cdot d\vec{A} + \int_V \vec{F}\, dV$$

Where:

$\boldsymbol{I}$ Identity Matrix

$\bar{\bar{\tau}}$ Stress Tensor

$\vec{F}$ Force Vector

6.6.4.1. PRESTO! Pressure Interpolation Scheme

This project will later be expanded to include clotting in the form of porous media. Because the default second-order pressure interpolation scheme does not accommodate porous media, the PRESTO! (PREssure Staggering Option) scheme was selected for the simulation, as it is recommended for flows involving porous media. PRESTO! applies a discrete continuity balance for a "staggered" control volume about the face to compute the face pressure (ANSYS® Academic Research Fluent 19.1, Help System, Fluent Theory Guide Chapter 21: Solver Theory | 21.4. Pressure-Based Solver | 21.4.1.1. Pressure Interpolation Schemes).

6.6.5. PISO Pressure-Velocity Coupling

Face mass flux J_f is applied to the continuity equation to derive an additional condition for pressure, resulting in a pressure-velocity coupling. Of the pressure-velocity coupling algorithms offered in ANSYS® Fluent, PISO was deemed the most applicable for the problem, as it is highly recommended for all transient flow calculations, especially when a larger timestep is desired. The PISO algorithm is based on a predictor-corrector approach, and is part of the SIMPLE family of algorithms (ANSYS® Academic Research Fluent 19.1, Help System, Fluent Theory Guide Chapter 21: Solver Theory | 21.4. Pressure-Based Solver | 21.4.3.1.3. PISO).

The SIMPLE algorithm family of algorithms employs a relationship between corrections of velocity and pressure to impose mass conservation and acquire the pressure field (ANSYS® Academic Research Fluent 19.1, Help System, Fluent Theory Guide Chapter 21: Solver Theory | 21.4. Pressure-Based Solver | 21.4.3.1.1. SIMPLE).

If the momentum equation is solved with a guessed pressure field p^*, the face flux J_f^* is as follows:

$$J_f^* = \hat{J}_f^* + d_f(p_{c0}^* - p_{c1}^*)$$

The continuity equation cannot be satisfied by J_f^* alone, so a correction J_f' is added to output the corrected face flux J_f, and in turn satisfy the continuity equation

The corrected face flux is as follows:

$$J_f = J_f^* + J_f'$$

Where the correction J_f' is as follows:

$$J_f' = d_f(p_{c0}' - p_{c1}')$$

Where:

p' cell pressure correction

The coefficient d_f is defined as a function of $\overline{(a_P - \sum_{nb} a_{nb})}$ for the SIMPLEC and PISO algorithms. Modified in this way, the correction equation accelerates convergence where pressure-velocity coupling deters the acquisition of a solution (ANSYS® Academic Research Fluent 19.1, Help System, Fluent Theory Guide Chapter 21: Solver Theory | 21.4. Pressure-Based Solver | 21.4.3.1.2. SIMPLEC).

The corrected face flux equation is substituted into the discrete continuity equation to yield a discrete equation for the pressure correction p' in the cell (ANSYS® Academic Research Fluent 19.1, Help System, Fluent Theory Guide Chapter 21: Solver Theory | 21.4. Pressure-Based Solver | 21.4.3.1.1. SIMPLE).

The pressure-correction equation is as follows:

$$a_P p' = \sum_{nb} a_{nb} p'_{nb} + b$$

The net flow rate into the cell, b, is as follows:

$$b = \sum_{f}^{N_{faces}} J_f^* A_f$$

The pressure-correction equation is solved using the algebraic multigrid method, and afterwards the cell pressure and face flux are corrected.

The corrected cell pressure is as follows:

$$p = p^* + \alpha_p p'$$

Where:

α_p under-relaxation factor for pressure.

The corrected face flux equation is as follows:

$$J_f = J_f^* + d_f(p'_{c0} - p'_{c1})$$

The corrected face flux J_f satisfies the discrete continuity equation identically during each iteration.

6.6.5.1. Neighbor Correction

The PISO algorithm moves the repetitive calculations involved in SIMPLE/SIMPLEC into the solution stage of the pressure-correction equation, and after one or more of these added PISO loops, the momentum and continuity equations are better satisfied by the corrected velocities. This process is referred to as neighbor correction. The PISO solver neighbor correction setting is set to the default value 1, and is instrumental in decreasing the number of iterations required for convergence in transient problems (ANSYS® Academic Research Fluent 19.1, Help System, Fluent Theory Guide Chapter 21: Solver Theory | 21.4. Pressure-Based Solver | 21.4.3.1.3.1. Neighbor Correction).

6.6.5.2. Skewness Correction

An iterative process like neighbor correction, called skewness correction, is used to calculate the components of the pressure-correction gradient along the cell-faces. In this process, after an initial solution is computed for the pressure-correction equation, the pressure-correction gradient is recalculated and applied to update the mass flux corrections. This is useful, because for meshes with a measure of skewness, mass flux upon the cell face has a rough relationship with pressure corrections at the adjacent cells, and component values of the pressure-correction gradient along cell-faces are not defined in advance. Skewness correction allows for easier convergence with distorted meshes (ANSYS® Academic Research Fluent 19.1, Help System, Fluent Theory Guide Chapter 21: Solver Theory | 21.4. Pressure-Based Solver | 21.4.3.1.3.2. Skewness Correction).

Due to the average skewness of the mesh being a satisfactory, the default skewness correction value of 1 was selected.

6.6.5.3. Skewness-Neighbor Coupling

Skewness-neighbor coupling was enabled for the PISO scheme. This coupling causes the PISO algorithm to apply iterations for skewness correction for each iteration of neighbor correction, allowing for a more accurate face mass flux correction based on the normal pressure correction gradient than an uncoupled solution (ANSYS® Academic Research Fluent 19.1, Help System, Fluent Theory Guide Chapter 21: Solver Theory | 21.4. Pressure-Based Solver | 21.4.3.1.3.3. Skewness - Neighbor Coupling).

6.6.6. Under-Relaxation

6.6.6.1. Under-Relaxation of Variables

Within the pressure-based coupled algorithm, explicit under-relaxation of variables is applied for momentum and pressure. Under-relaxation of variables is valuable for achieving convergent behaviour in a solution, because the set of equations solved in the pressure-based coupled algorithm are nonlinear. Specifically, under-relaxation of variables dampens change in the variable ϕ for each solution iteration in the following form (ANSYS® Academic Research Fluent 19.1, Help System, Fluent Theory Guide Chapter 21: Solver Theory | 21.4. Pressure-Based Solver | 21.4.4.1. Under-Relaxation of Variables):

$$\phi = \phi_{old} + \alpha \Delta \phi$$

Where:

ϕ_{old} old ϕ value from previous iteration

α under-relaxation factor

$\Delta\phi$ computed change in ϕ

Per default ANSYS® Fluent solver settings, only two variables have an under-relaxation factor less than 1. Pressure has an under-relaxation factor of 0.3, and momentum has an under-relaxation factor of 0.7 per program defaults.

6.6.6.2. Under-Relaxation of Equations

All equations solved using the pressure-based solver have an under-relaxation factor associated with them, because the update of variables at each iteration is controlled by implicit relaxation to stabilize convergence behavior of outer nonlinear iterations (ANSYS® Academic Research Fluent 19.1, Help System, Fluent Theory Guide Chapter 21: Solver Theory | 21.4. Pressure-Based Solver | 21.4.4.2. Under-Relaxation of Equations).

At a location specific timestep, the under-relaxation factor α changes the discretized equation for scalar ϕ to the following:

$$\frac{a_p\phi}{\alpha} = \sum_{nb} a_{nb}\phi_{nb} + b + \frac{1-\alpha}{\alpha} a_p\phi_{old}$$

6.6.7. Time Advancement Algorithm

The flow simulation is time dependent, and in this case ANSYS® Fluent utilizes the following discretized form of the generic transport equation (ANSYS® Academic Research Fluent 19.1, Help System, Fluent Theory Guide Chapter 21: Solver Theory | 21.4. Pressure-Based Solver | 21.4.5. Time-Advancement Algorithm).:

$$\int_V \frac{\partial \rho\phi}{\partial t} dV + \oint \rho\phi\, \vec{v} \cdot d\vec{A} = \oint \Gamma_\phi \nabla_\phi \cdot d\vec{A} + \int_V S_\phi dV$$

Where:

$\frac{\partial \rho\phi}{\partial t}$ conservative form of transient derivative of transported variable ϕ

ρ density

$\vec{v}$ velocity vector

$\vec{A}$ surface area vector

Γ_ϕ diffusion coefficient of ϕ

∇_ϕ gradient of ϕ

S_ϕ Source of ϕ per unit volume

ANSYS® Fluent pressure-based solver uses an implicit discretization of the transport equation. By default, the convective diffusive and source terms are evaluated at time level $n+1$ (ANSYS® Academic Research Fluent 19.1, Help System, Fluent Theory Guide Chapter 21: Solver Theory | 21.4. Pressure-Based Solver | 21.4.5. Time-Advancement Algorithm).

$$\int_V \frac{\partial \rho \phi}{\partial t} dV + \oint \rho^{n+1} \phi^{n+1} \vec{v}^{n+1} \cdot d\vec{A} = \oint \Gamma_\phi{}^{n+1} \nabla_\phi{}^{n+1} \cdot d\vec{A} + \int_V S_\phi{}^{n+1} dV$$

Time discretization error is determined by the first-order temporal discretization and the time advancement scheme.

The default first-order iterative time advancement scheme is employed in the simulation, wherein equations are solved iteratively for each time-step until the criteria for convergence are met (ANSYS® Academic Research Fluent 19.1, Help System, Fluent Theory Guide Chapter 21: Solver Theory | 21.4. Pressure-Based Solver | 21.4.5.1. Iterative Time-Advancement Scheme).

6.6.8. User-Defined Scalars (UDS)

A UDS is included in the simulation to accommodate the variable thrombin concentration, where the entire mesh is the solution zone, and the flux function employed is the mass flow rate. This UDS is solved by ANSYS® Fluent in the same fashion it solves the transport equation for a scalar (ANSYS® Academic Research Fluent 19.1, Help System, Fluent Theory Guide Chapter 1: Basic Fluid Flow | 1.3. User-Defined Scalar (UDS) Transport Equations | 1.3.1. Single Phase Flow).

Where ϕ_k is an arbitrary scalar, and convective flux is computed with mass flow rate, ANSYS® Fluent uses the following equation:

$$\frac{\partial \rho \phi_k}{\partial t} + \frac{\partial}{\partial x_i}\left(\rho u_i \phi_k - \Gamma_k \frac{\partial \phi_k}{\partial x_i}\right) = S_{\phi_k} \qquad k = 1, \dots, N$$

Where:

Γ_k Diffusion coefficient

S_{ϕ_k} Source Term supplied for each N scalar

$\frac{\partial \rho_{\ k}}{\partial t}$ Unsteady flow term

$\rho u_i \phi_k$ Convection term

$\Gamma_k \frac{\partial \phi_k}{\partial x_i}$ Diffusion term

Inlet diffusion is disabled, so the UDS transport equation does not operate at the inflow and outflow boundaries.

6.6.9. Algebraic Multigrid Solver (AMG)

The ANSYS® Fluent pressure-based implicit solver relies upon an AMG to accelerate the convergence. This operates by correcting a series of progressively coarser grid levels. The guiding principle in this method is that global error present on a fine mesh can be represented on a coarse mesh as local error. This helps to greatly reduce the number of iterations and CPU time to reduce global error and reach convergence, since these expenses decrease exponentially for coarser meshes (ANSYS® Academic Research Fluent 19.1, Help System, Fluent Theory Guide Chapter 21: Solver Theory | 21.7. Multigrid Method | 21.7.1.1. The Need for Multigrid).

6.6.9.1. Multigrid Concept

A discretized set of linear equations is defined as follows (ANSYS® Academic Research Fluent 19.1, Help System, Fluent Theory Guide Chapter 21: Solver Theory | 21.7. Multigrid Method | 21.7.1.2. The Basic Concept in Multigrid).

$$A\phi_e + b = 0$$

Where:

ϕ_e Exact Solution

A Fine level operator

Prior to convergence, the approximate solution ϕ has a defect d.

$$A\phi + b = d$$

A correction ψ is applied so that the exact solution becomes the following:

$$\phi_e = \phi + \psi$$

Substituting this into the discretized set of linear equations yields:

$$A(\phi + \psi) + b = 0$$

$$A\psi + (A\phi + b) = 0$$

Which applied to the approximate solution equation yields the correction equation.

$$A\psi + d = 0$$

If the fine level relaxation scheme has damped local errors adequately, the correction will be more successfully solved on the subsequent coarse level.

6.6.9.2. Coarse Grid Correction

Corrections are solved via the processes of restriction and prolongation. Restriction is the transfer of a defect from the fine level to the coarse level. Corrections are then computed, and prolongation begins, in which the corrections are transferred back to the fine level from the coarse level (ANSYS® Academic Research Fluent 19.1, Help System, Fluent Theory Guide Chapter 21: Solver Theory | 21.7. Multigrid Method | 21.7.1.3. Restriction and Prolongation).

The coarse level correction equation is the following:

$$A^H\psi^H + Rd = 0$$

Where:

A^H Coarse level operator

R Restriction operator

The fine level solution is as follows:

$$\phi^{new} = \phi + P\psi^H$$

Where P is the prolongation operator. For AMG, the prolongation operator is given as the transpose of the restriction operator (ANSYS® Academic Research Fluent 19.1, Help System, Fluent Theory Guide Chapter 21: Solver Theory | 21.7. Multigrid Method | 21.7.3.1. AMG Restriction and Prolongation Operators).

$$P = R^T$$

The coarse level operator A^H is constructed via a Galerkin approach. A new defect associated with the corrected fine level solution must be substituted when transferred back to the coarse level. The expression A^H is derived as follows (ANSYS® Academic Research Fluent 19.1, Help System, Fluent Theory Guide Chapter 21: Solver Theory | 21.7. Multigrid Method | 21.7.3.2. AMG Coarse Level Operator).

$$Rd^{new} = 0$$

$$R(A\phi^{new} + b) = 0$$

$$R(A(\phi + \mathrm{P}\psi^H) + b) = 0$$

$$RAP\psi^H + R(A\phi + b) = 0$$

$$RAP\psi^H + Rd = 0$$

Yielding:

$$A^H = RAP$$

This coarse level operator effectively is a summation of diagonal and off-diagonal blocks for all cells of a group in the fine grid, which forms the diagonal block of the group's course cell.

6.6.9.3. V Multigrid Cycle

The V multigrid cycle is the default multigrid cycle used for the algebraic multigrid. It is a recursive procedure that is employed at each level of the multigrid. The default V cycle employed for the algebraic multigrid consists of four steps. These steps are as follows (ANSYS® Academic Research Fluent 19.1, Help System, Fluent Theory Guide Chapter 21: Solver Theory | 21.7. Multigrid Method | 21.7.2.1. The V and W cycles):

1. The current grid level solution is restricted to the next coarser grid level.
2. One multigrid cycle is performed, and error on the coarse grid is reduced

3. Corrections computed on the coarse grid is interpolated back to the fine grid using prolongation. This causes some high-frequency error.
4. Iterations, called post-relaxation sweeps, are performed on the fine grid to remove the high-frequency error.

6.7. Materials

Human blood is a Non-Newtonian fluid, and its density and viscosity change based upon a variety of factors. Blood is considered Newtonian in this model as the vessels are sufficiently large for such an assumption to hold. To this end, blood is modelled as having a density of $\rho = 1000\,kg/m^3$ and a viscosity $\mu = 0.004\,kg/ms$, and is considered laminar and incompressible.

6.8. Pulsatile Flow Boundary Conditions

To implement pulsatile flow into the aneurysm clotting model, periodic boundary flow conditions were first explored in ANSYS® Fluent. Periodic flow boundary conditions exist within Ansys Fluent, however the conditions required for their use do not apply to the problem being explored; where the translational periodicity boundary condition option requires heat transfer in the simulation, and the rotational periodicity boundary condition option is only applicable in simulations involving rotating parts. Given this, pulsatile flow functions are required to define the boundary conditions for pulsatile flow in ANSYS® Fluent.

6.8.1. Velocity Inlet

A velocity inlet boundary condition was implemented using the velocity Fourier Transform function as the velocity magnitude. The direction of the velocity magnitude was considered normal to the inlet boundary. Supersonic/initial gauge pressure was set as 0 since this option is ignored by ANSYS® Fluent for subsonic velocities, and the reference was defaulted to absolute since the option has no bearing on the result so long as the inlet remains stationary. Velocity is uniform across the surface of the inlet, and behaves like a flow plug at this boundary. This flow plug redistributes shortly after leaving the inlet, and more closely resembles Poiseuille Flow prior to reaching the aneurysm zone shown in Figure 7.

ANSYS® Fluent uses velocity components and boundary condition scalar quantities to calculate inlet mass flow rate and momentum fluxes.

It computes the mass flow rate of an adjacent fluid cell to the velocity inlet boundary as follows:

$$\dot{m} = \int \rho \vec{v} \cdot d\vec{A}$$

Where only the component of velocity normal to the face of the control volume is employed in computing the inlet mass flow rate.

6.8.2. Pressure Outlet

A pressure outlet boundary condition was implemented, where the gauge pressure was set to the pressure Fourier Transform function in the UDF, and the backflow was set normal to the outlet boundary.

For incompressible flow, the pressure at the face of the outlet boundary P_f is defined as follows:

$$P_f = \frac{P_c + P_e}{2}$$

Where

P_c Interior cell pressure neighboring the exit face f

P_e Specified exit pressure

6.8.3. Artery Wall

The rigid artery wall is idealized to limit computational complexity, and is a no-slip, no-shear, stationary and inelastic surface.

6.8.4. Aneurysm Wall

The aneurysm wall is identical to the artery wall, except that the User-Defined Scalar Boundary Value is set to a variable thrombin concentration. This value represents the damaged tissue of aneurysm and is meant to activate clotting functions in the aneurysm fluid zone that are not included in this experiment.

6.9. Steady Flow Boundary Conditions

Steady flow conditions were established in a separate simulation. The steady flow clotting simulation is identical to the pulsatile flow clotting simulation, save for the velocity inlet boundary and pressure outlet, which use steady flow conditions. The velocity magnitude for the velocity inlet is 0.23 m/s, and the gauge pressure for the pressure outlet is 11100 Pa. The velocity magnitude and gauge pressure are the average of the velocity and pressure Fourier Transforms, respectively, over one full wavelength and three significant figures.

6.10. Calculation Settings

6.10.1. Steady Flow

The steady flow simulation has a timestep size of 0.01, and 30,000 timesteps to calculate a total flow time of 5 minutes. This timestep size was selected since it was small enough to collect a large amount of datapoints, but large enough that the simulation ran efficiently, and with residuals of less than 1e-6. The convergence criteria for the steady flow simulations are that continuity, x-velocity, y-velocity, & z-velocity residuals all fall below 0.001 each timestep.

6.10.1.1. Grid Independence

A grid independence study was carried out for the steady-flow simulation. Due to the transient nature of the problem, pursuing grid independence through reduction of residuals is an unreliable method in isolation, so to reduce the mesh size of the aneurysmal geometry and retain sufficient accuracy, the simulation was repeated for coarser meshes, and probe values were compared to previously measured probe values of the maximum cell/node mesh. To accomplish this, three probes were employed; a surface probe across the inlet, a line probe parallel to the x-axis across the surface of the outlet, and another line probe through the center of the aneurysmal geometry parallel to the z-axis. These probes output pressure and velocity values at each time-step using the area-weighted average of the nodes surrounding the elements that their coordinates resided within. This was repeated for 1000 time-steps for each mesh, where each mesh used roughly half the elements of the previous mesh. Fully developed flow was achieved around 1.5 seconds for each case.

Mesh Information		
Elements in Mesh	Nodes	Global Element Size
401283 (Baseline)	**108346**	**4.163e-4 m**
203369	59201	5.35e-4 m
100071	31725	7.03e-4 m

Table 2: Grid Independence Study: Mesh Information

Standard Deviation from Baseline Mesh						
	Inlet		Center-Axis Line-Probe		Outlet Line-Probe	
Elements in Mesh	Velocity	Pressure	Velocity	Pressure	Velocity	Pressure
401283 (Baseline)	**0%**	**0%**	**0%**	**0%**	**0%**	**0%**
203369	0%	0.03%	2.61%	0.02%	3.87%	0.02%
100071	0%	0.03%	4.89%	0.01%	4.32%	0.03%

Table 3: Grid Independence Study: Standard Deviation

Pressure changes minimally with adjustment of mesh size. Velocity changes more significantly with coarser mesh size, though only deviates from the baseline mesh with a significantly coarser mesh that has a quarter of the number of elements.

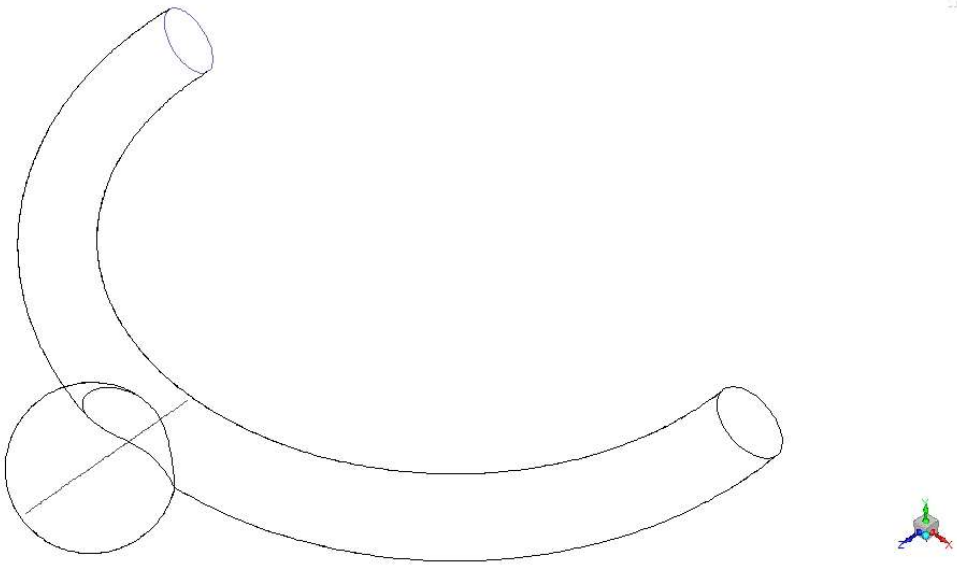

Figure 13: Center Line-Probe

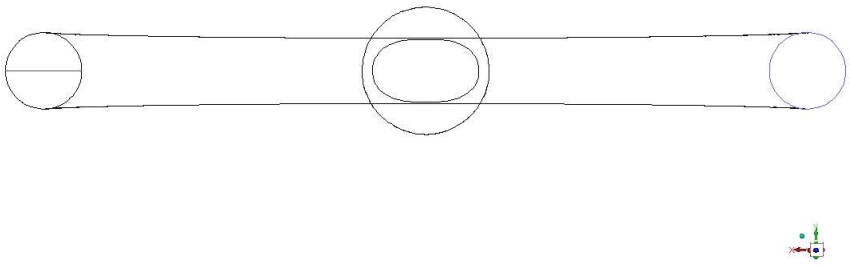

Figure 14: Outlet Line-Probe

6.10.2. Pulsatile Flow

The convergence criteria for the pulsatile simulations are that continuity, x-velocity, y-velocity, & z-velocity residuals all fall below 0.001 each timestep. However, in a transient simulation with many flow variables, residuals may not be representative of accuracy. Given this, the initial 10 seconds of the simulation was first run with a timestep sized such that at the average velocity of the velocity Fourier Transform, the maximum cell-convective Courant number within the aneurysm zone was less than 1. To accomplish this, the aneurysm zone element size of 2.0815e-4 m was divided by the average velocity 0.23 m/s to yield the rounded timestep of 0.001s.

Using this timestep, a comparison was made between the output UDS values along the centerline probe at four specific times, illustrated in Figure 15. This timestep was small and would result in a long simulation. A timestep of size 0.01 was desirable since it was small enough to collect a large amount of data points, but large enough that the simulation could run more efficiently should it be accurate. The process was repeated with this timestep size to gauge its accuracy.

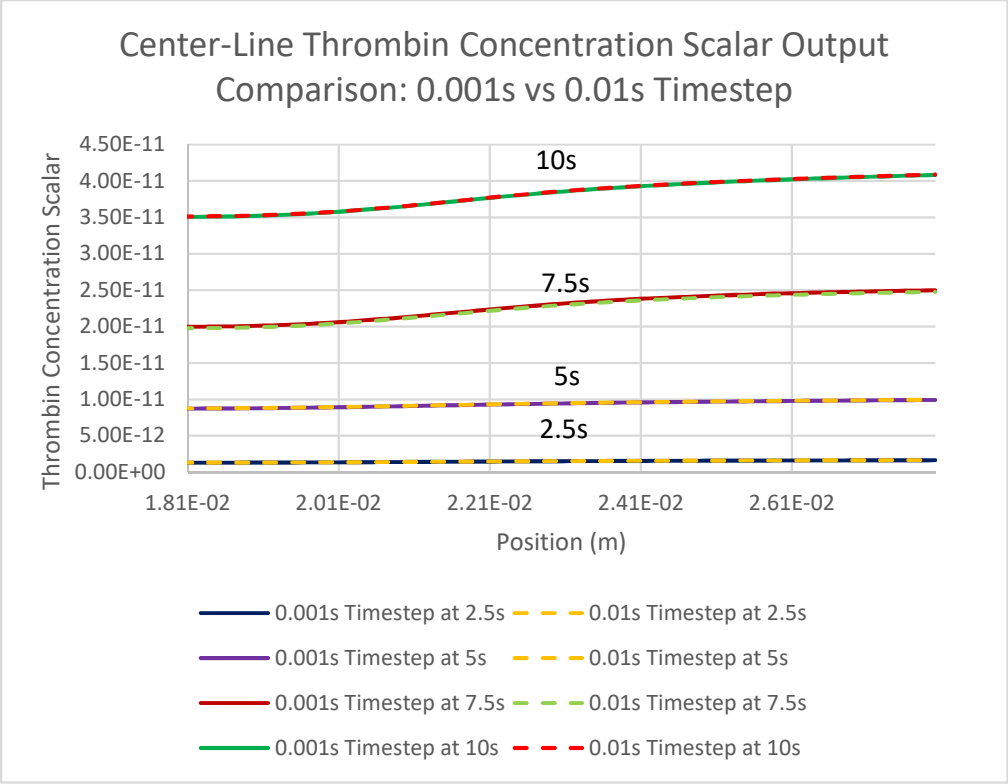

Figure 15: Pulsatile Flow Simulation Centerline Probe Thrombin Concentration Scalar Output: 0.001s Timestep vs 0.01s Timestep

There is a small offset between scalar values at different times along the centerline probe in Figure 13. However, as shown in Figure 16, the average thrombin concentration scalar value across the aneurysm geometry is nearly identical for each simulation, and the 0.01s timestep data has a standard deviation of 0.91%

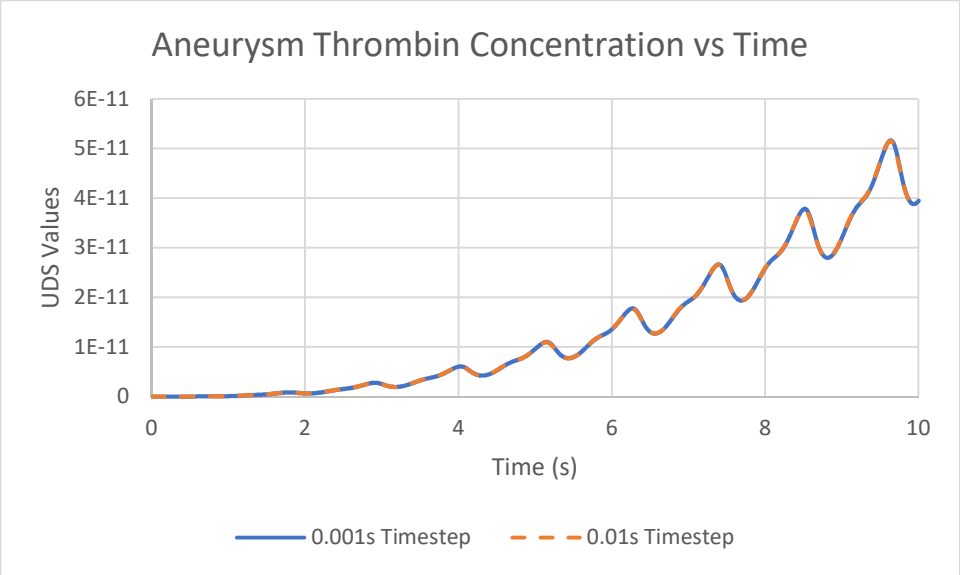

Figure 16: Average Aneurysm Thrombin Concentration Timestep Comparison

A timestep size of 0.01s was therefore used in the pulsatile flow simulation. 30,000 timesteps are calculated to produce a total flow time of 5 minutes.

6.11. Data Postprocessing

6.11.1. Flow Comparison

In post-processing, line-probes and contour planes are used to measure the differences in flow-profile and thrombin concentration scalar values between the steady-flow and pulsatile-flow simulations. Five line-probes are employed, shown in Figures 17 & 18.

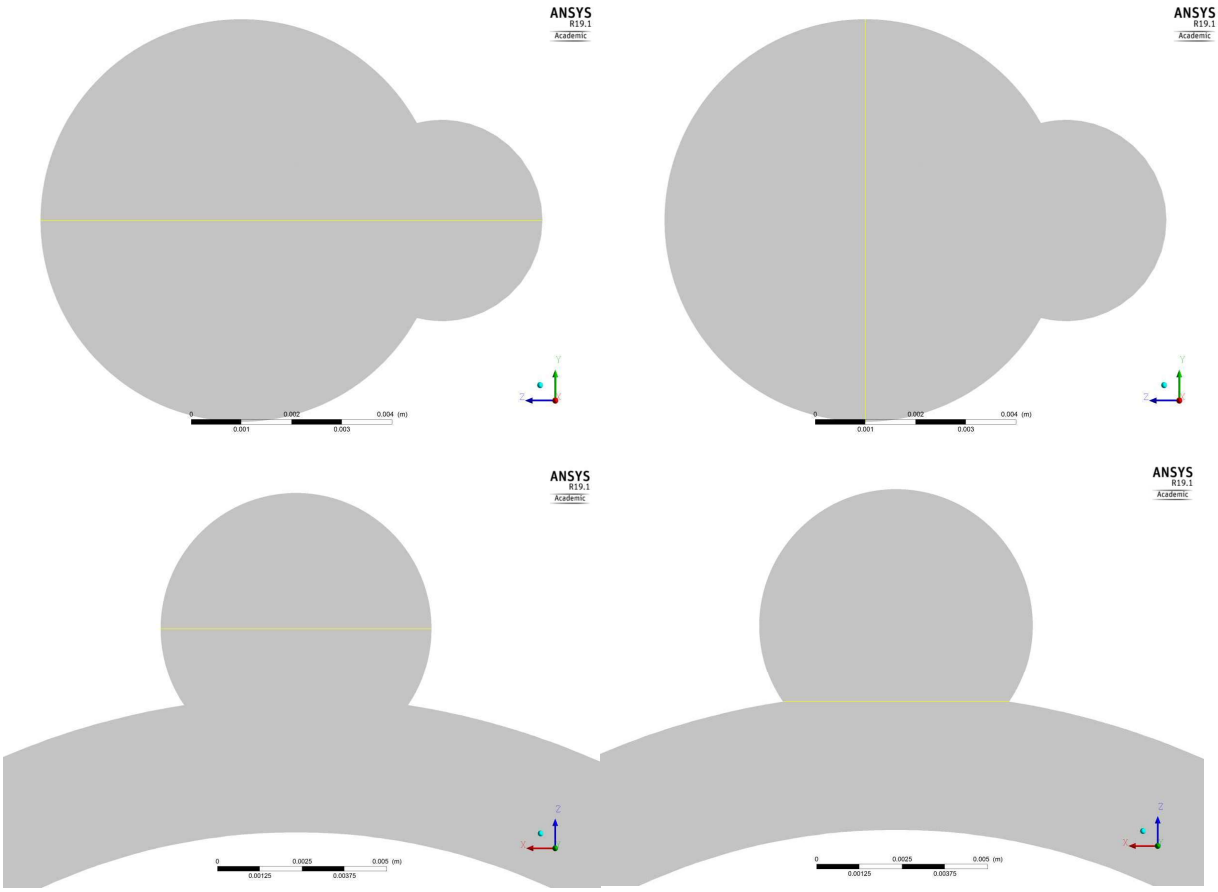

Figure 17: Probe A (Top Left), Probe B (Top Right), Probe C (Bottom Left), Probe D (Bottom Right)

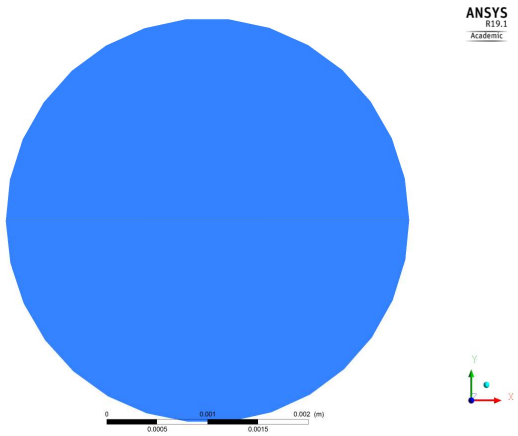

Figure 18: Outlet Line-Probe

Two planes, shown in Figures 19 and 20 are used to visualize contours of pressure, velocity, and scalar values.

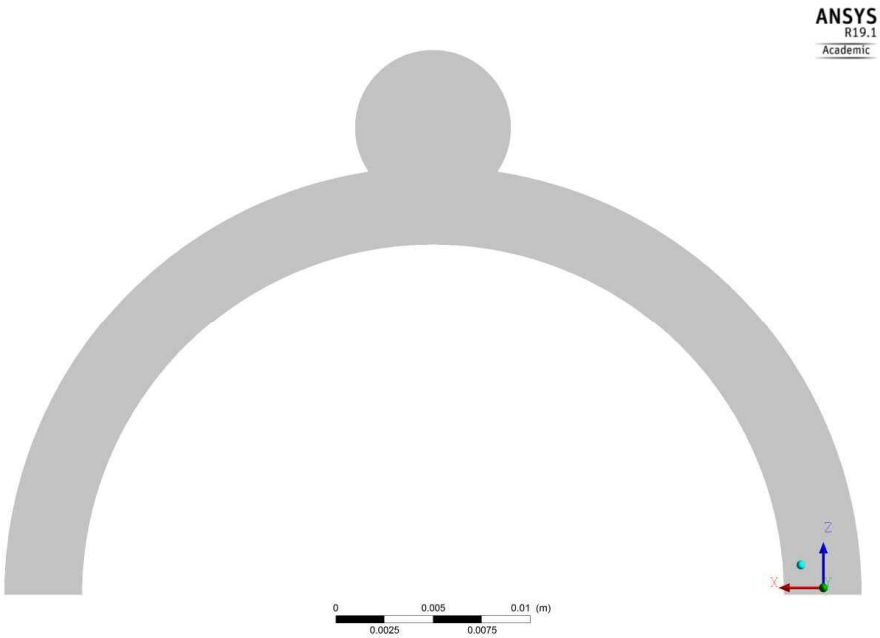

Figure 19: X-Z Post-Processing Plane

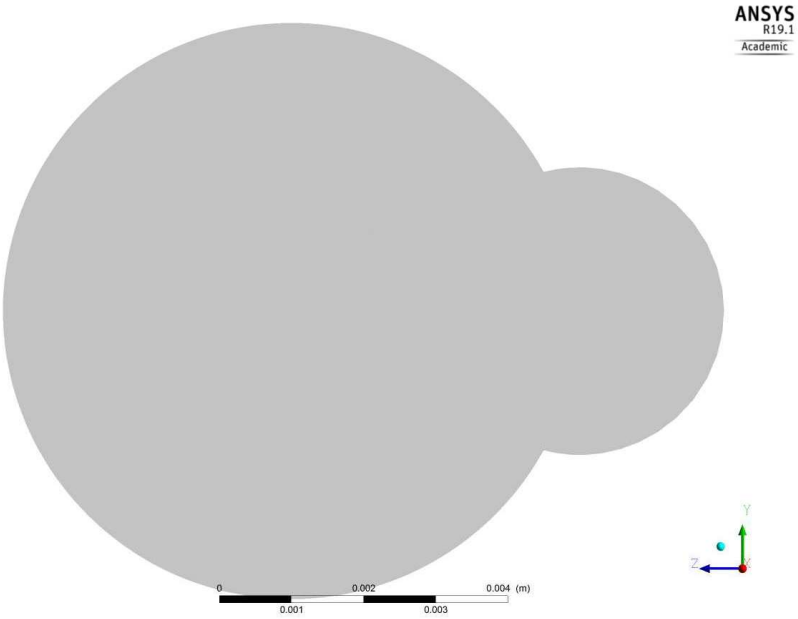

Figure 20: Y-Z Centerline Post-Processing Plane

Finally, two 3d probes cover the aneurysm zone shown in Figure 7, and the artery zone shown in Figure 8. Case data is saved every 0.1s in each simulation. Comparisons are made at the timesteps at t=1s, t=3s, t=10s, t=30s, t=100s, t=300s, between the steady and pulsatile flow simulations.

6.12. PIV Experiment Comparison

6.12.1. PIV Specifications and Results

The collaboration PIV experiment was performed using a flow phantom whose fluid area is similar in shape to the aneurysmal geometry used for the ANSYS® Fluent simulation. It however is upscaled in size for ease of use, and its dimensions differ.

Only steady flow was utilized for this experiment, since pulsatile flow was deemed too complicated to implement given the setup and distance of the pressure pump from the inlet of the flow phantom. Pressure is not accounted for in the experiment either, since there was no feasible method of modifying the pressure given the experiment's setup and timeline.

The PIV experiment yields results in the form of velocity vectors on an x-y grid, where the average magnitude and direction of fluid velocity is located at each vertex on the grid shown in Figure 21. Inlet velocity into the PIV flow phantom was measured to be 0.027 m/s, and the overall physical configuration of the collaboration PIV experiment is shown in Figure 22.

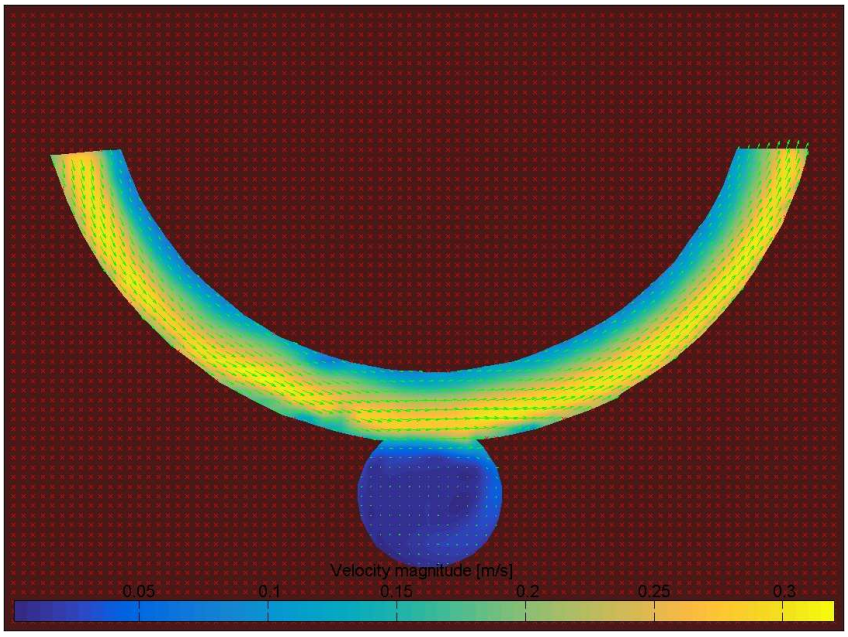

Figure 21: PIV Velocity Results

Figure 22: Physical Setup of PIV Collaboration Experiment

6.12.2. ANSYS® Fluent PIV Comparison Simulation

6.12.2.1. Geometry

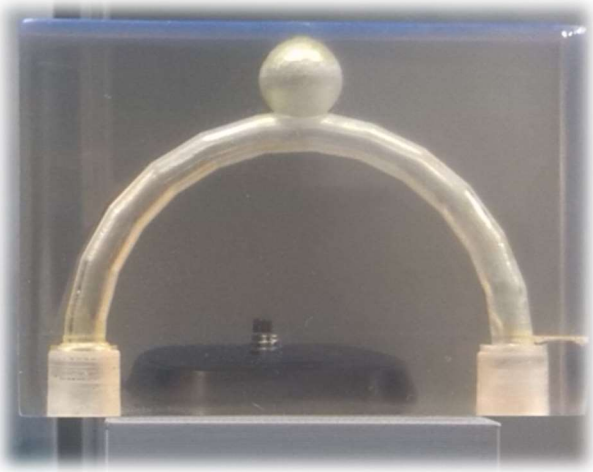

Figure 23: Printed 3D Flow Phantom

Because the scale of the flow phantom shown in Figure 23 does not match the aneurysmal geometry utilized in the pulsatile flow simulation, both a 2D and 3D simulation geometry had to be created with the flow phantom's dimensions for a proper comparison. It was determined that a 2D simulation was worth exploring, since the velocity contours of preliminary 2D simulations appeared to closely resemble the PIV velocity results. The flow phantom geometry dimensions utilized for the 3D and 2D simulations are illustrated below in Figure 24.

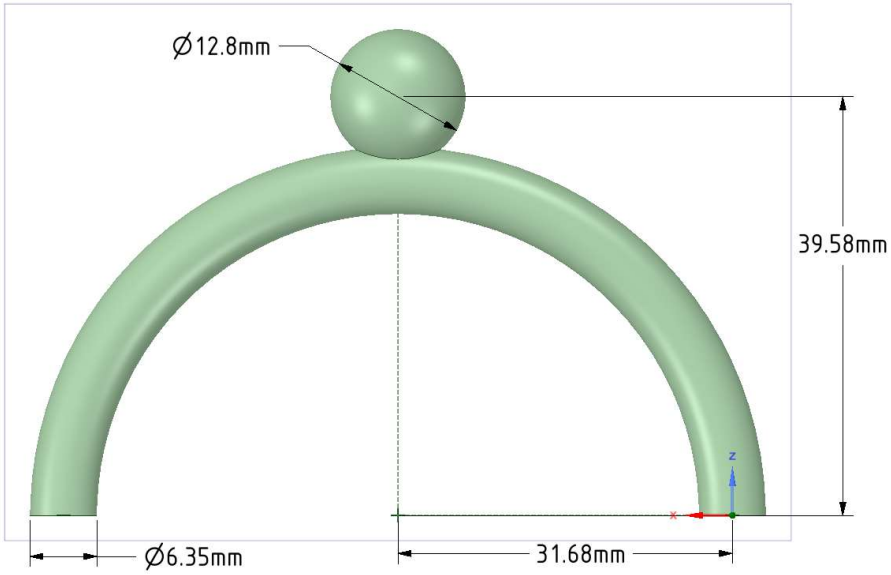

Figure 24: PIV Simulation Geometry

6.12.2.2. Mesh

Like the original mesh, the 3D PIV mesh (illustrated in Figure 25) was made as fine as possible, consisting of 402236 elements and 109380 nodes. Global default element size was set to 6.7e-4 m. The mesh deviates from this default size at the aneurysm zone, and at the edge connecting the aneurysm zone and the artery zone, where element size is set as 3.35e-4 m. Inflation of five layers is employed at the walls of the aneurysm zone and artery zone, as well as the connection between the two zones. The skewness and orthogonal quality statistics of the mesh are displayed in Table 6.

The 2D PIV mesh, seen in Figure 26, was designed with similar considerations, consisting of 2703 elements and 2887 nodes. Global default element size was set to 6.7e-4 m, and the element size at the aneurysm zone is set as 3.35e-4 m. The skewness and orthogonal quality statistics of the mesh are displayed in Table 7.

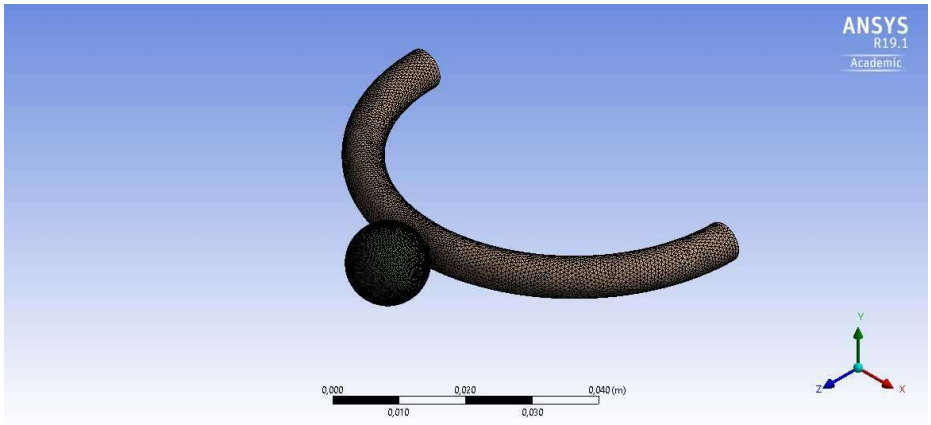

Figure 25: 3D PIV Simulation Mesh

Mesh Metric	Min	Max	Average	Standard Deviation
Orthogonal Quality	0.17509	0.99598	0.80529	0.1213
Skewness	8.589e-6	0.82491	0.19321	0.12277

Table 4: 3D PIV Mesh Orthogonal Quality and Skewness

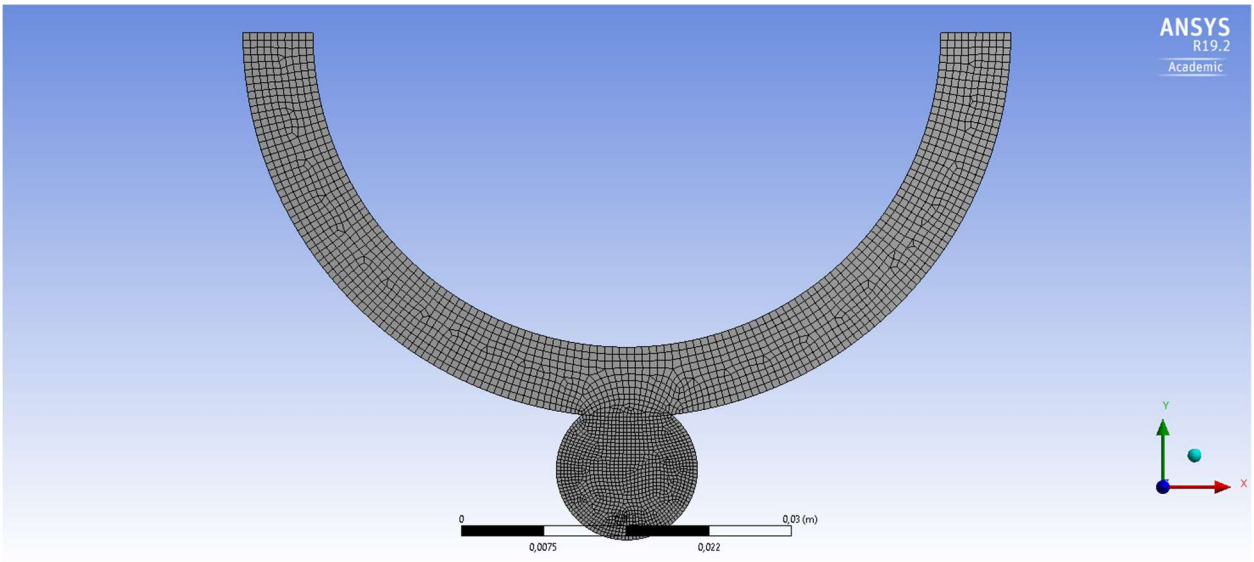

Figure 26: 2D PIV Simulation Mesh

Mesh Metric	Min	Max	Average	Standard Deviation
Orthogonal Quality	0.70143	1	0.98657	2.5623e-2
Skewness	1.9218e-3	0.59226	9.3251e-2	9,4947e-2

Table 5: 2D PIV Mesh Orthogonal Quality and Skewness

6.12.2.3. Solver Settings

The solver settings for the PIV comparison simulation are identical to those used for the steady flow simulation, save that the thrombin concentration function is not employed. A timestep of 0.01s is used, and the simulation is calculated over a total of 6000 timesteps to ensure full development of flow. The convergence criteria for these simulations are that continuity, x-velocity, y-velocity, & z-velocity residuals all fall below 0.001 each timestep.

6.12.2.4. Materials

The material properties of the mixture used in the PIV experiment were used in place of the blood material properties. They are as follows.

Fluid	Ammonium Thiocyanate 66% + Deionized Water 34% at 20-25C
Density	1131 kg/m^3
Viscosity	2.5e-3 $Pa \cdot s$

Table 6: PIV Experiment Fluid Properties

6.12.2.5. Cell-Zone Conditions

The cell-zone conditions for the PIV comparison simulations are identical to those used for the pulsatile and steady flow clotting simulations, save that a porous zone is never defined in the aneurysm zone, and it is therefore identical in setup to the artery zone.

6.12.2.6. Boundary Conditions

The boundary conditions for the PIV comparison simulations are like those used in the steady flow clotting simulation. The outlet gauge pressure is set as 11100 pascals for both the 2D and 3D PIV simulations, and the inlet velocity is set as 0.027 m/s for the 2D PIV simulation. Because of the way the velocity profile distributes in the 3D PIV comparison simulation, the velocity in the center of the artery zone is not representative of the PIV experiment results when the measured PIV inlet velocity of 0.027 m/s is applied upon the inlet area. Specifically, the velocity at the no-slip walls tends towards 0, which drives the velocity at the centerline of the artery zone up to maintain an average velocity of 0.027 m/s. To account for this

difference, the velocity magnitude of the 5 points at location 1 shown in Figure 27 was averaged for both the PIV experiment and an initial run of the 3D PIV simulation using the 0.027 m/s velocity inlet, and the percentage deviation of the experimental data from the simulation. The velocity inlet was then reduced by this percentage to 0.017 m/s, which produces a velocity profile more representative of the PIV results. The UDS scalar boundary aneurysm wall function is not applied at the aneurysm wall.

6.12.3. PIV Simulation Post-Processing

The X-Z postprocessing plane shown in Figure 19 is used to generate a velocity contour of both the 2D and 3D PIV simulation solution for comparison to the PIV experiment velocity results within the aneurysmal sac. The average of velocity in the x and y directions of the combined respective coordinates located at each numbered location shown in Figure 27 are compared to the corresponding averages from the PIV experimental results at the same coordinates Using these averages, the standard deviation of the 2D and 3D PIV simulation results from the PIV experimental results are calculated.

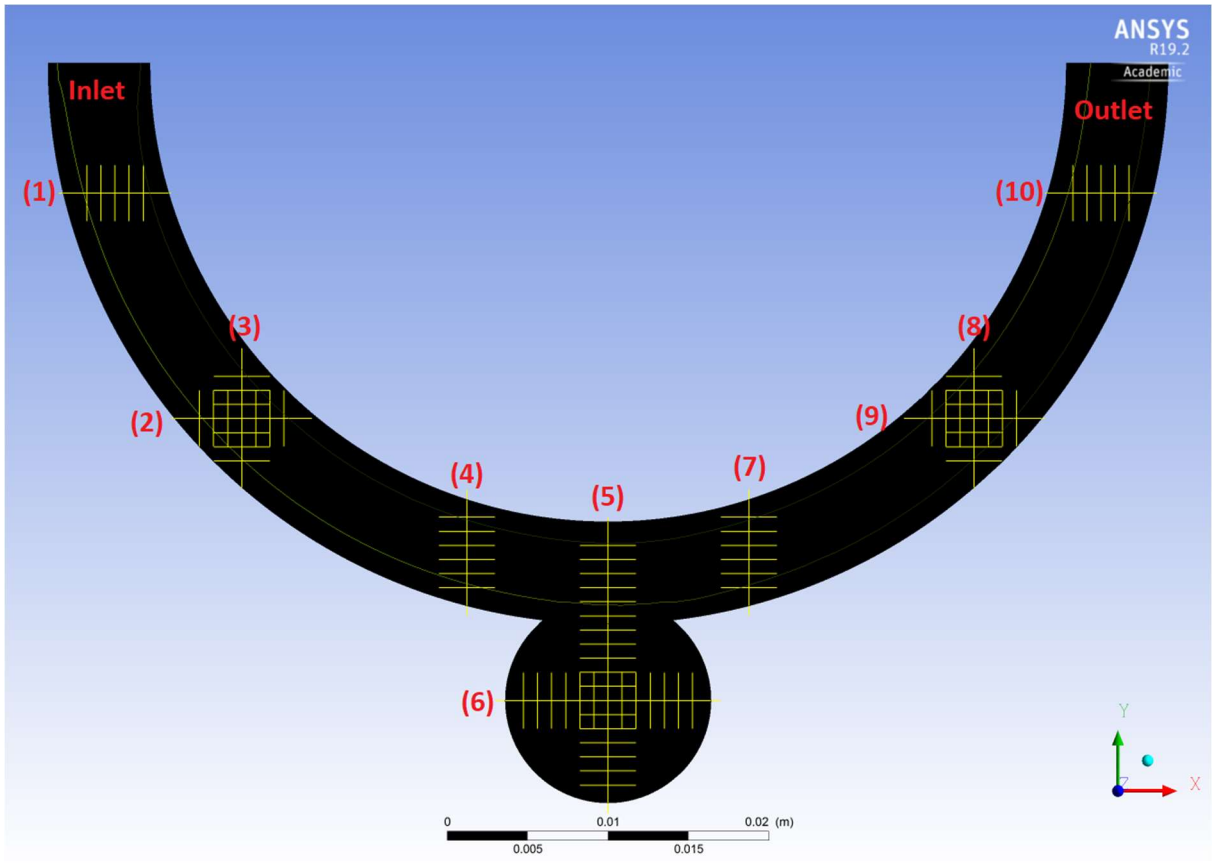

Figure 27: Numbered Locations for 2D and 3D PIV Simulation Coordinate Averages

The velocities at location 5 & 6 of Figure 27 are also compared to the output of probe's A &C shown in Figure 28 to determine differences in the velocity profile between the PIV simulations and PIV experiment results. Because these probes occupy the same relative locations as probes A & C applied in the pulsatile and steady flow models shown in Figure 17.

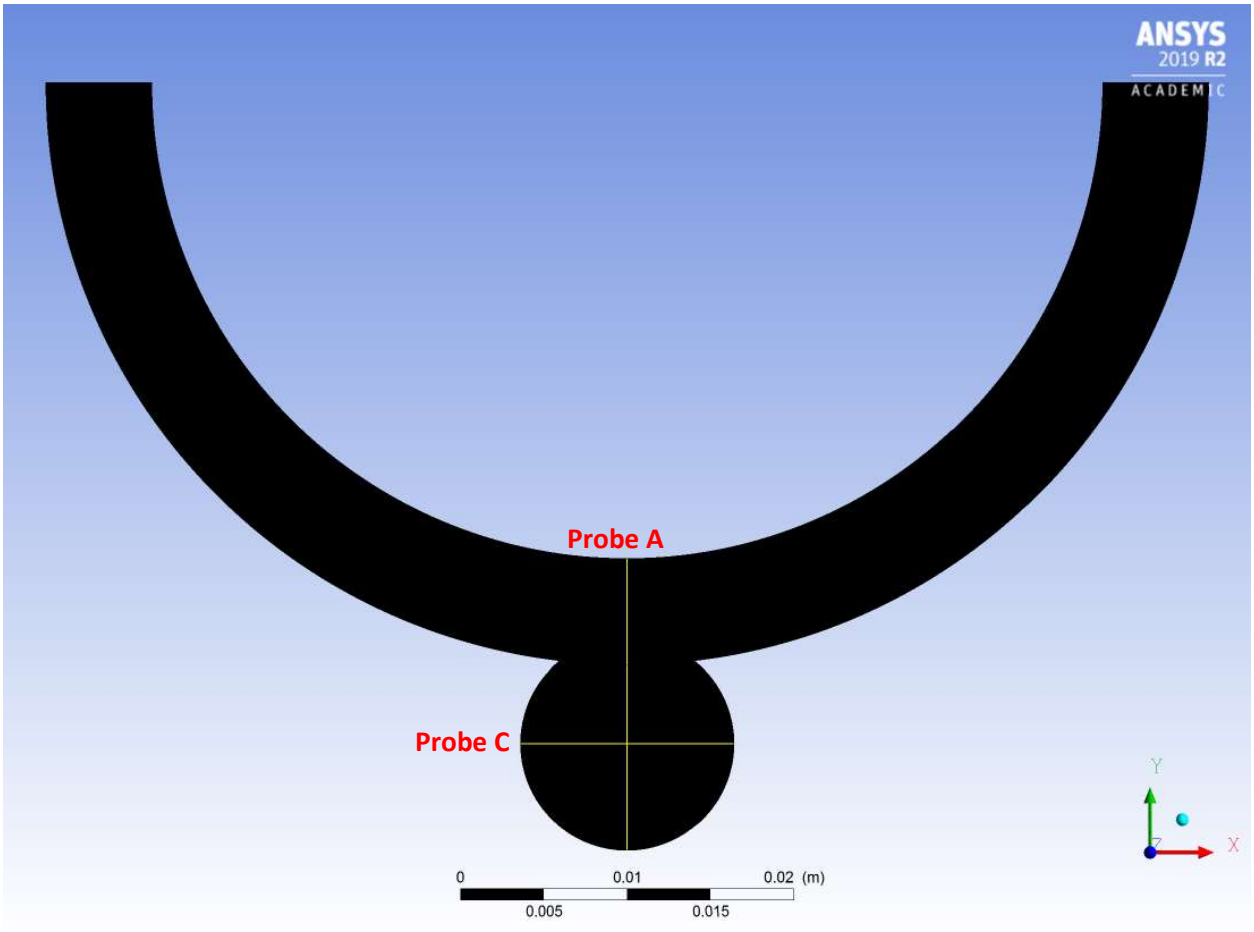

Figure 28: PIV Simulation Probe's A & C

7. Results

7.1. Steady Flow

The results of the steady flow model using the geometry shown in Figure 6 are recorded in this section. Specifically, velocity, pressure, and thrombin concentration scalar outcomes are observed.

7.1.1. Velocity Behavior

7.1.1.1. Velocity Contour Analysis

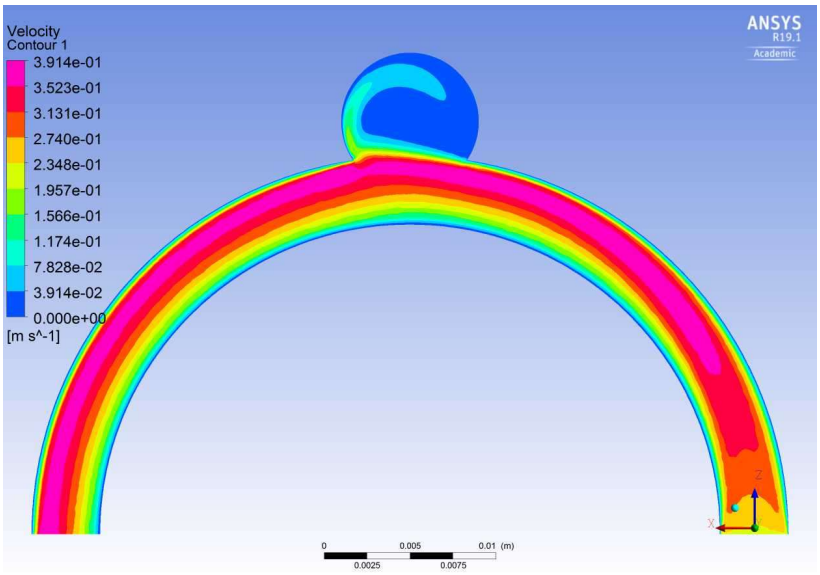

Figure 29: Steady Flow Velocity Contour at 30s

As illustrated in Fig 29, the highest velocity particles tend towards the outer edge of the artery zone, and a portion of these high velocity particles split off into the aneurysm zone and circulate along the aneurysm wall on the side closest to the outlet. After flow fully develops at the inlet, the highest velocity particles are consistently distributed along the outer edge of the arterial zone, such that this behavior continues to the outlet. The lowest velocity particles circulate within the center of the aneurysm.

7.1.1.2. Velocity Probe Analysis

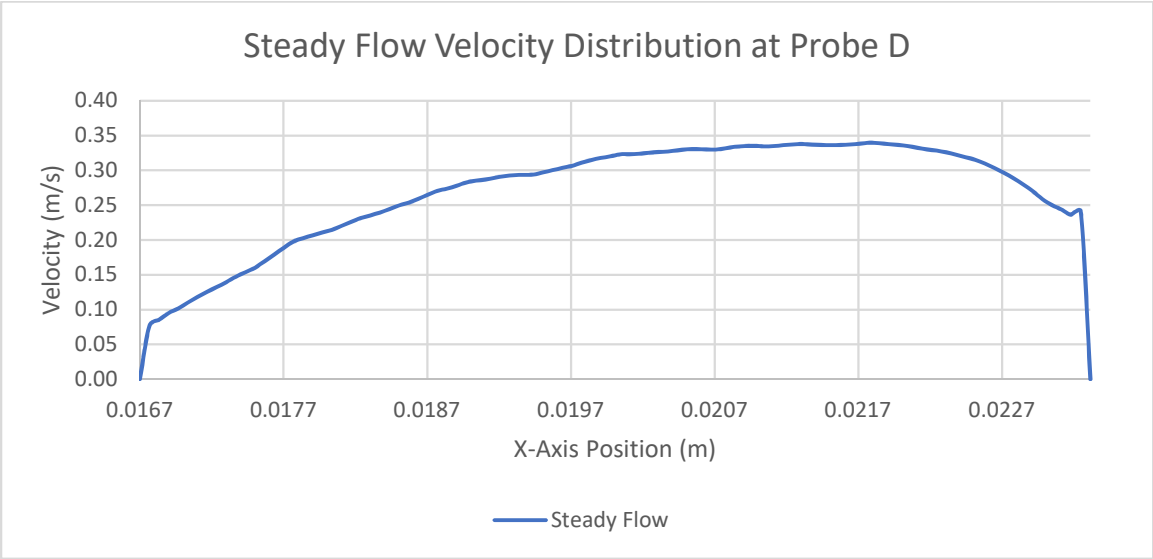

Figure 30: Probe D Steady Flow Velocity Distribution at 30s

As shown in Figure 30, velocity at Probe D increases with distance from the inlet, and drops just before the edge of the aneurysm neck closest to the outlet. The velocity distribution across Probe C shown in Figure 31 exhibits similar behaviour, but is significantly more pronounced at the side of the aneurysm wall most proximal to the outlet.

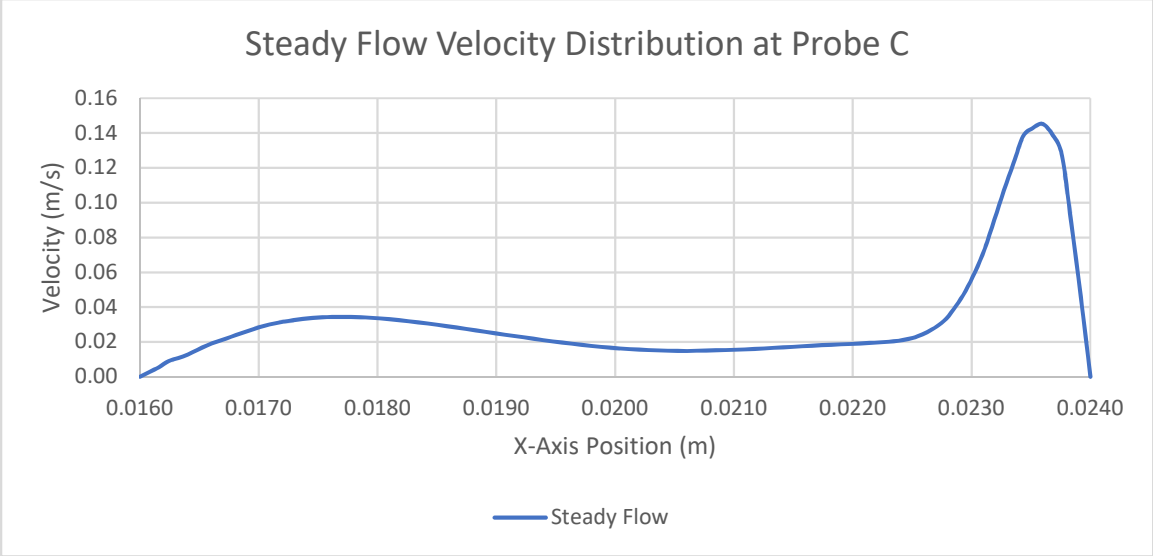

Figure 31: Probe C Steady Flow Velocity Distribution at 30s

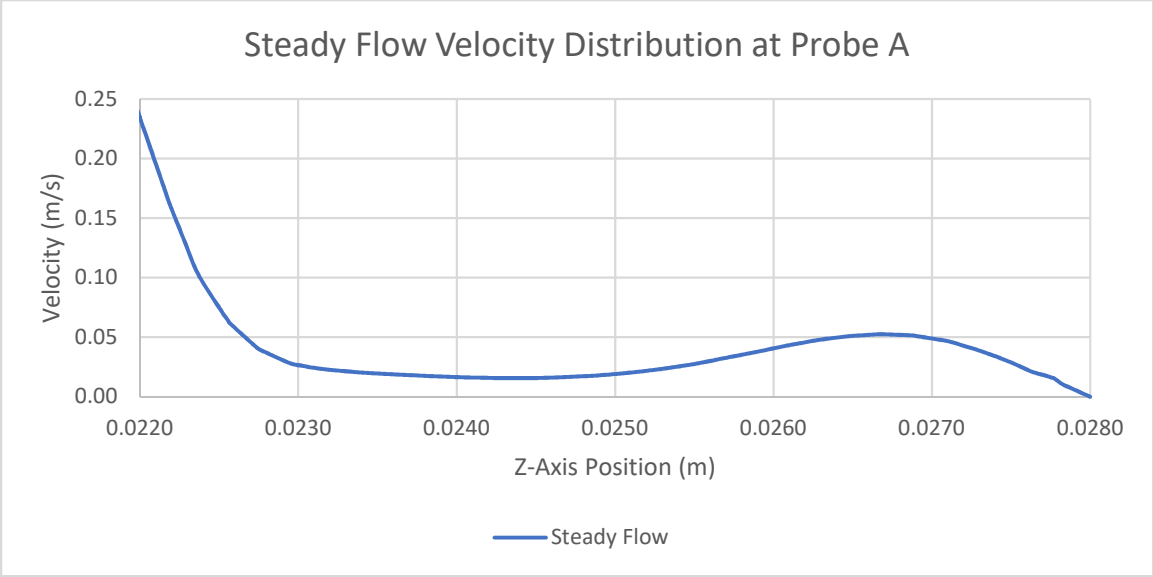

Figure 32: Probe A Steady Flow Velocity Distribution at 30s

Figure 32 shows that velocity through Probe A decreases sharply from the aneurysm neck, but begins to increase again slightly as it approaches the aneurysm wall. Figure 33 shows that velocity distribution across Probe B is significantly lower in magnitude than the other probes, suggesting that velocity at the center of the aneurysm is universally low velocity across the y-axis.

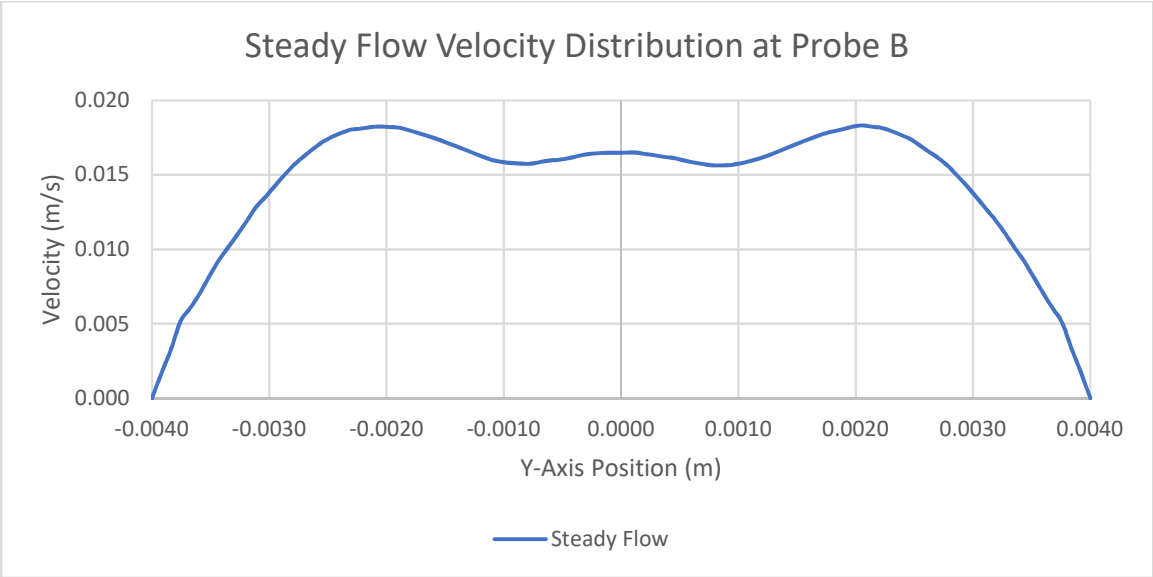

Figure 33: Probe B Steady Flow Velocity Distribution at 30s

7.1.2. Pressure Behavior

7.1.2.1. Pressure Contour Analysis

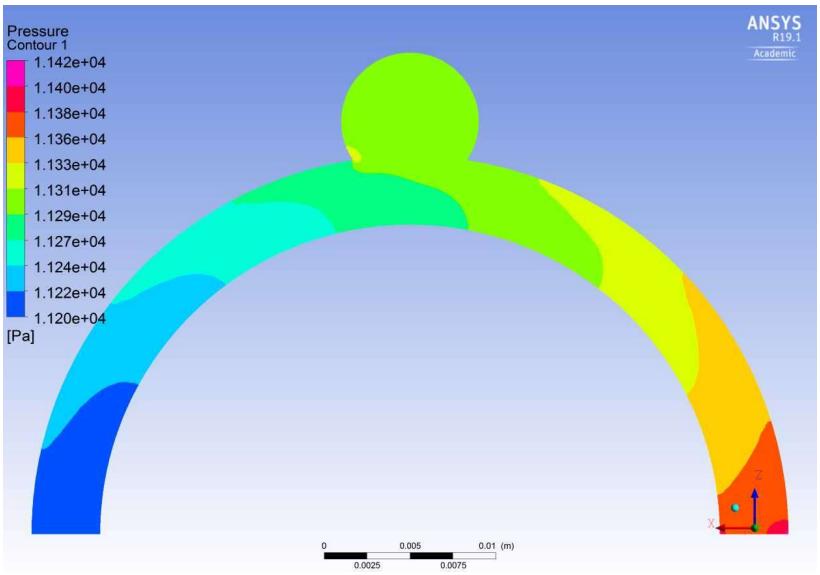

Figure 34: Steady Flow Pressure Contour at 30s

As shown in Figure 34, pressure consistently grades from high-to-low from inlet-to-outlet with an overall pressure difference of 220 Pascals. There is a slight pressure increase around the edge of the aneurysm neck closest to the outlet.

7.1.3. Thrombin Concentration Scalar Behavior

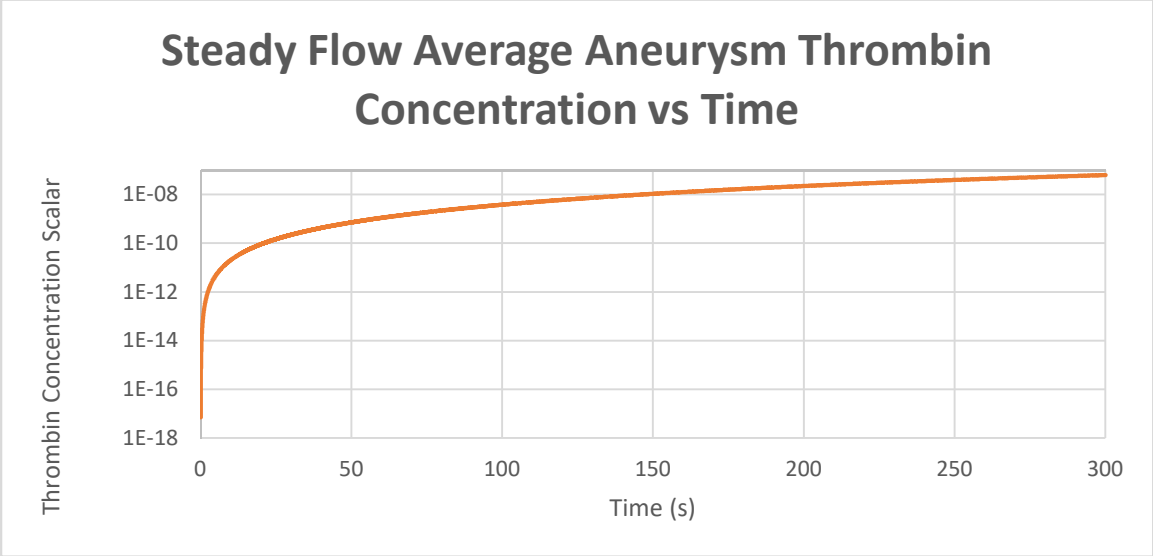

Figure 35: Steady Flow Average Aneurysm Thrombin Concentration Scalar

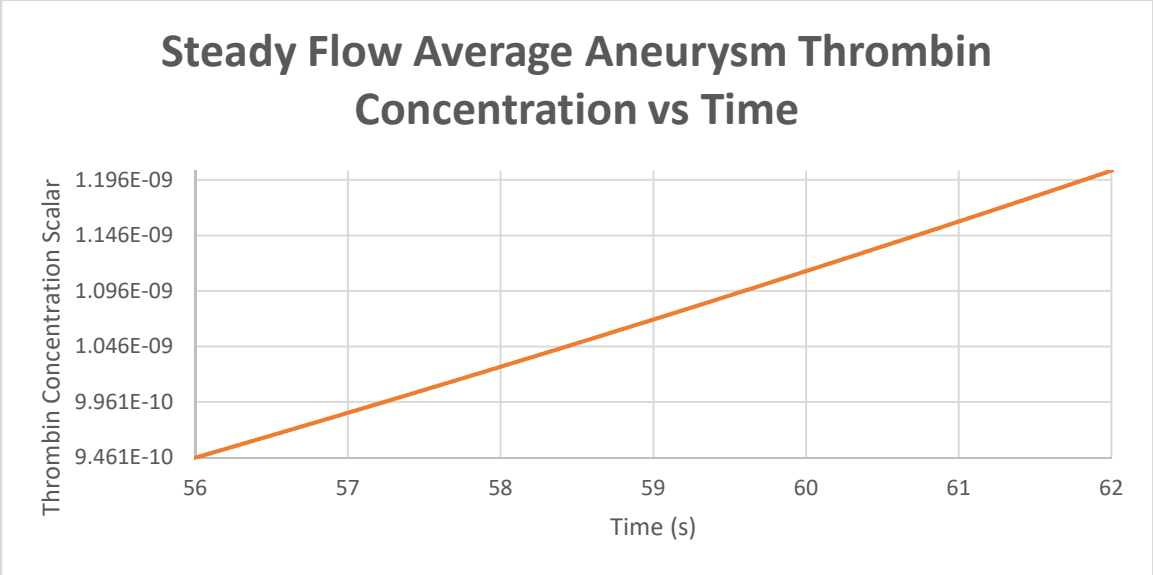

Figure 36: Steady Flow Average Aneurysm Thrombin Concentration Scalar

Figure 35 illustrates the overall output of thrombin concentration over the course of the steady flow simulation. According to Figure 36, the thrombin concentration increases roughly linearly with time when looking at small sections of the thrombin concentration curve.

7.1.3.1. Thrombin Concentration Scalar Contour Analysis

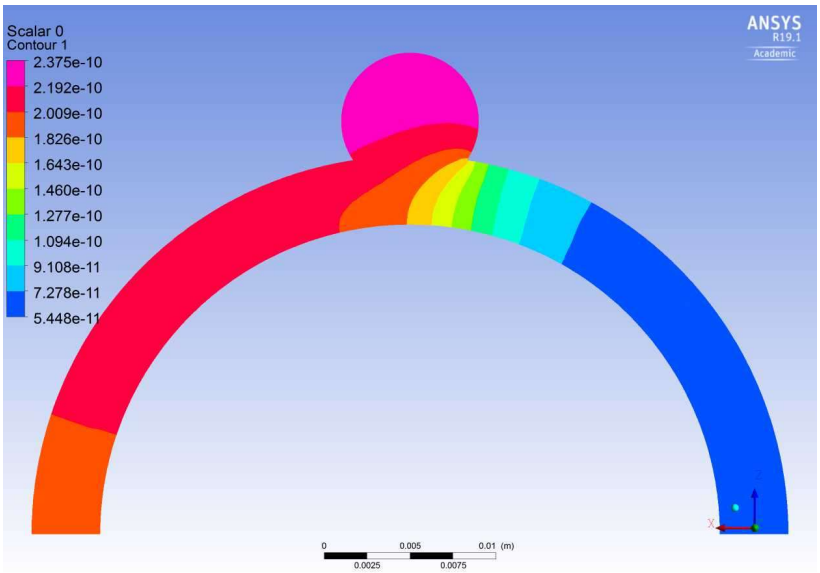

Figure 37: Steady Flow Thrombin Concentration Contour at 30s

Illustrated in Figure 37, at any given time significantly lower scalar values of thrombin concentration are observed in flow between the inlet to just before the neck of the aneurysm. Areas of highest thrombin concentration scalar values are in the top half of the aneurysm.

7.1.3.2. Aneurysm Thrombin Concentration Scalar Probe Analysis

As shown in figures 38 & 40, thrombin concentration has a positive relationship with changes in position in the positive x and z directions within the aneurysm zone. Figure 39 shows that thrombin concentration that borders the artery-zone is higher close to the aneurysm walls, with thrombin concentration being higher at the aneurysm wall farthest from the inlet.

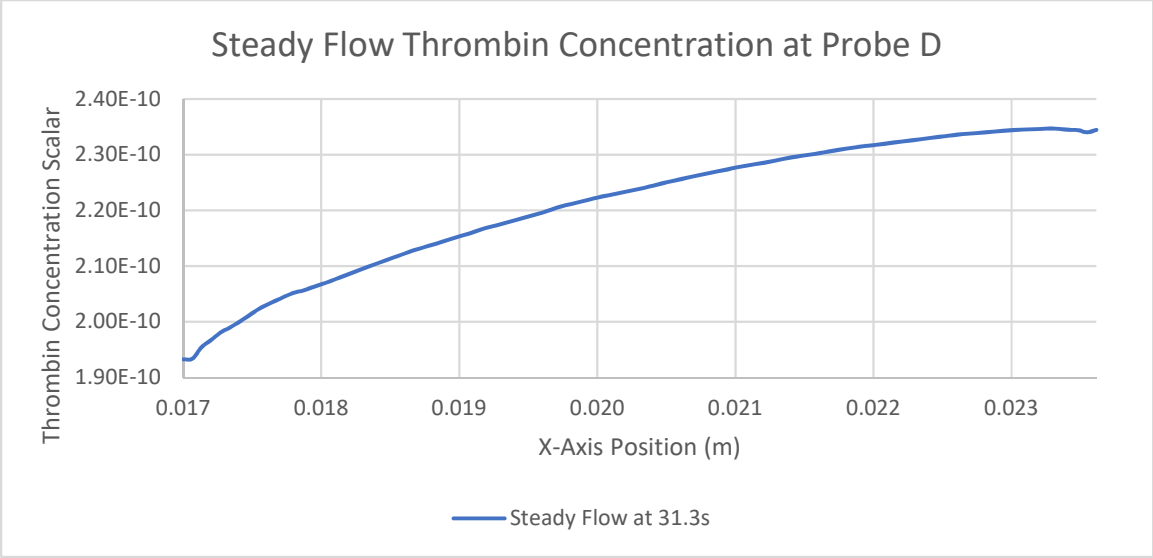

Figure 38: Steady Flow Thrombin Concentration Scalar Distribution at Probe D

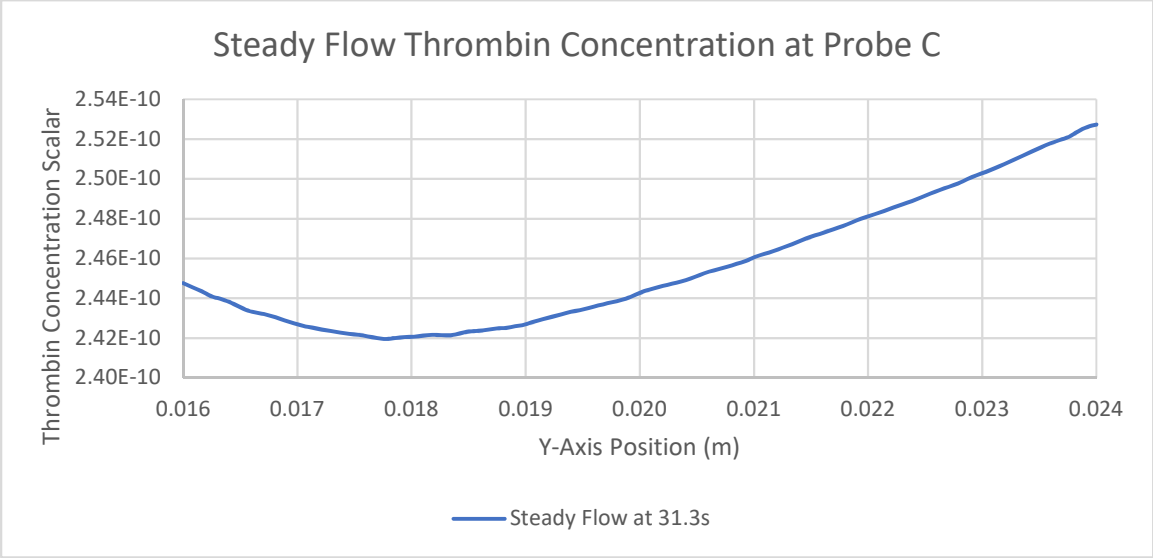

Figure 39: Steady Flow Thrombin Concentration Scalar Distribution at Probe C

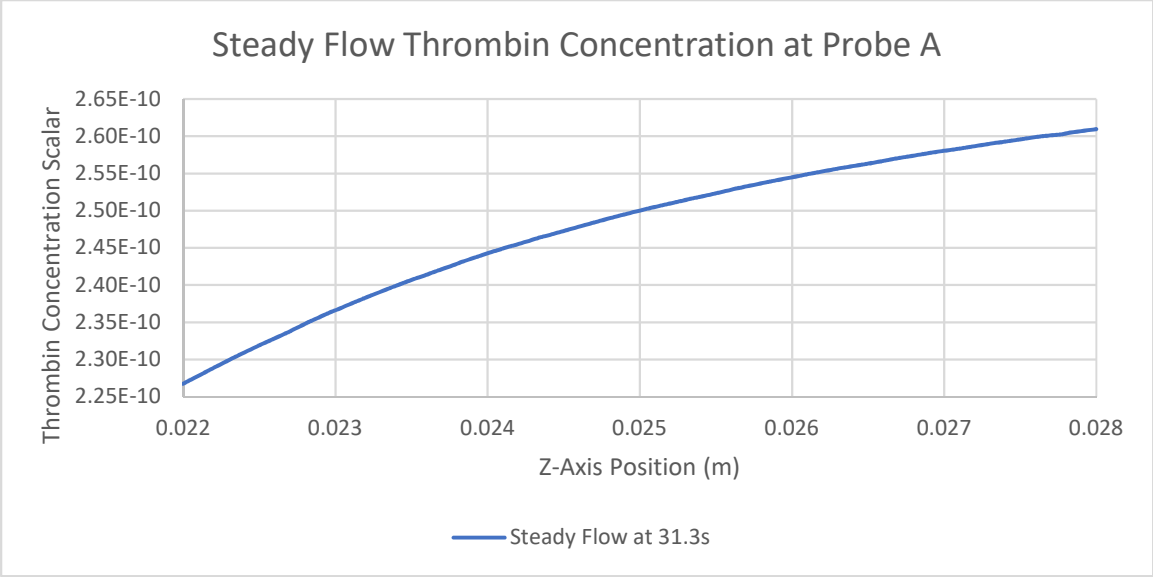

Figure 40: Steady Flow Thrombin Concentration Scalar Distribution at Probe A

According to Figure 40, thrombin concentration is similarly high near the aneurysm walls along the Probe B, and decreases towards the center of the aneurysm.

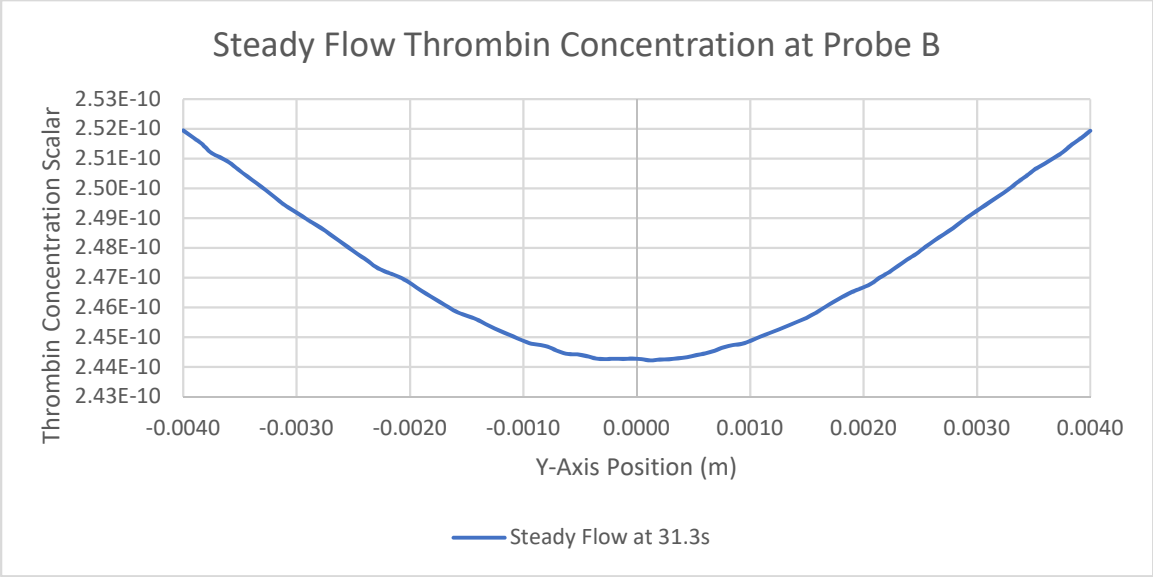

Figure 41: Steady Flow Thrombin Concentration Scalar Distribution at Probe B

7.1.3.3. Clotting Process

Thrombin concentration scalars first present condition for clotting (reaching a value of 1e-9) in the top of the aneurysm along the aneurysm wall around 56.3s, shown in Figure 42. As shown in Figure 43, the thrombin concentration increases linearly, and clotting conditions exist within the entire aneurysm zone by 61.4s

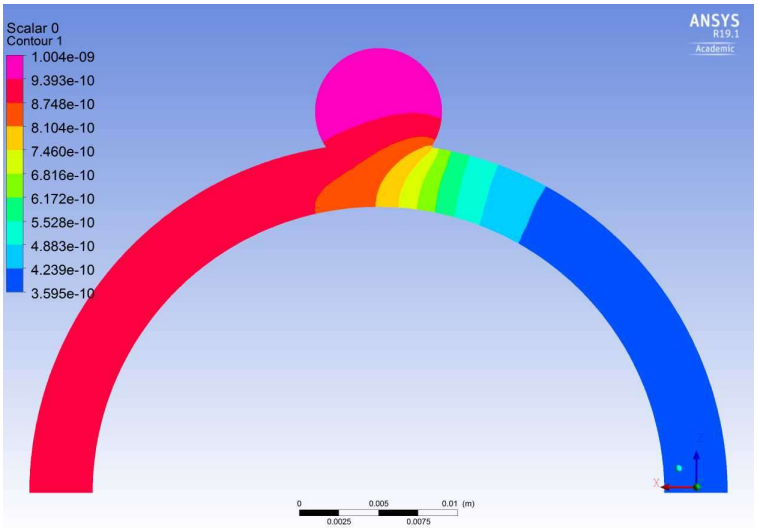

Figure 42: Steady Flow Thrombin Concentration Scalar Contour at 56.3s

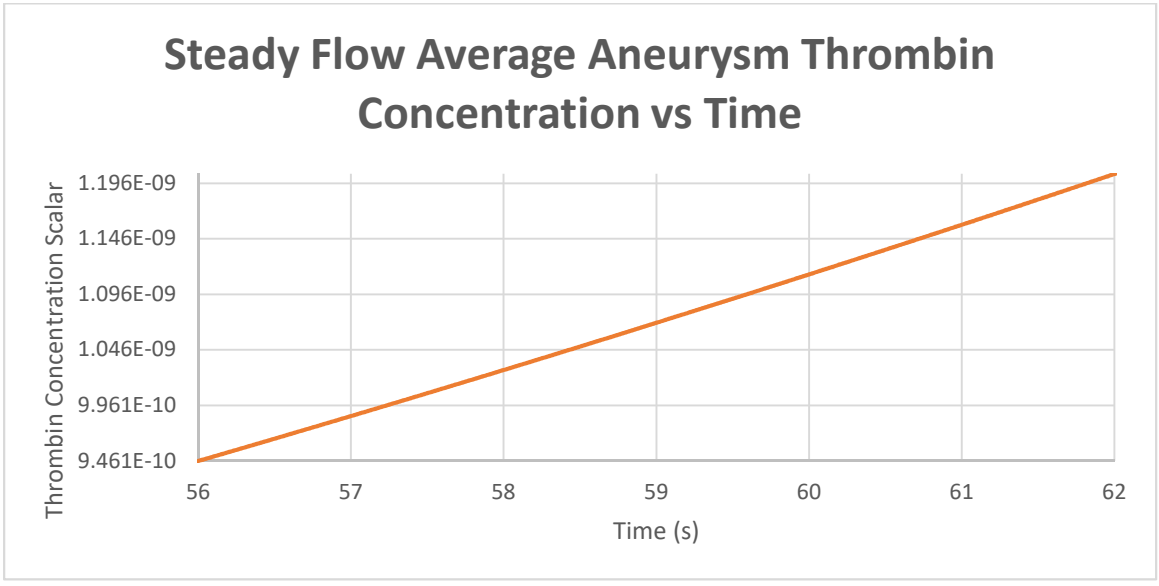

Figure 43: Steady Flow Average Aneurysm Thrombin Concentration Scalar at Clotting Start

7.2. Pulsatile Flow

This section details the velocity, pressure, and thrombin concentration behavior for the pulsatile flow model. Behavior surrounding conditions relevant to the beginning of the clotting process is documented.

7.2.1. Velocity Behavior

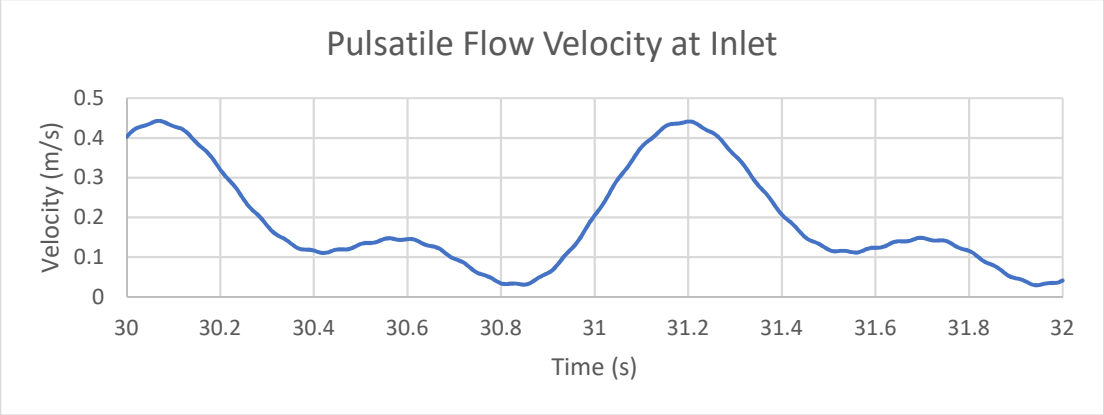

Figure 44: Pulsatile Flow Velocity vs Time at Inlet

Flow from the inlet begins with uniform velocity, that develops further down the geometry. There are four recurring time-based behaviors of note, visible on Figure 44, which captures the time at which thrombin concentration was high enough to induce significant clotting within the aneurysm-zone. These behaviors directly relate to the velocity Fourier Transform velocity-inlet function, and represent the low, upper, low-middle, and upper-middle velocity peaks visible in Figure 4.

7.2.1.1. Velocity Contour Analysis

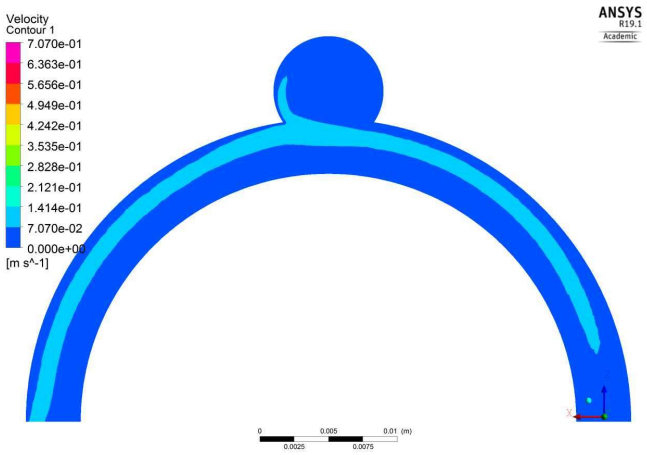

Figure 45: Low-Peak Pulsatile Flow Velocity Contour at 30.8 Seconds (Global Scale)

At the low velocity peak show in Figure 45, the relative high-velocity particles tend towards the outer-edge of the artery zone and split at the edge of the neck of the aneurysm zone closest to the outlet, causing some of the high-velocity particles to circulate into the aneurysm zone. By contrast, relatively low-velocity particles tend towards the inner edge of the artery zone, and circulate within the center of the aneurysm zone.

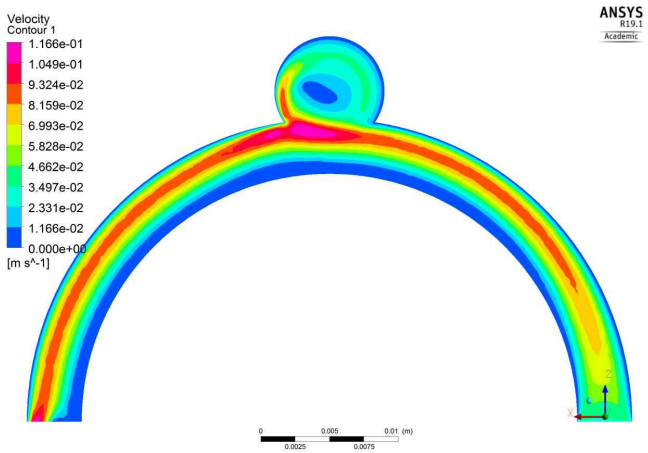

Figure 46: Low-Peak Pulsatile Flow Velocity Contour at 30.8 Seconds (Local Scale)

During the low-velocity peak further illustrated in Figure 46, the highest area of velocity develops just before the edge of the aneurysm zone closest to the outlet. This occurs again just before the outlet at the outer-edge of the artery zone, where areas of low velocity flow have expanded.

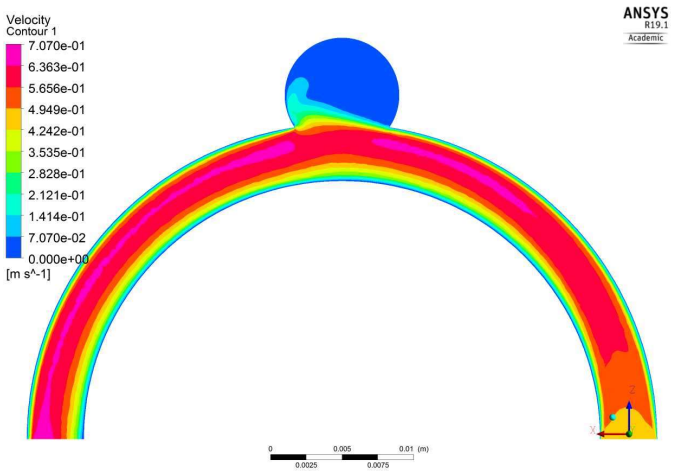

Figure 47: Upper-Peak Pulsatile Flow Velocity Contour at 31.2 Seconds (Global Scale)

During the upper velocity peak illustrated in Figure 47, high velocity particles also tend towards the outer-edge of the arterial-geometry. However, as velocity increases from the low-velocity peak, the areas of highest velocity migrate away from the edge of the aneurysm geometry and expand towards the outlet.

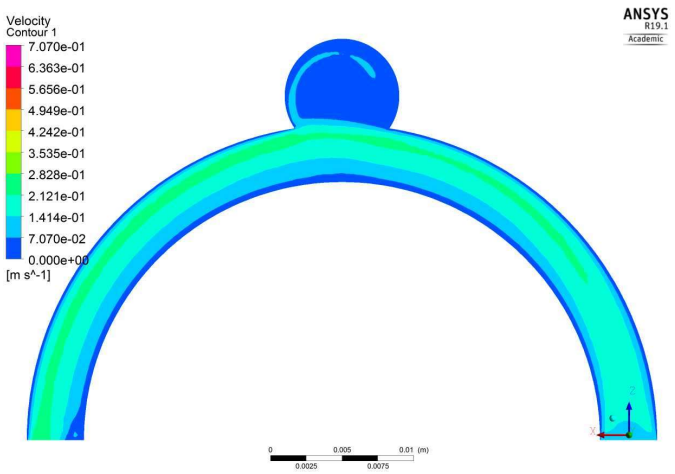

Figure 48: Lower-Middle Peak Pulsatile Flow Velocity Contour at 31.6 Seconds (Global Scale)

As overall flow velocity decreases from the upper-velocity peak, particles from the artery zone begin to circulate along the aneurysm zone wall, and they begin to distribute within the aneurysm zone, illustrated in Figure 48. Low flow velocity propagates at the inner-edge of the artery-zone near the outlet.

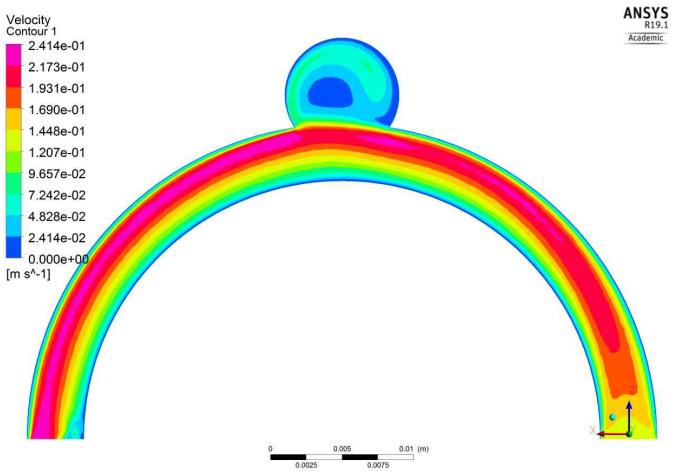

Figure 49: Lower-Middle Peak Pulsatile Flow Velocity Contour at 31.6 Seconds (Local Scale)

Circulation of particles within the aneurysm-zone is high during the lower-middle velocity peak according to Figure 49. Despite this, the lowest flow velocity still lies within the center of the aneurysm zone. Areas of high flow are distributed along the artery zone past after flow becomes fully-developed.

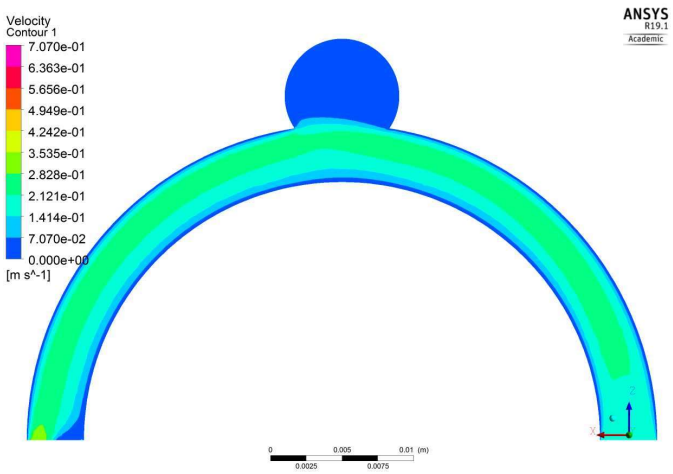

Figure 50: Upper-Middle Peak Pulsatile Flow Velocity Contour at 31.7 Seconds (Global Scale)

Velocity increases slightly from the lower-middle velocity peak to the upper-middle velocity peak. Incursion of relatively high-velocity particles from the artery-zone into the aneurysm-zone is minimal as shown in Figure 50.

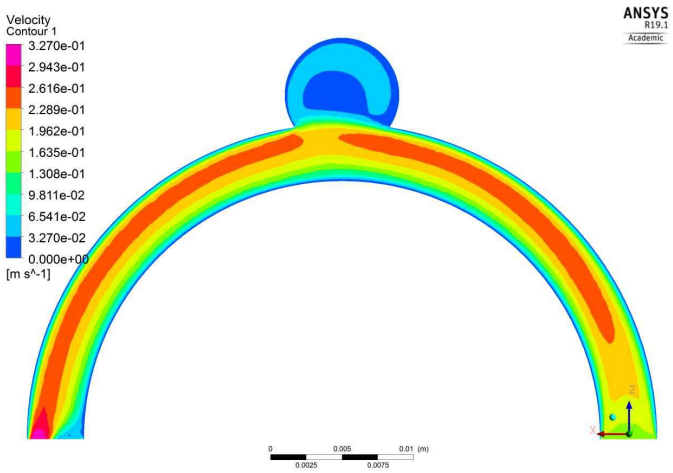

Figure 51: Upper-Middle Peak Pulsatile Flow Velocity Contour at 31.7 Seconds (Local Scale)

As shown in Figure 51, circulation within the aneurysm zone decreases, and becomes more distributed. The area of lowest flow velocity remains in the center of the aneurysm zone Flow within the artery zone becomes more evenly distributed, with the highest velocity cells present near the outlet.

7.2.1.2. Aneurysm Velocity Probe Analysis

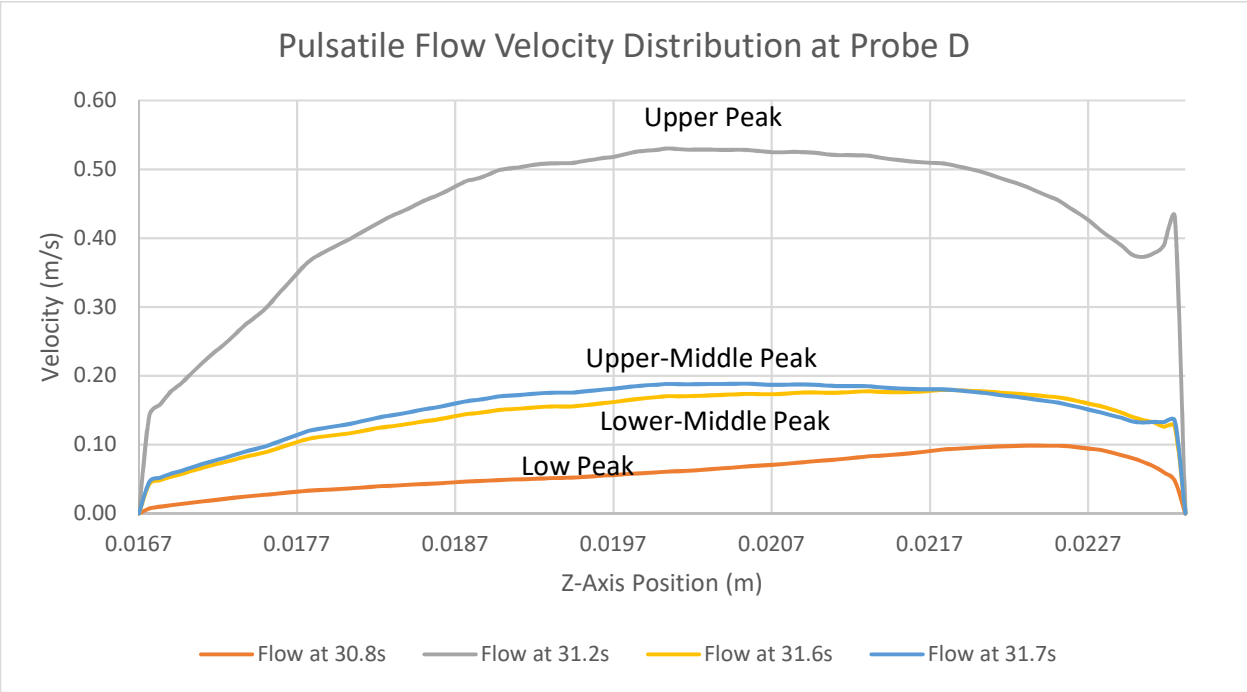

Figure 52: Pulsatile Flow Velocity Distribution at Probe D

At the neck of the aneurysm, shown in Figure 52, peaks of are roughly proportional to the velocity magnitude of the corresponding peaks. The velocity distribution behaviour changes drastically along Probe C shown in Figure 53, where velocity at the side of the aneurysm wall closest to the inlet is higher at the low velocity peak than at the lower-middle and upper-middle velocities. When examining the behaviour towards other side of the aneurysm wall in Figure 54, velocity is highest at the low velocity peak, and lowest at the upper velocity peak.

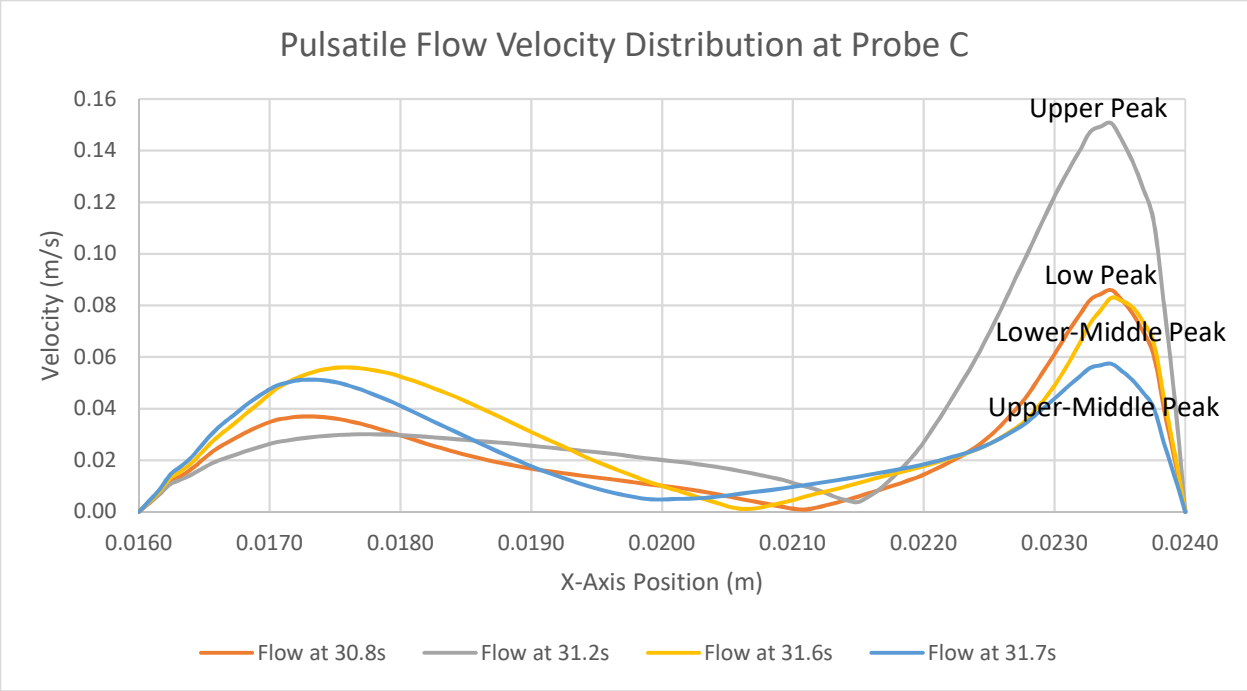

Figure 53: Pulsatile Flow Velocity Distribution at Probe C

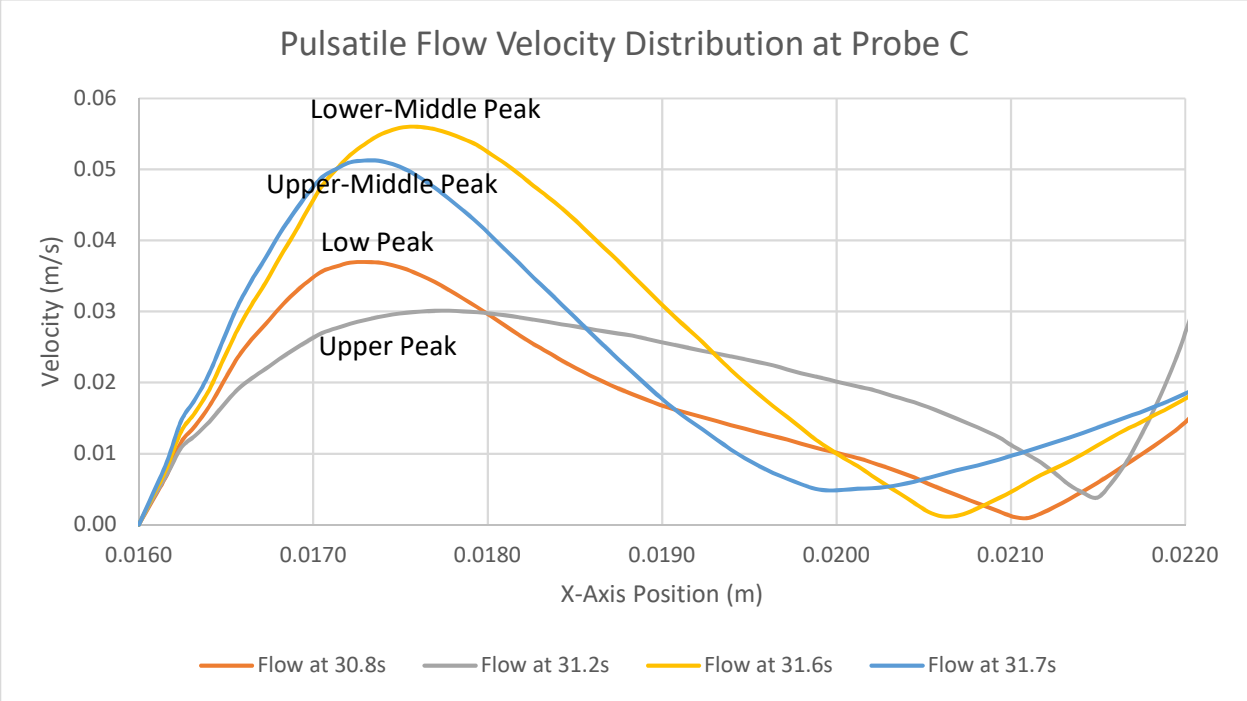

Figure 54: Pulsatile Flow Velocity Distribution at Low Velocity Side of Probe C

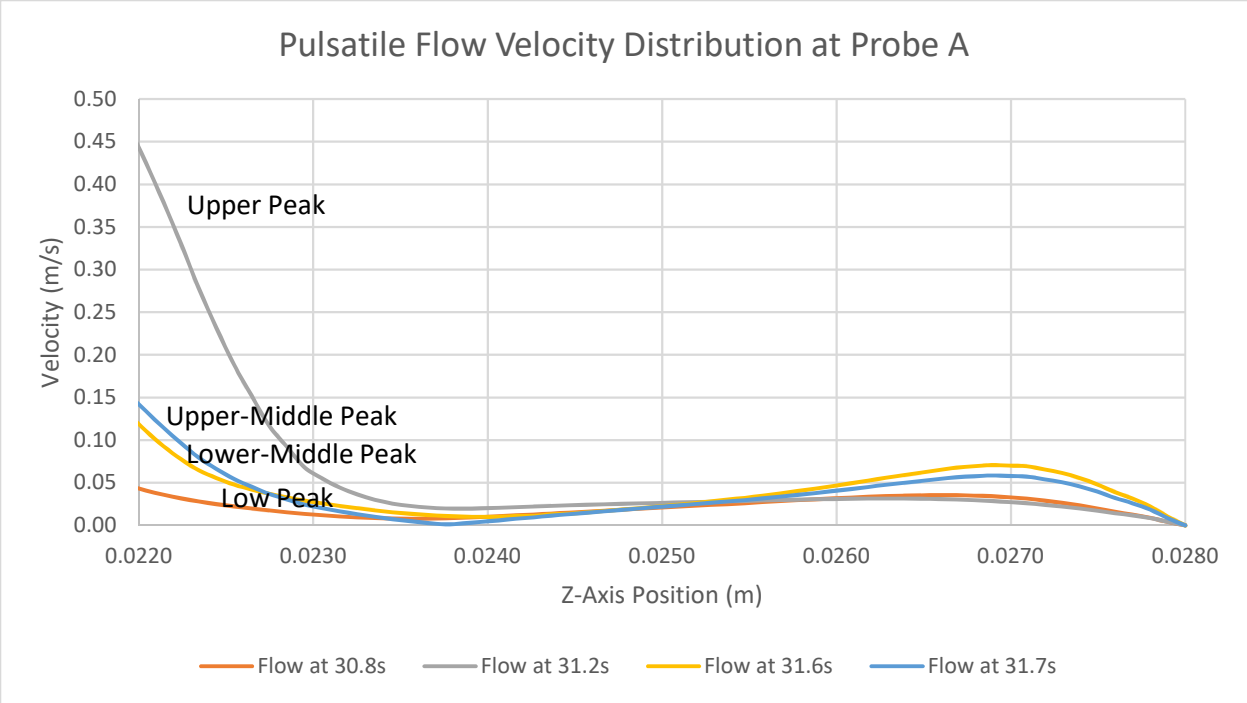

Figure 55: Pulsatile Flow Velocity Distribution at Probe A

Velocity distribution along Probe A shown in Figure 55 shows that velocity magnitudes are proportional to peaks near the connection between the aneurysm and the artery. When examining the center-axis velocity distribution towards the aneurysm wall in Figure 56, velocity along the aneurysm wall is higher at the upper and lower-middle peaks of velocity, than the lower and upper peaks of velocity, suggesting that flow in this region increases when overall flow is decreasing. Velocity distribution across the y-axis, as shown in Figure 57, is similar in this regard. Towards the aneurysm walls, velocity is highest at the lower-middle velocity peak, and lowest at the low velocity peak. Towards the center of Probe B, velocity seems to be lowest at the upper-middle peak, and highest at the upper peak. Velocity distributions at the upper and low velocity peaks across the y-axis appear roughly even, and the peaks upper-middle and lower-middle peaks are the opposite.

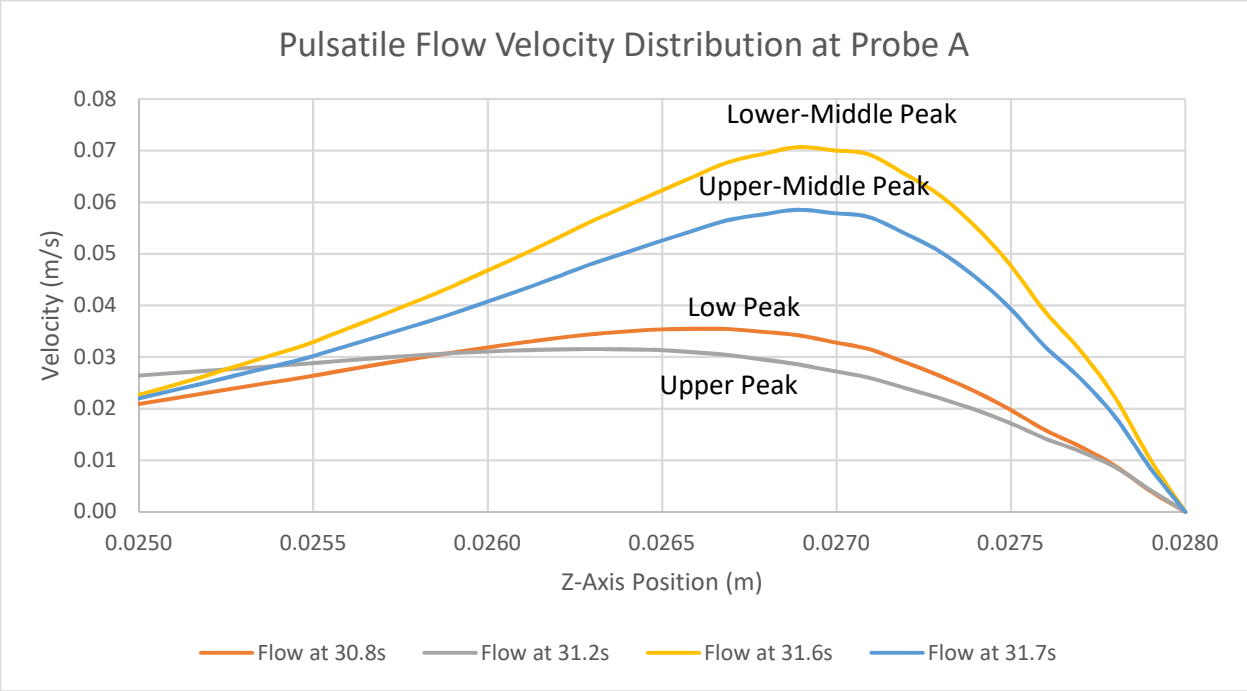

Figure 56: Pulsatile Flow Velocity Distribution at Top of Probe A

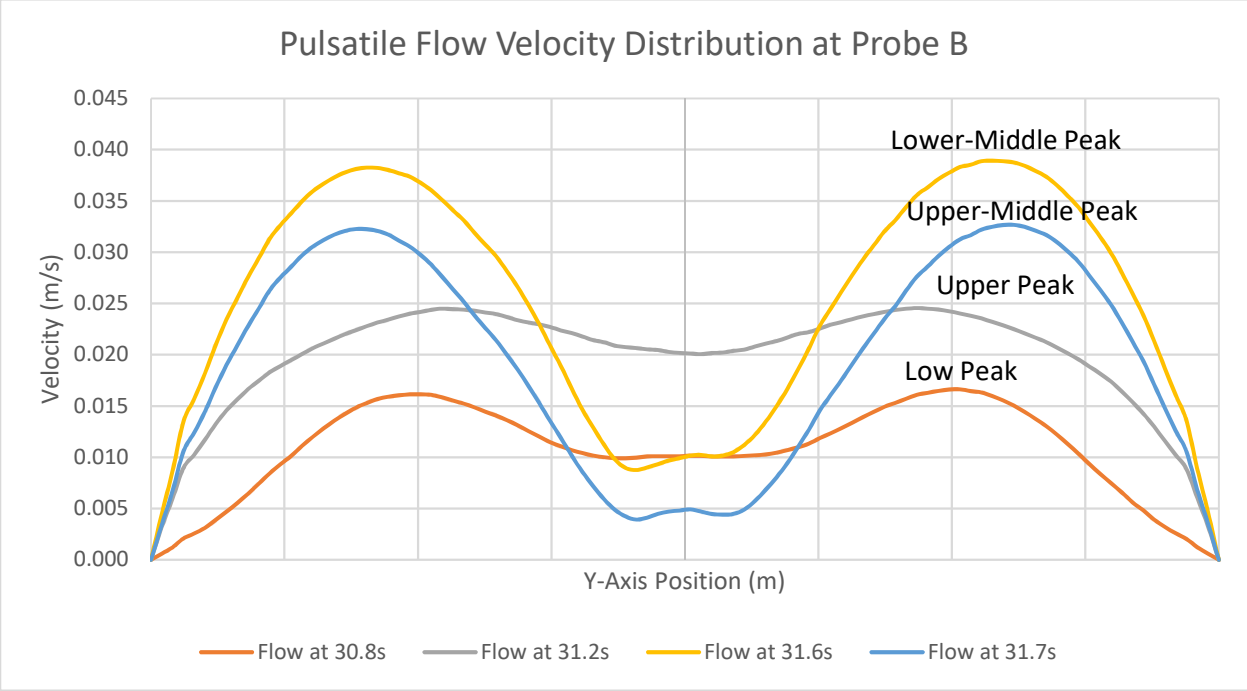

Figure 57: Pulsatile Flow Velocity Distribution at Probe B

7.2.2. Pressure Behavior

Pressure values are relatively uniform throughout the geometry at a given timestep, with slight deviations in certain locations. Pressure changes over time as dictated by the pressure Fourier Transform, shown at the inlet in Figure 58. There are three recurring time-based behaviors of note; the upper-peak pressure, the lower peak pressure, and a brief reversal in direction of the pressure gradient.

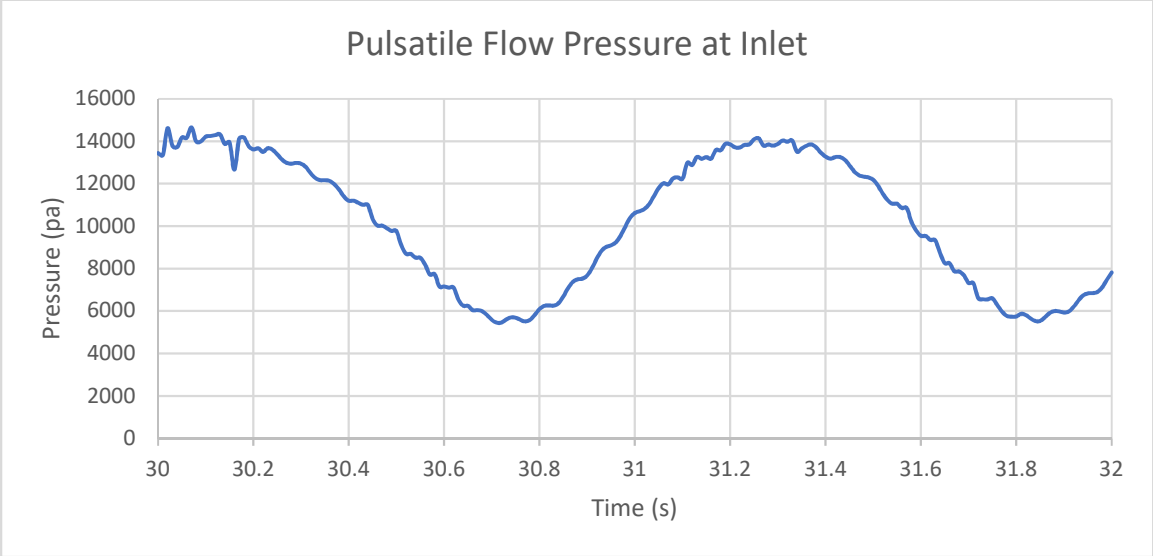

Figure 58: Pulsatile Flow Pressure vs Time at Inlet

7.2.2.1. Pressure Contour Analysis

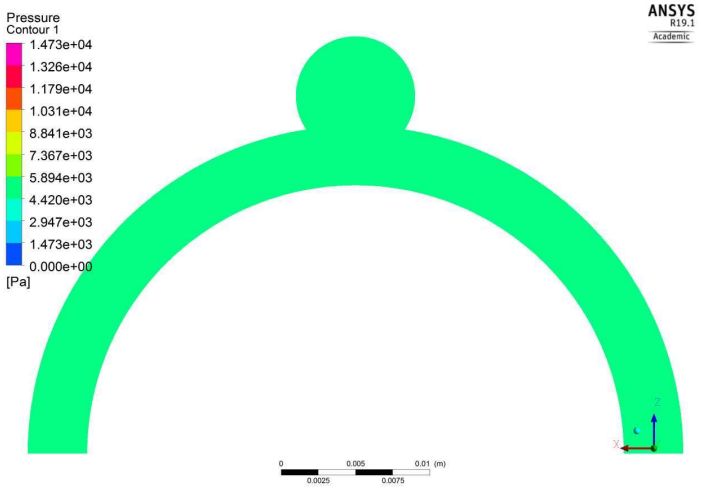

Figure 59: Lower-Peak Pulsatile Flow Pressure Contour at 30.7 Seconds (Global Scale)

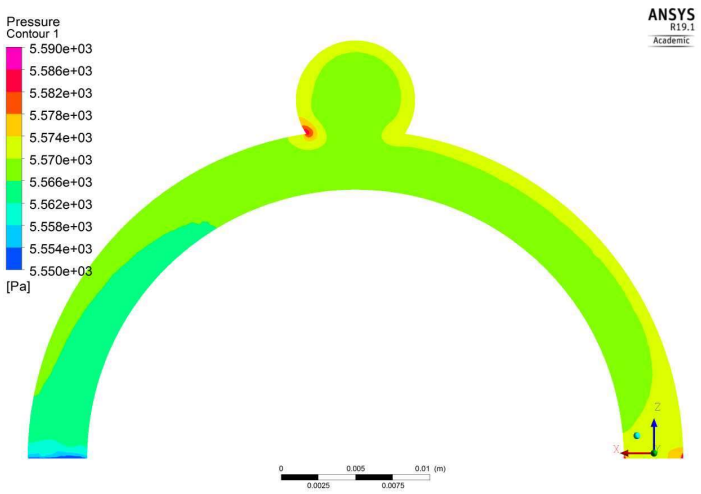

Figure 60: Lower-Peak Pulsatile Flow Pressure Contour at 30.7 Seconds (Local Scale)

Figure 59 shows pressure at the lower-peak. As shown in Figure 60, pressure grades by 40 pascals from the inlet to the outlet at the lower pressure peak. High pressure cells are located at the outer wall of the geometry up until the neck of the aneurysm zone proximal to the outlet, where the highest-pressure cells are concentrated.

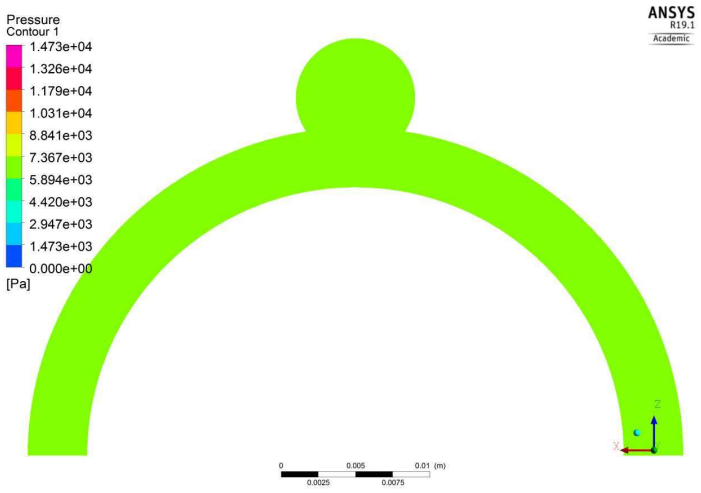

Figure 61: Low-High Pressure Gradient Pulsatile Flow Pressure Contour at 30.8 Seconds (Global Scale)

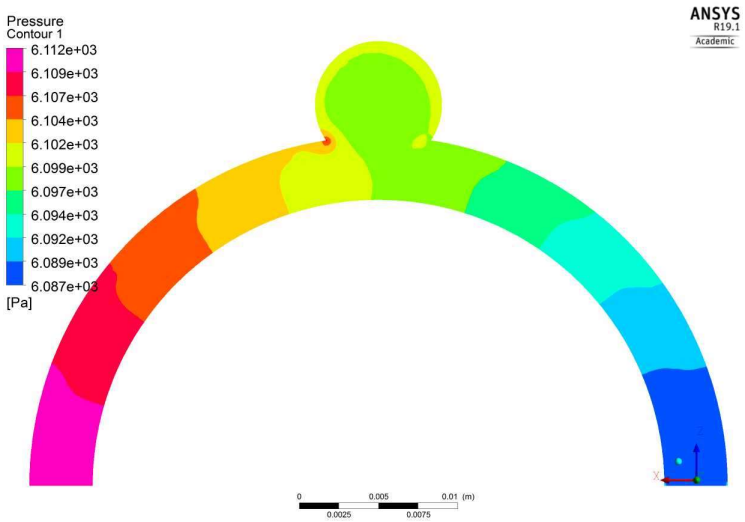

Figure 62: Low-High Gradient Pulsatile Flow Pressure Contour at 30.8 Seconds (Local Scale)

Figure 61 shows pressure Just after the lower pressure peak. Figure 62 observes local pressure behaviour at this time, and shows the pressure difference from the inlet to the outlet briefly changes from high-low to low-high for around 0.1s. The indication of this is unclear.

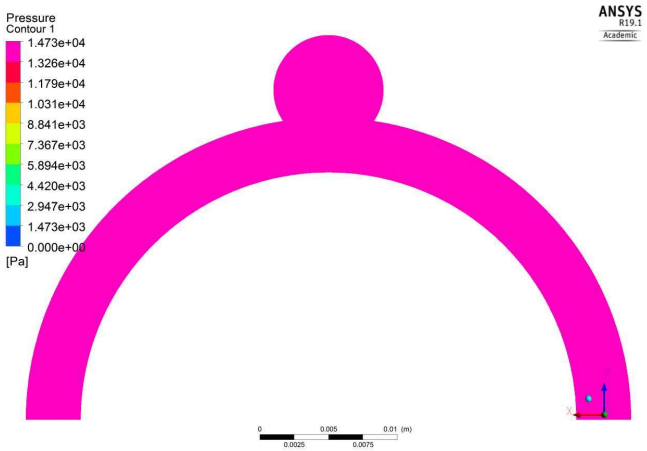

Figure 63: Upper-Peak Pulsatile Flow Pressure Contour at 31.3 Seconds (Global Scale)

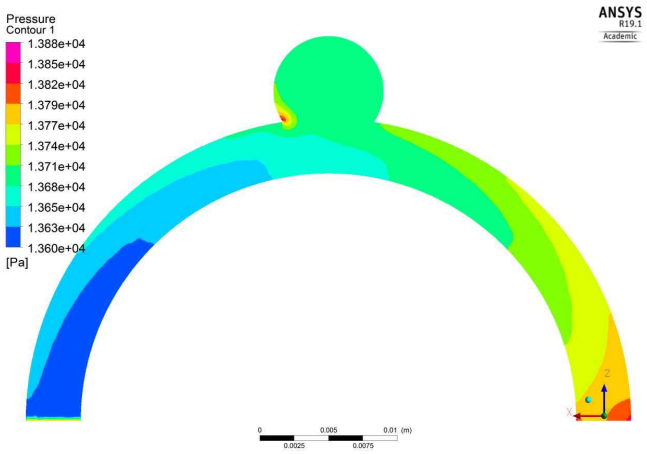

Figure 64: Upper-Peak Pulsatile Flow Pressure Contour at 31.3 Seconds (Local Scale)

Figure 63 shows pressure at the upper peak. Figure 64 illustrates that the pressure difference between the inlet and outlet grows to its largest point at this time. Relatively high pressure is continuous at the edge of neck of the aneurysmal geometry most proximal to the outlet.

7.2.3. Thrombin Concentration Scalar Behavior

Figure 65 shows that the thrombin concentration scalar tends upwards throughout the simulation. Figure 66 examines this trend at a smaller time interval, and indicates that the scalar exhibits quasi-periodic behavior.

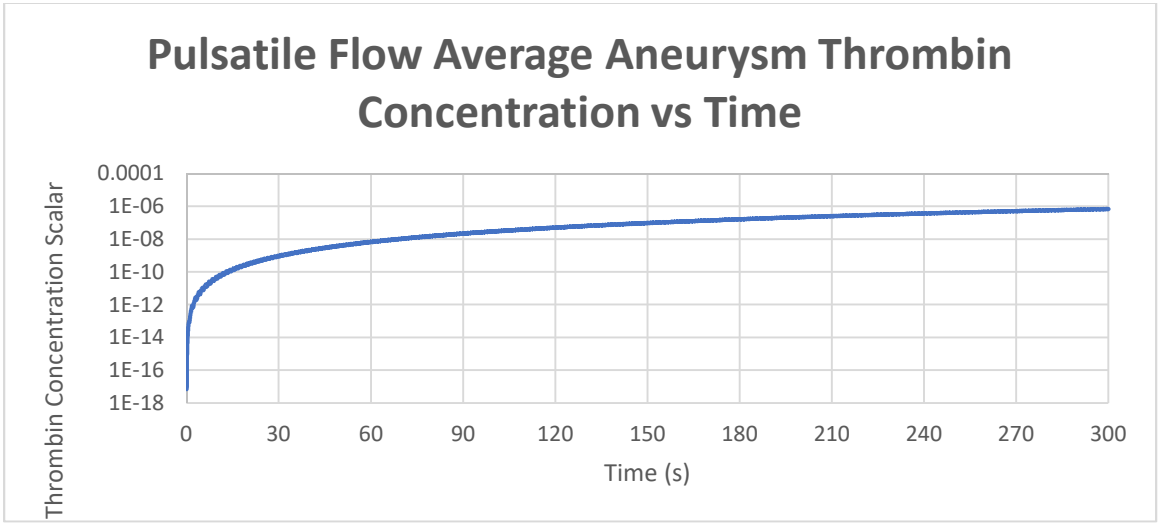

Figure 65: Pulsatile Flow Aneurysm Average Thrombin Concentration Scalar vs Time

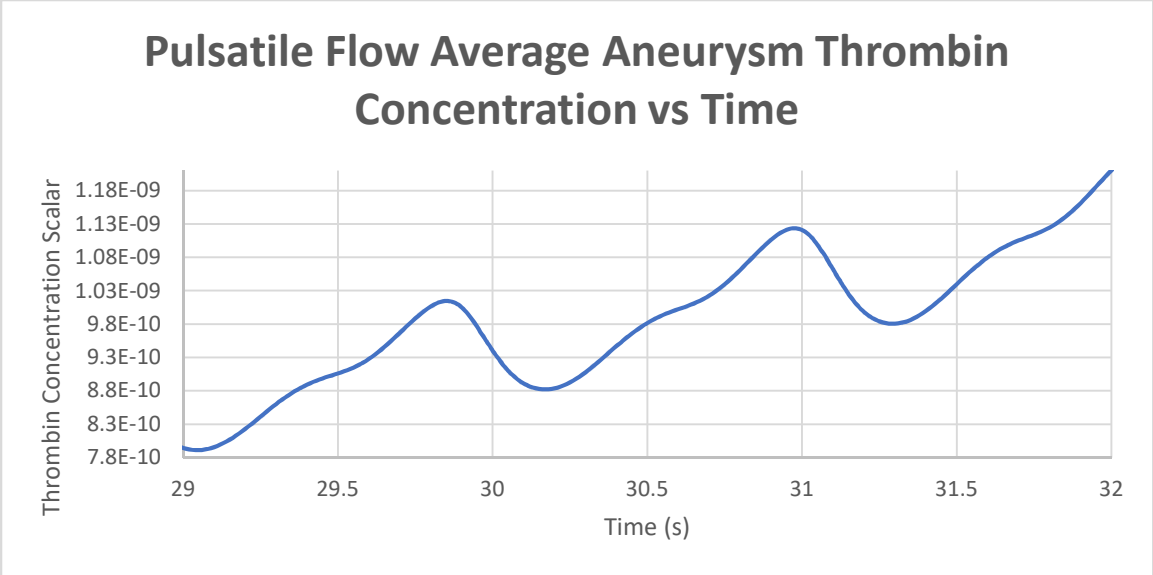

Figure 66: Pulsatile Flow Aneurysm Average Thrombin Concentration Scalar vs Time (29s-32s)

7.2.3.1. Thrombin Concentration Scalar Contour Analysis

As shown in Figures 67 and 68, thrombin concentration between the inlet and the edge of the aneurysm neck most proximal to the inlet is consistently lower than in the rest of the geometry. At the upper-peak of the thrombin concentration scalar, shown in Figure 67, areas of highest thrombin concentration are at the outer half of the aneurysm zone, and near the outlet.

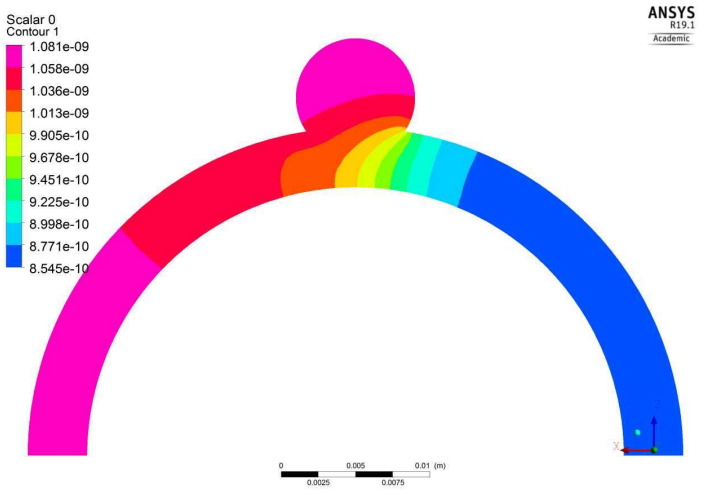

Figure 67: Upper-Peak Pulsatile Flow Thrombin Concentration Scalar at 31.1 Seconds

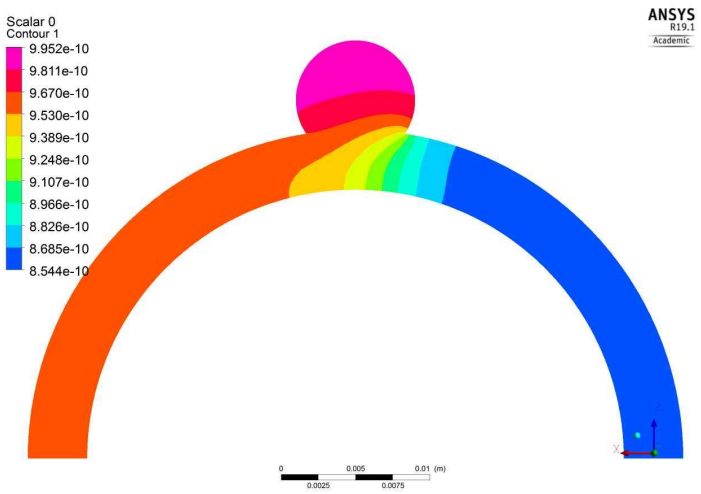

Figure 68: Lower-Peak Pulsatile Flow Thrombin Concentration Scalar at 31.3 Seconds

At the lower-peak's of the thrombin concentration scalar, shown in Figure 68, thrombin concentration at the outlet is still higher than at the inlet, but the thrombin concentration is highest within the top half of the aneurysm zone.

7.2.3.2. Aneurysm Thrombin Concentration Scalar Probe Analysis

Regardless of timestep or peak, thrombin concentration at a given time has a positive relationship with changes in position in the positive x and z directions within the aneurysm zone as shown in Figures 69, 70, and 71. This change appears to be the most drastic along the aneurysm neck. Here thrombin concentration scalar distribution seems to vary at a greater rate at upper scalar peaks than lower scalar peaks. Along Probe B shown in Figure 72, thrombin concentration appears highest near the aneurysm walls, and lowest in the center of the aneurysm.

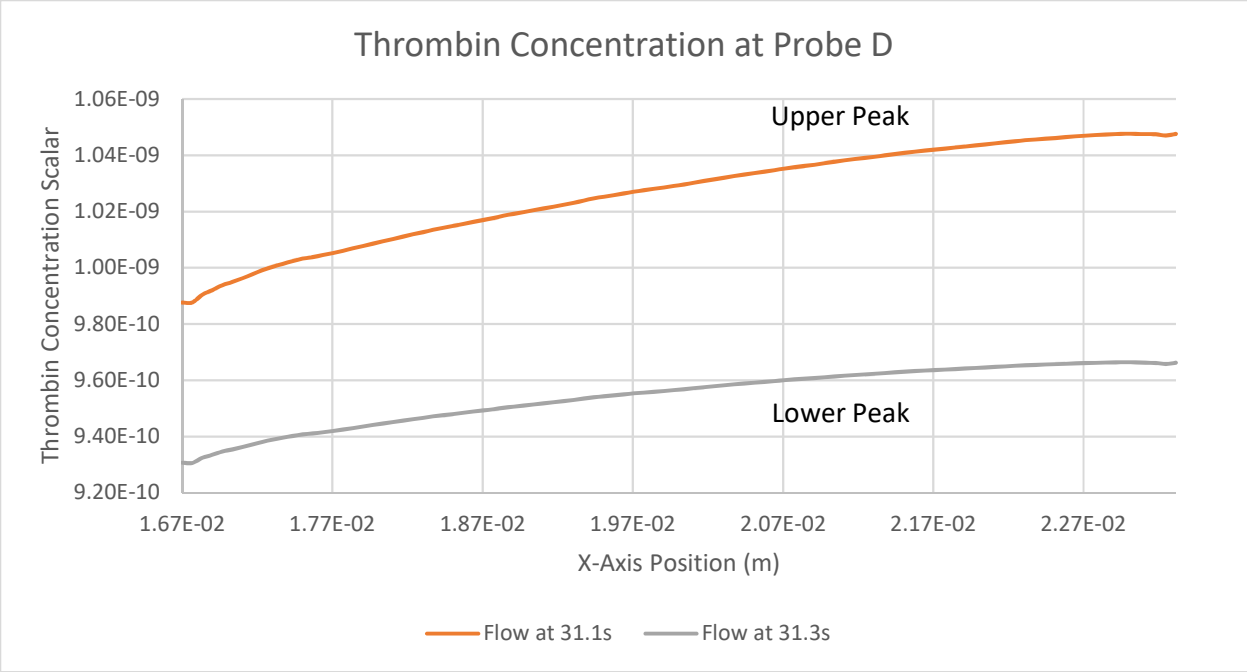

Figure 69: Pulsatile Flow Peak Thrombin Concentration Scalar Distribution at Probe D

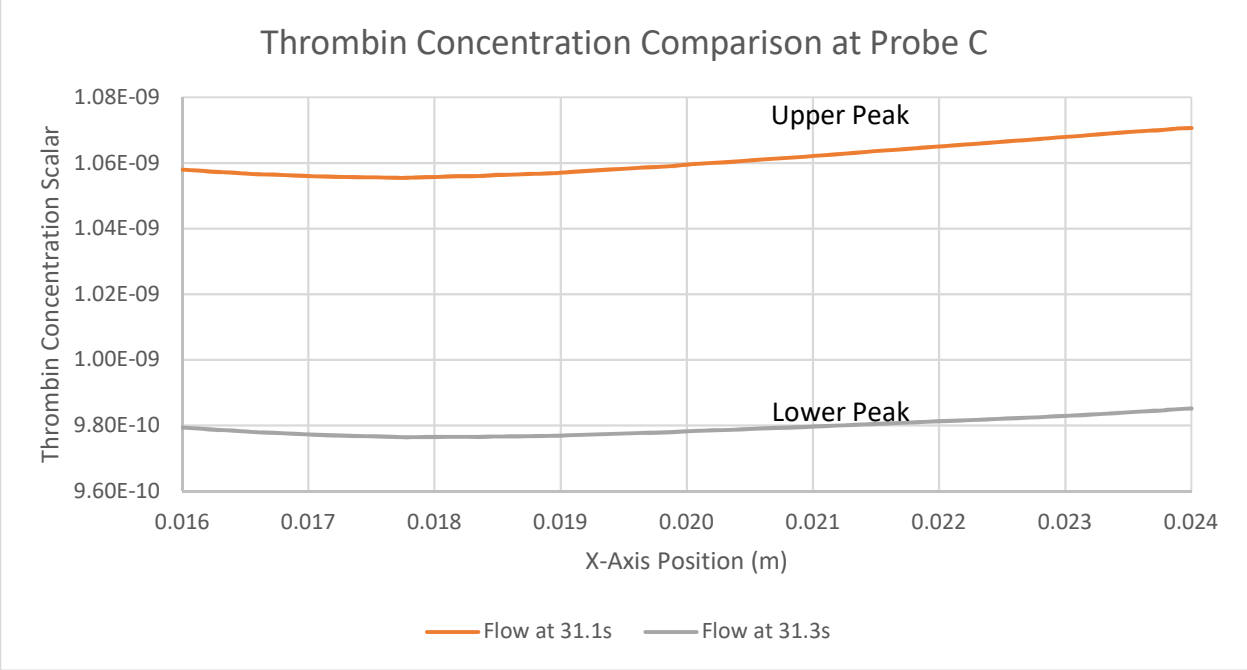

Figure 70: Upper-Peak Pulsatile Flow Thrombin Concentration Scalar Distribution at Probe C

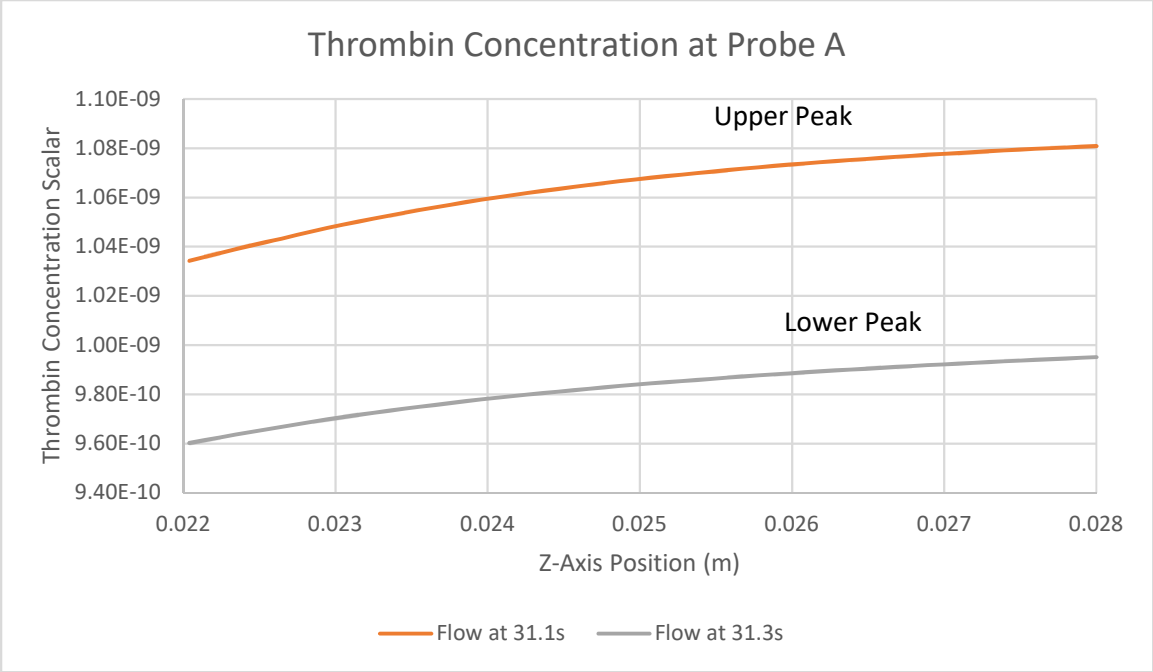

Figure 71: Pulsatile Flow Thrombin Concentration Scalar Distribution at Probe A

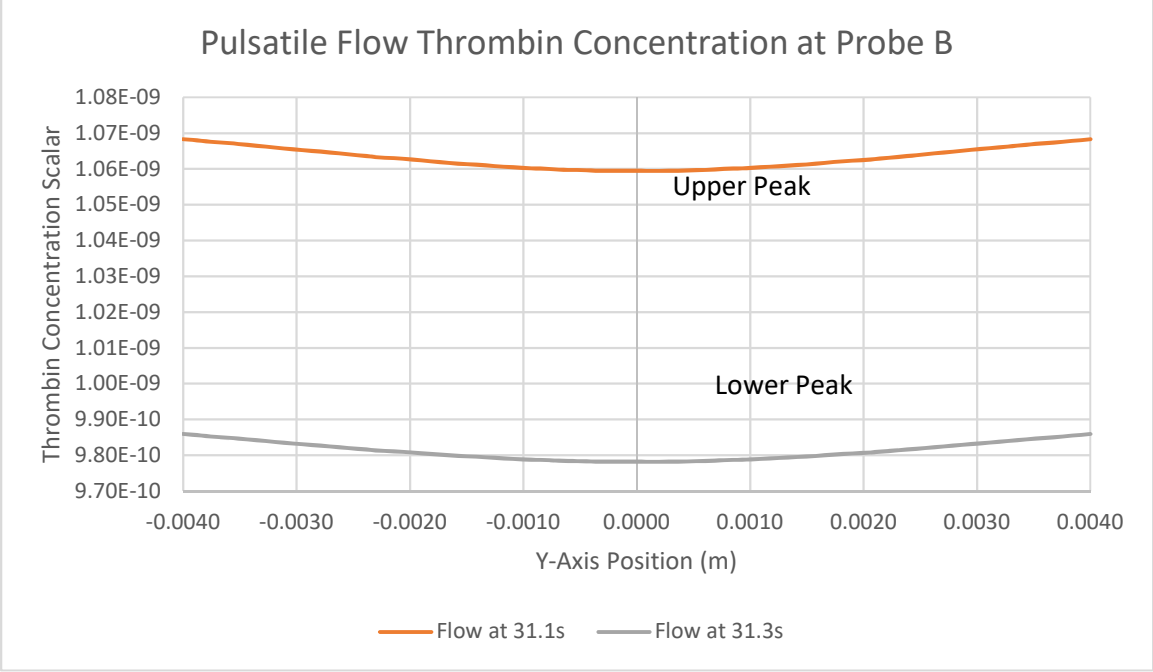

Figure 72: Pulsatile Flow Thrombin Concentration Scalar Distribution at Probe B

7.2.3.3. Clotting Activation

Time (s)	X-Z Plane	Y-Z Plane
29.8	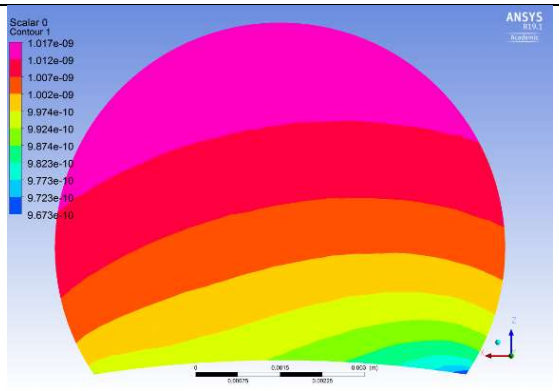	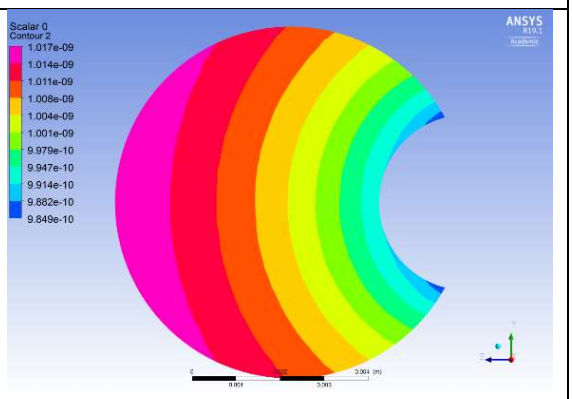
29.9	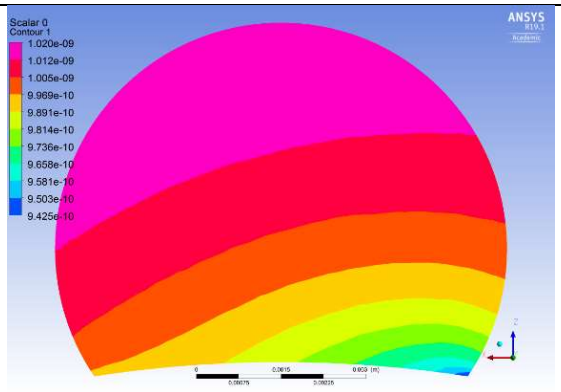	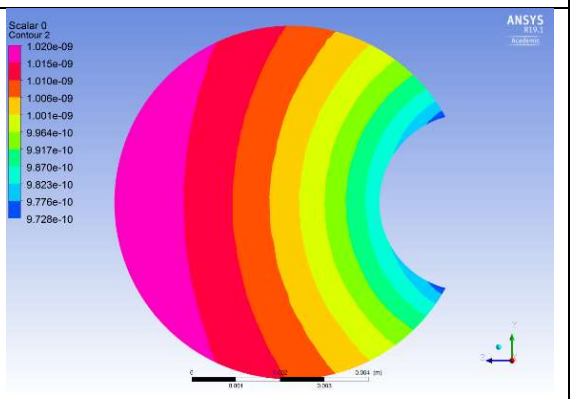

Figure 73: Pulsatile Flow Thrombin Concentration Scalar Aneurysm-Zone Contours at 1st Clot Activation

Thrombin concentration scalar conditions for clotting (scalar = 1e-9) within the aneurysm zone present themselves twice before they become permanent. Illustrated in Figure 73, this happens the first time around 29.8 seconds at the top of the aneurysm when the thrombin concentration scalar is approaching its relative upper-peak. This condition persists to at least 29.9s before the thrombin concentration scalar values in the entire aneurysm dip below 1e-9, and conditions for clotting cease, which is consistent with the average thrombin concentration within the aneurysm vs time illustrated in Figure 66.

The thrombin concentration scalar begins to increase again at 30.5s, and the conditions for clotting present themselves again by 30.6s, allowing for clotting to begin at the top of the aneurysm as illustrated by the contour in Figure 74. Clotting within the entire aneurysm zone becomes possible by 30.8s. After the thrombin concentration scalar peak at 31.1s, thrombin concentration begins to decrease. Clotting conditions diminish by 31.2s and disappear entirely by 31.3s.

Conditions for clotting present themselves a third and final time by 31.4s, and conditions for full clotting within the aneurysm present themselves permanently by 31.6s.

Time (s)	X-Z Plane	Y-Z Plane
30.6	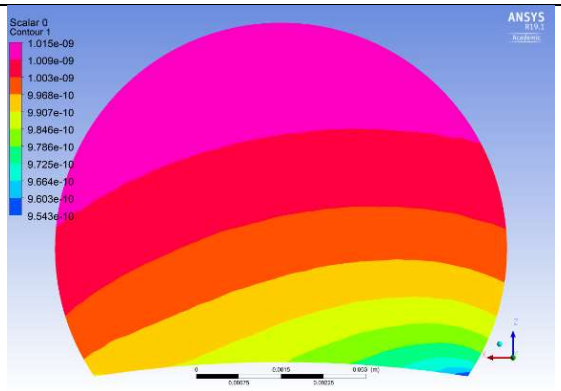	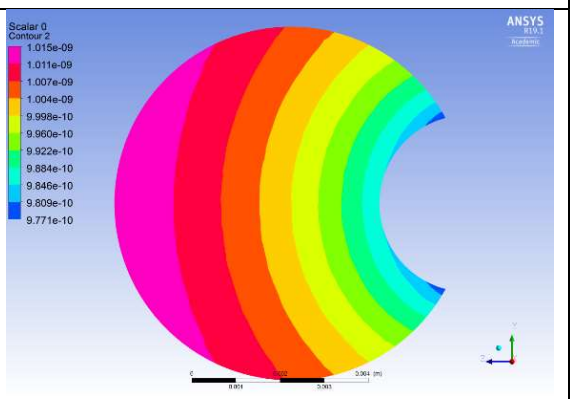
30.8	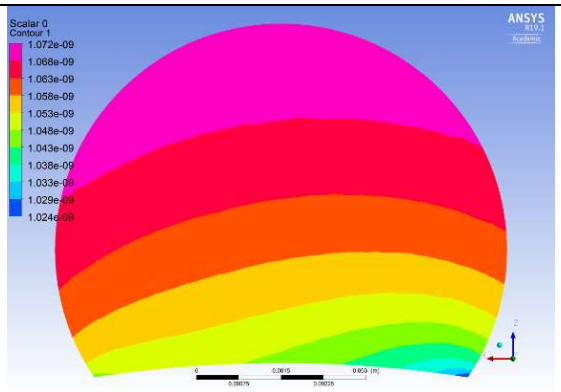	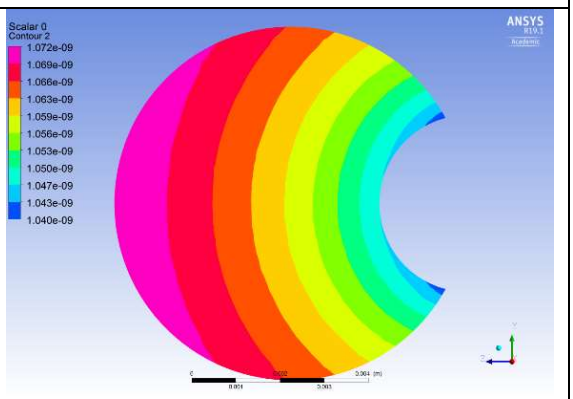
31.2	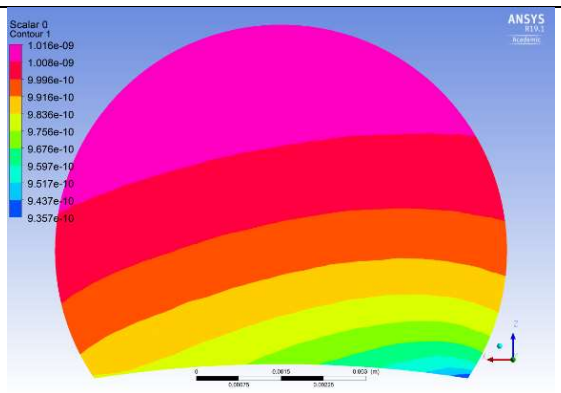	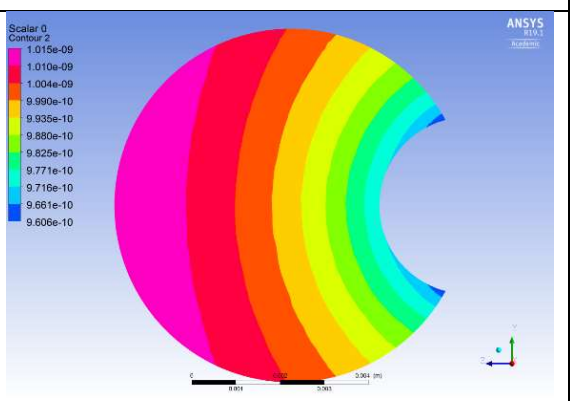

Figure 74: Pulsatile Flow Thrombin Concentration Scalar Aneurysm-Zone Contours at 2nd Clot Activation

7.3. Pulsatile vs Steady Flow Comparison

7.3.1. Average Aneurysm Thrombin Concentration vs Time Comparison

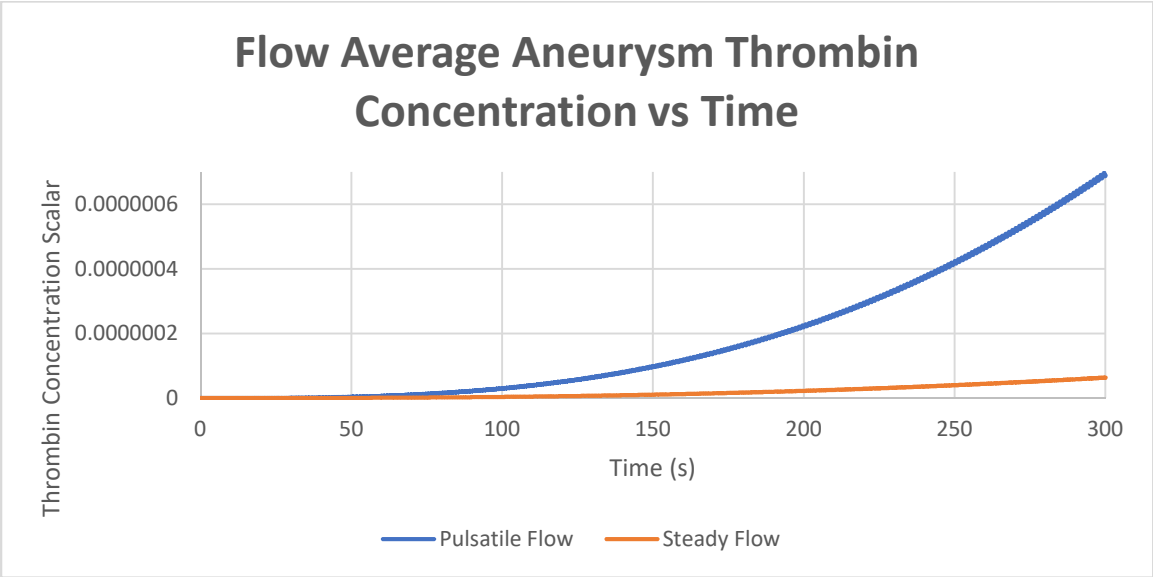

Figure 75: Average Aneurysm Thrombin Concentration vs Time

As is evident from Figure 75, the thrombin concentration scalar increases at a significantly faster rate in the pulsatile flow. Figure 76 illustrates the difference in thrombin concentration rates between pulsatile and steady flow. Pulsatile flow locally exhibits quasi-periodic nature as opposed to steady flow, which exhibits more linear features.

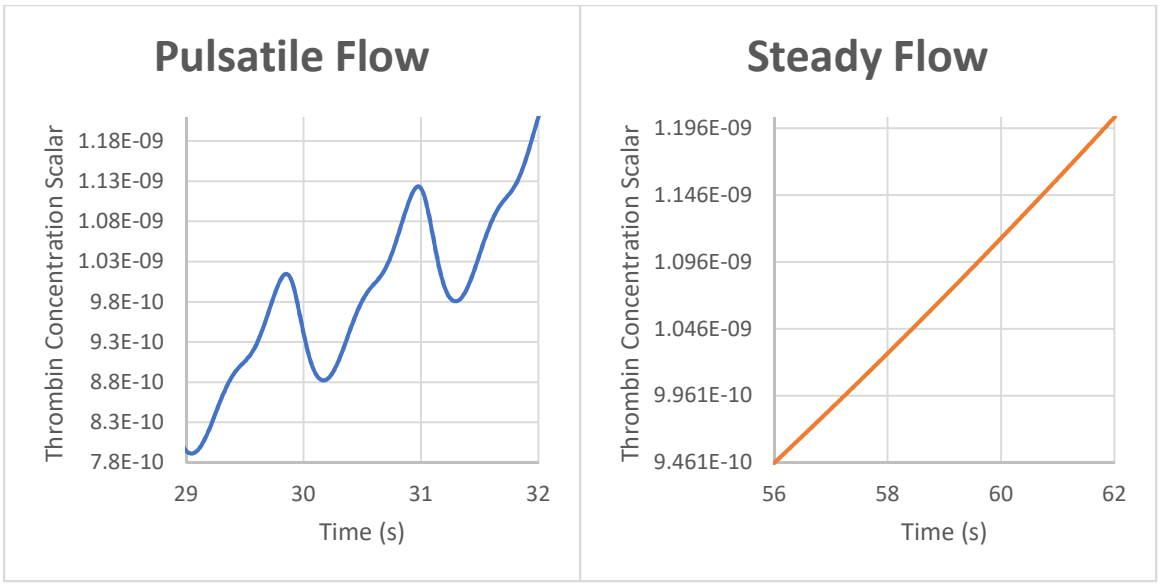

Figure 76: Clotting Conditions Timeline Comparison

7.3.2. Velocity Probe Distribution Comparison

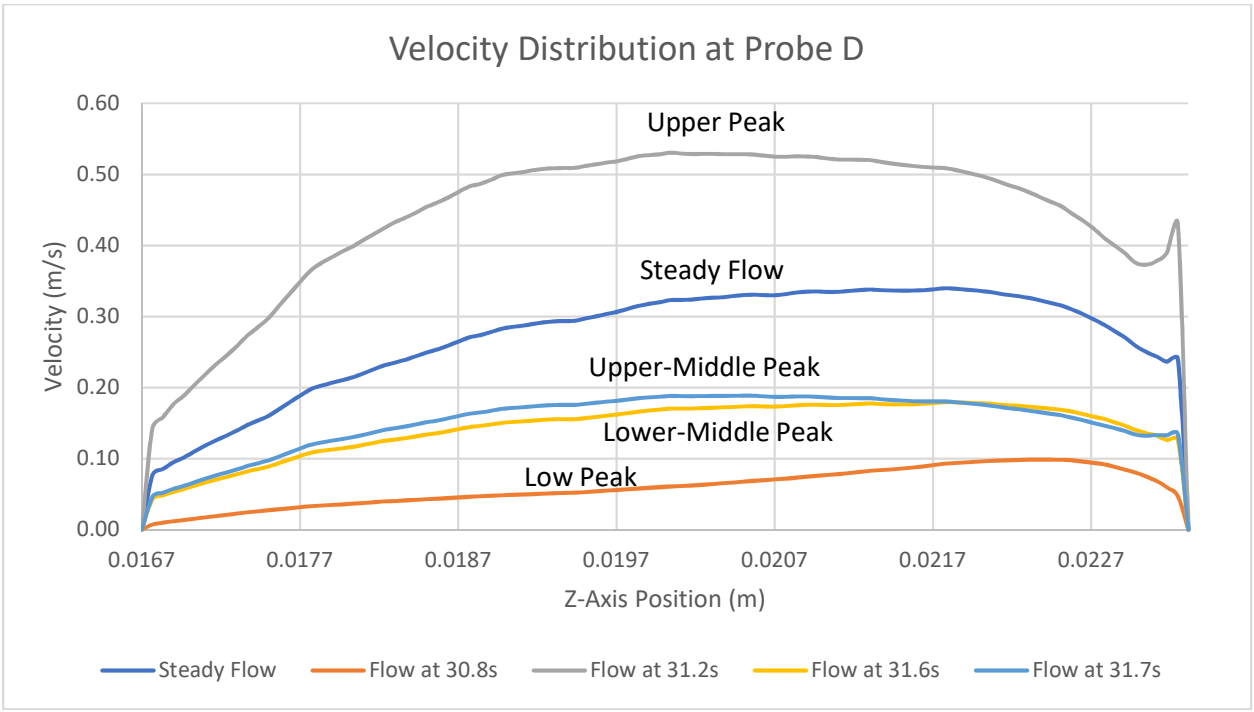

Figure 77: Flow Velocity Distribution Comparison at Probe D

As illustrated in figures 77 and 78, steady flow behaves similarly to the upper velocity peak of pulsatile flow, where magnitude is highest on Probe C and Probe D, the more proximal it gets to the outlet. This is true on Probe C to such an extent that steady flow velocity is of similar magnitude to the upper velocity peak of pulsatile flow, extending all the way to the other end of the probe as shown in Figure 79. This means that on average velocity is higher at the wall most proximal to the outlet for the steady flow simulation, but average velocity at the opposite side of the aneurysm wall most proximal to the inlet is higher for the pulsatile flow simulation.

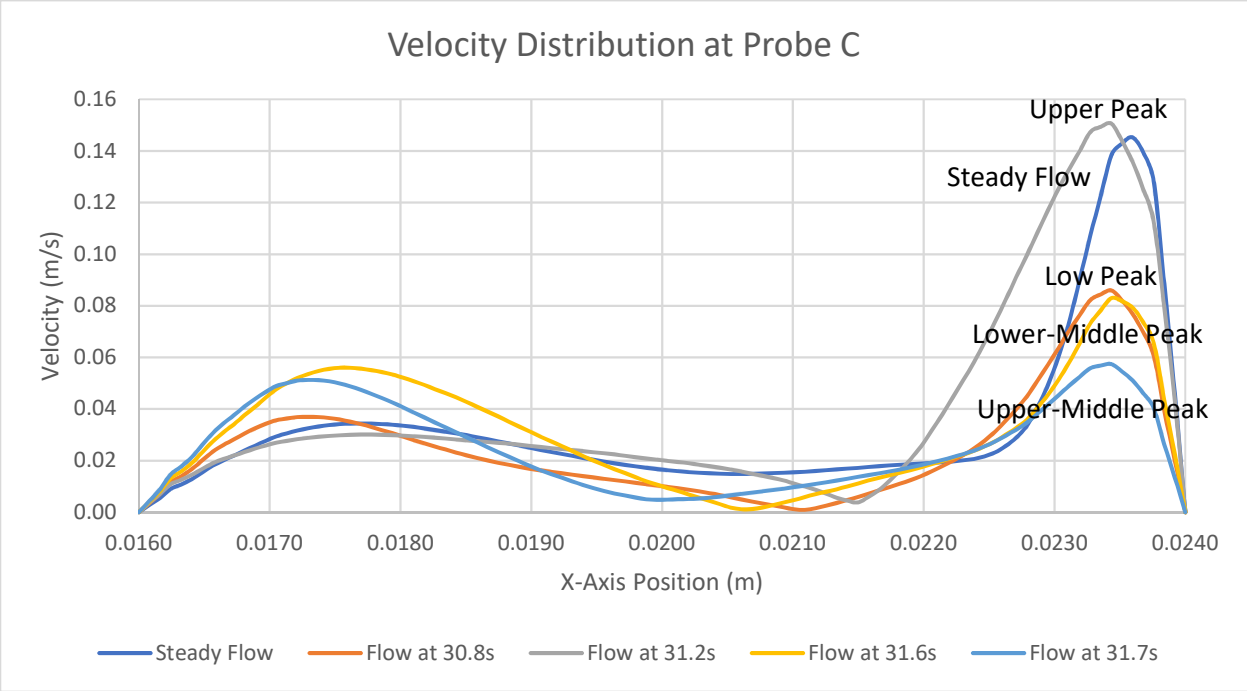

Figure 78: Flow Velocity Distribution Comparison at Probe C

On the Probe A shown in Figure 80, steady flow velocity is nearly the mean of the upper and lower velocity peaks where the artery connects with the aneurysm, suggesting that average flow in this region is nearly identical between the two simulations. This behavior differs with movement along Probe A, where at the top of the aneurysm shown in Figure 81 steady flow velocity is higher than both the high and low pulsatile velocity peaks, but lower than the upper-middle and lower-middle pulsatile velocity peaks. This suggests that velocity is higher on average for steady flow in this region than pulsatile flow, given that velocity remains low in this region between the lower and upper pulsatile velocity peaks, and increases above steady flow only briefly between the upper and lower velocity peaks.

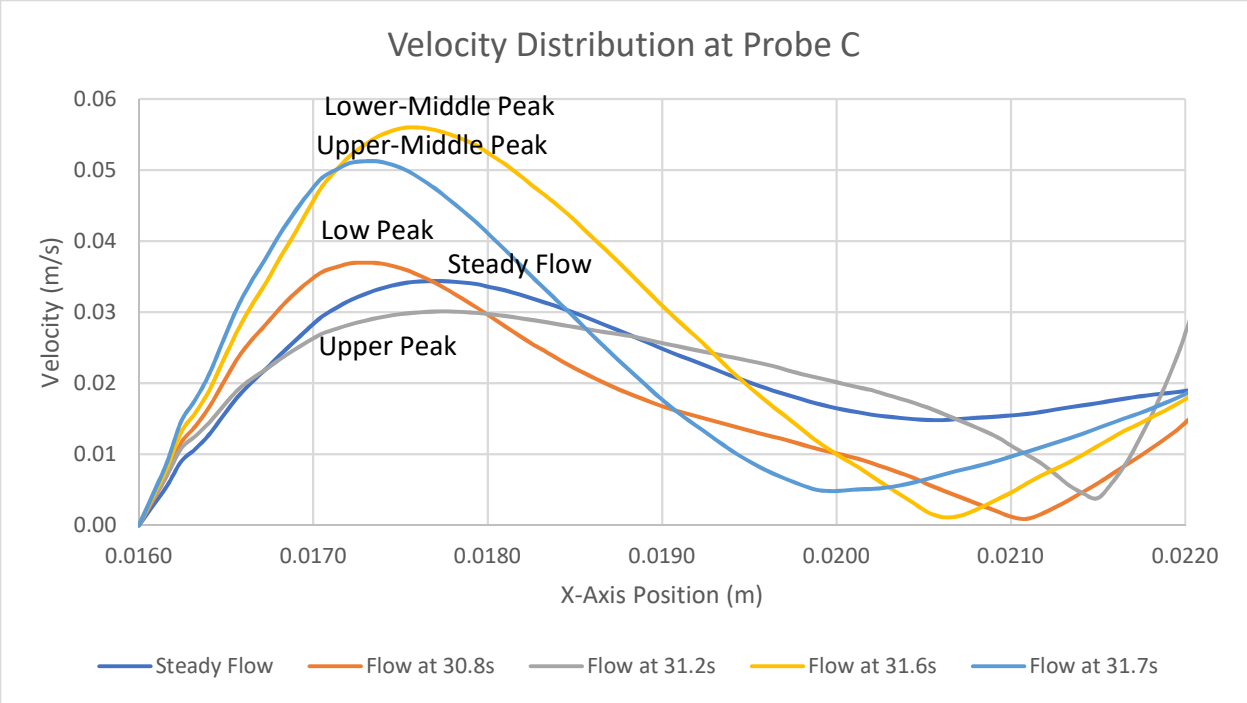

Figure 79: Flow Velocity Distribution Comparison at Low Velocity Side of Probe C

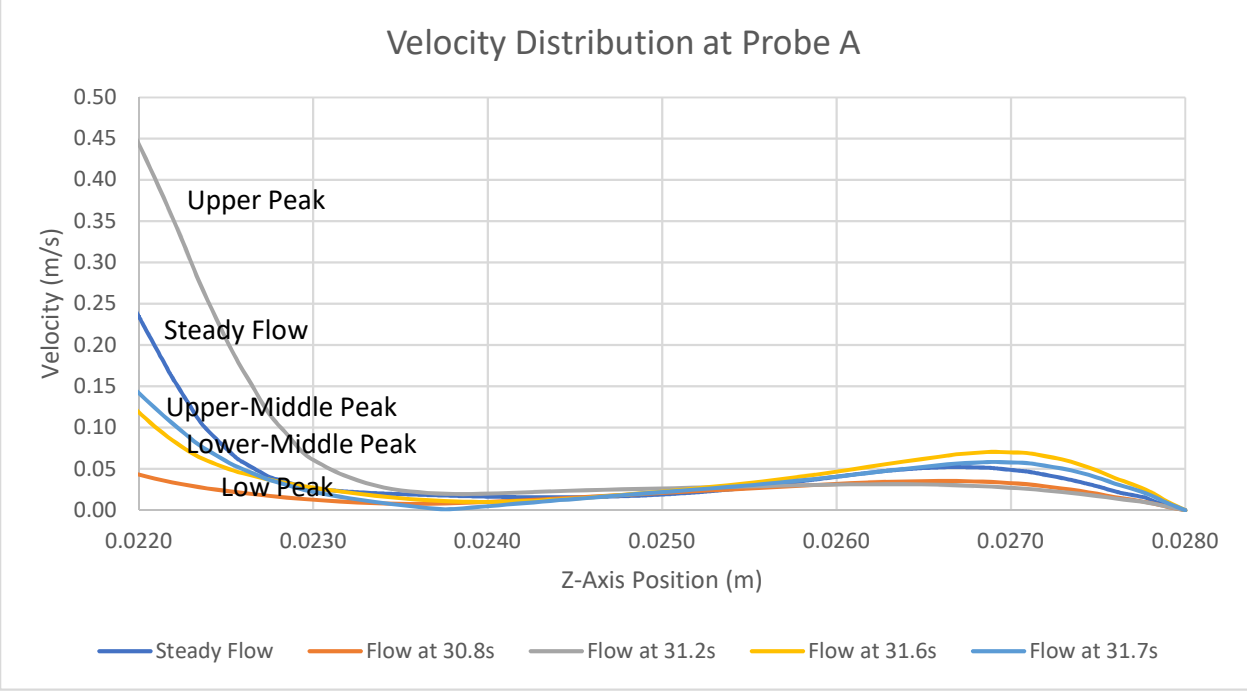

Figure 80: Flow Distribution Comparison Probe A

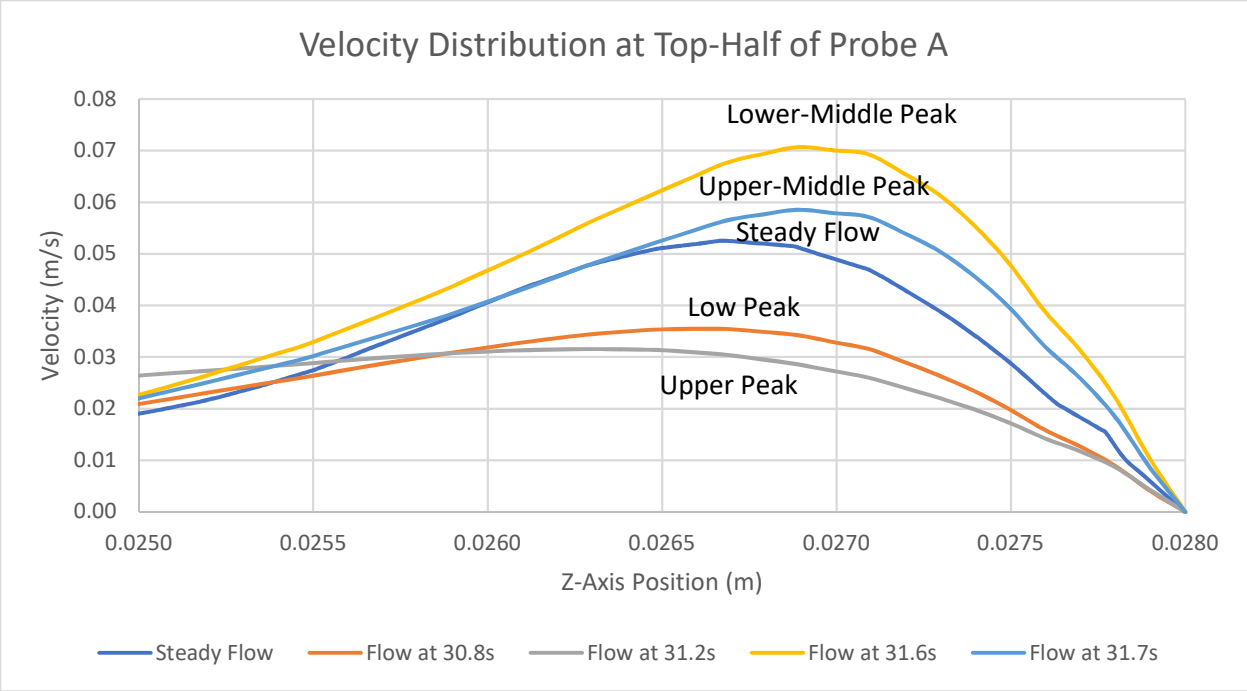

Figure 81: Flow Distribution Comparison at Top Half of Probe A

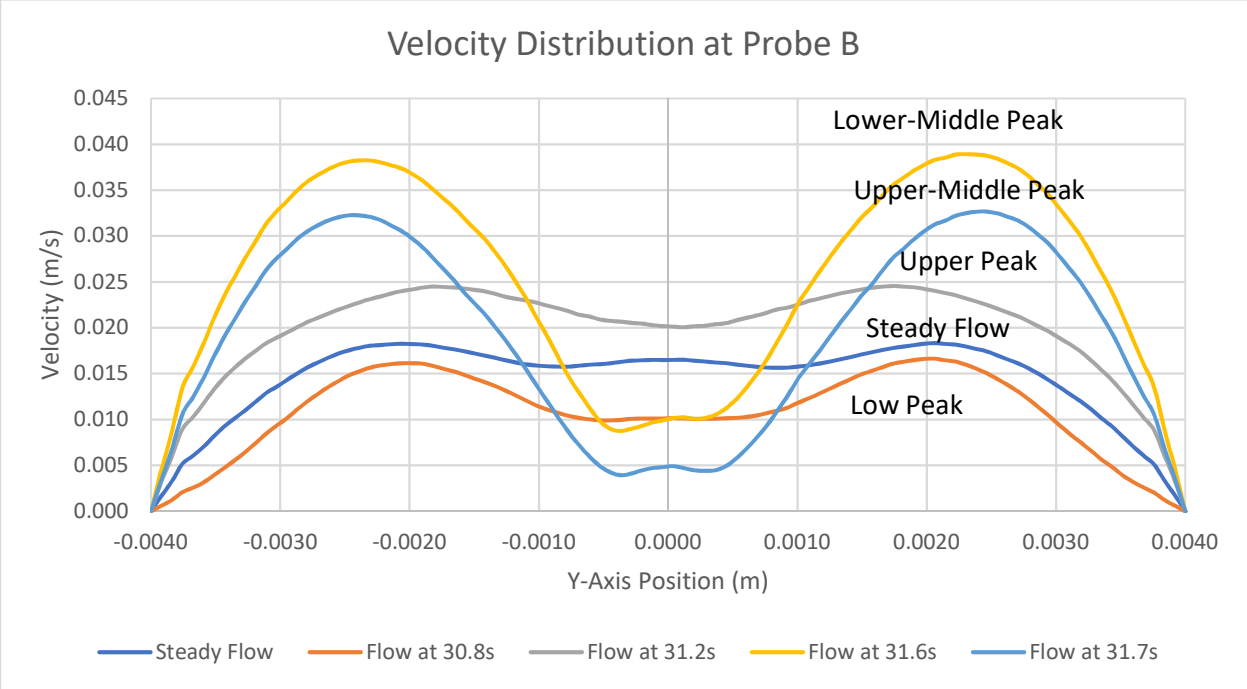

Figure 82: Flow Velocity Distribution Comparison at Probe B

According to Figure 82, velocity is on average higher in magnitude along the y-axis probe towards the aneurysm wall in pulsatile flow than in steady flow. Figure 83 shows that steady flow velocity is better distributed across the y-axis of the aneurysm than pulsatile flow and is on average higher in the center of the aneurysm than steady flow.

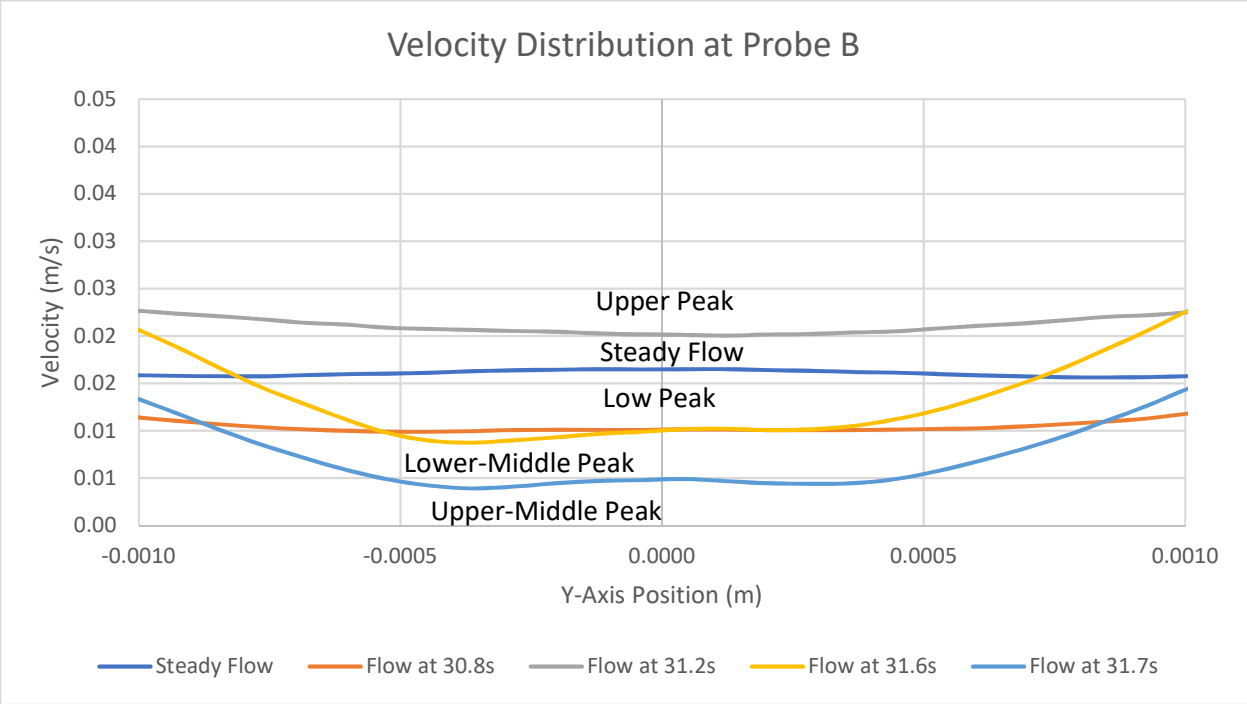

Figure 83: Flow Velocity Distribution Comparison at Center of Probe B

7.4. PIV Simulation Contour Comparison

According to the average deviation of the 2D and 3D PIV simulations listed in Table 9 for the locations shown in Figure 27, magnitude of velocity is similar between the output of the PIV experiment and the simulations. Deviation from the experimental results appears reliably for both the 2D and 3D case in the flow direction most perpendicular to the overall flow profile at a particular location, particularly the U-velocity at location 1, and V-velocity at locations 4 & 7. This behavior is not consistent at the outlet, where both the 2D and 3D PIV simulations deviate by nearly 30% in the V-direction, and more than 26% velocity magnitude deviation. Other anomalous behavior occurs at location 3 where V direction velocity significantly deviates from the experimental results for both the 2D and 3D PIV simulations by more than 80%.

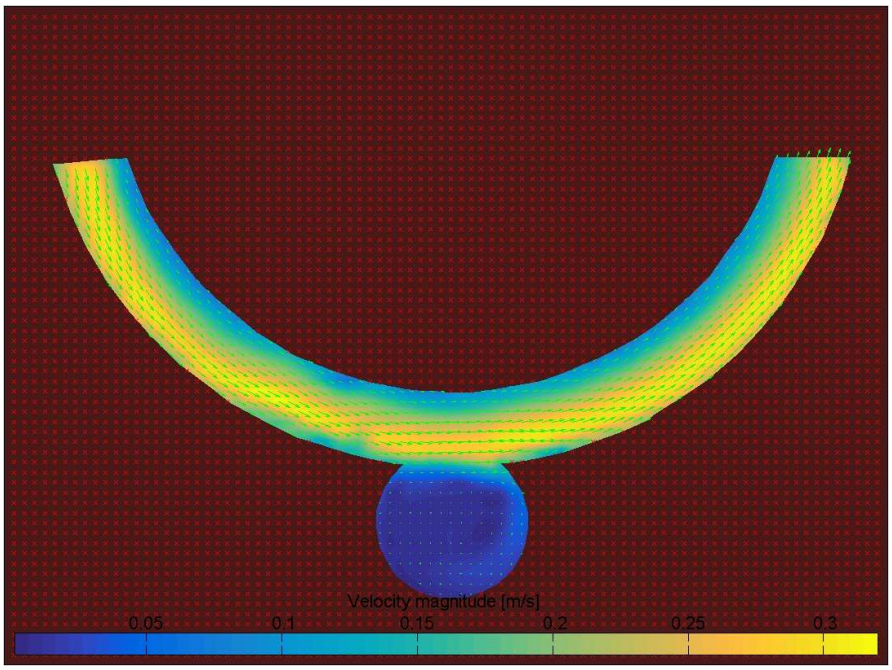

Figure 84: PIV Velocity Results

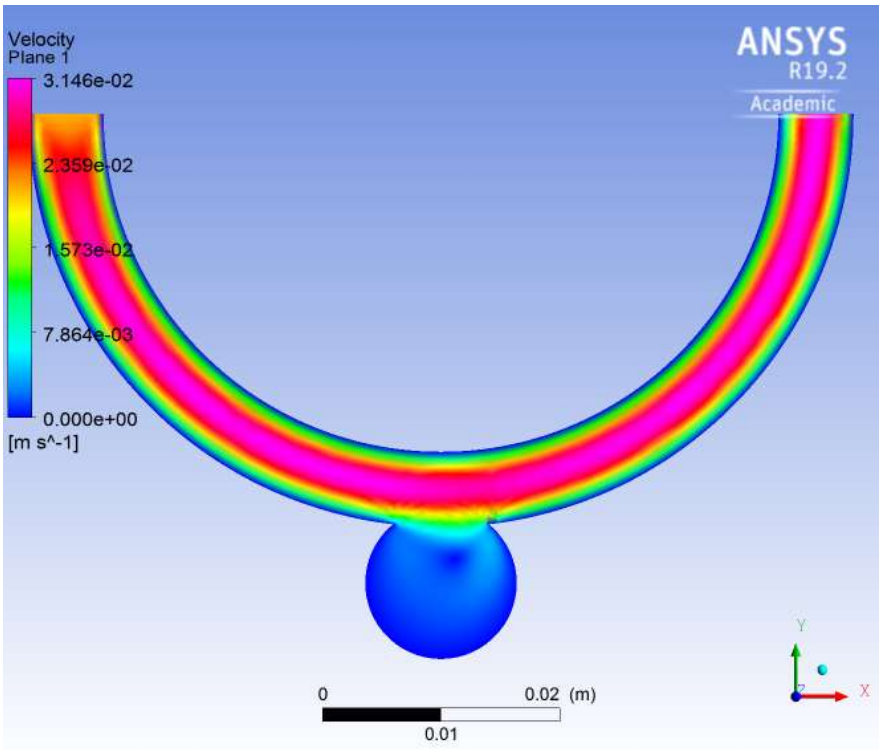

Figure 85: 2D PIV Simulation X-Z Plane Velocity Contour

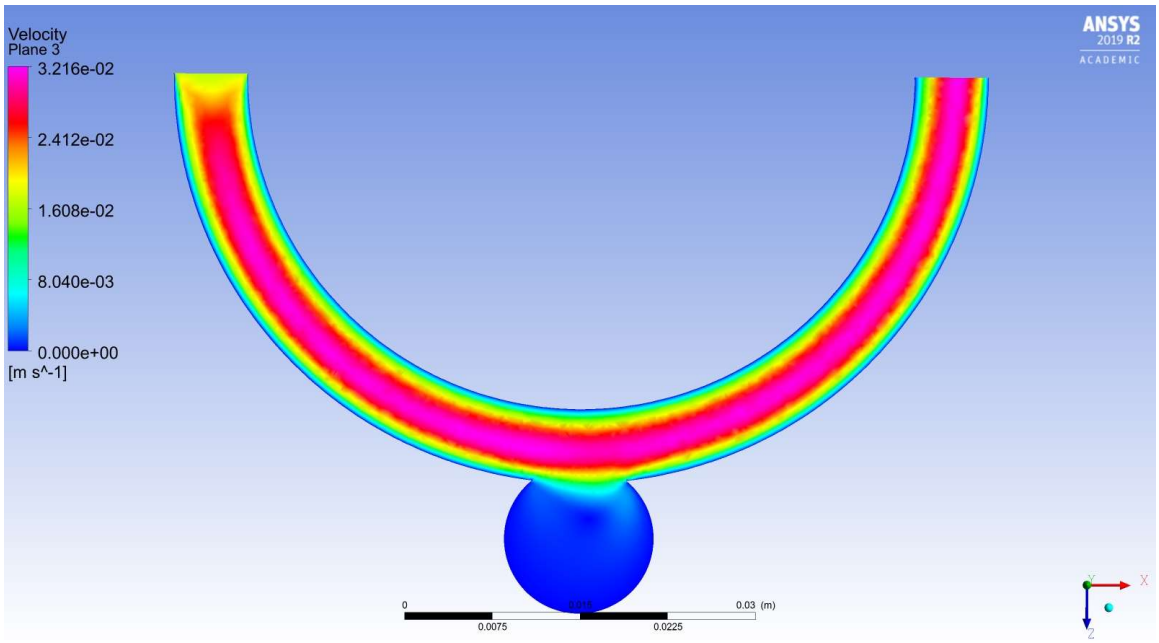

Figure 86: 3D PIV Simulation X-Z Plane Velocity Contour

Deviation is the highest across location 6 between the 2D PIV simulation and the PIV experiment. This difference is visually apparent in the contours shown in figures 84 & 85, where the flow appears largely similar, save for within the aneurysm zone. The velocity vectors shown in Figures 87-89 further highlight the differences in flow within the aneurysm zone between the PIV experiment results, 2D PIV simulation results, and 3D PIV simulation results. In particular, the point about which recirculation occurs within the aneurysm zone is in a different location for the PIV simulations, and the PIV experiment. In the PIV experiment results, the center of recirculation appears near the aneurysm zone wall most proximal to the outlet and away from the neck of the aneurysm. The 2D and 3D PIV simulation results by comparison indicate that the center of recirculation is in the bottom-half of the aneurysm and most proximal to the outlet. The distance and deviation and of the center of recirculation of the PIV simulations from the PIV experiment are recorded in Table 10.

Deviations between the computational and experimental contours shown in Figures 84-86 appear at the walls, where velocity is significantly lower in the simulations than in the PIV experiment. Overall the computational PIV simulations appear to have velocity profiles evenly distributed between the artery wall boundaries, where the maximum velocity for the PIV simulations appear to be at roughly the centerline of the artery zone. The experimental PIV contours by contrast indicate that high velocity flow tends

towards the outer wall of the artery-zone, and low velocity flow tends more towards the inner-wall of the artery-zone.

	2D PIV Simulation Deviation			3D PIV Simulation Deviation		
	Velocity U-Direction	Velocity V-Direction	Velocity Magnitude	Velocity U-Direction	Velocity V-Direction	Velocity Magnitude
1	16.85%	4.47%	5.12%	1.73%	4.72%	4.51%
2	12.17%	5.46%	8.57%	6.93%	10.49%	8.83%
3	16.14%	80.10%	9.44%	20.03%	86.45%	9.15%
4	6.00%	14.16%	3.86%	6.84%	0.23%	6.03%
5	6.58%	35.95%	1.96%	2.73%	418.71%	2.05%
6	541.34%	95.67%	68.12%	86.03%	123.20%	16.18%
7	0.91%	40.55%	1.25%	1.12%	19.99%	2.01%
8	2.01%	21.36%	10.83%	7.84%	16.76%	11.83%
9	2.08%	14.95%	7.90%	7.87%	13.16%	10.18%
10	7.29%	30.71%	26.56%	7.14%	30.09%	27.43%
Total	**2.27%**	**26.60%**	**8.50%**	**1.52%**	**162.83%**	**8.36%**

Table 7: Average Deviation of PIV Simulations from Experimental PIV Results

	X Distance (mm)	Y Distance (mm)	X Deviation	Y Deviation
2D PIV Simulation	-2.3529	2.9658	6.69%	7.33%
3D PIV Simulation	-2.6878	2.5385	7.64%	6.27%

Table 8: Distance of PIV Simulation Results from PIV Experiment Results

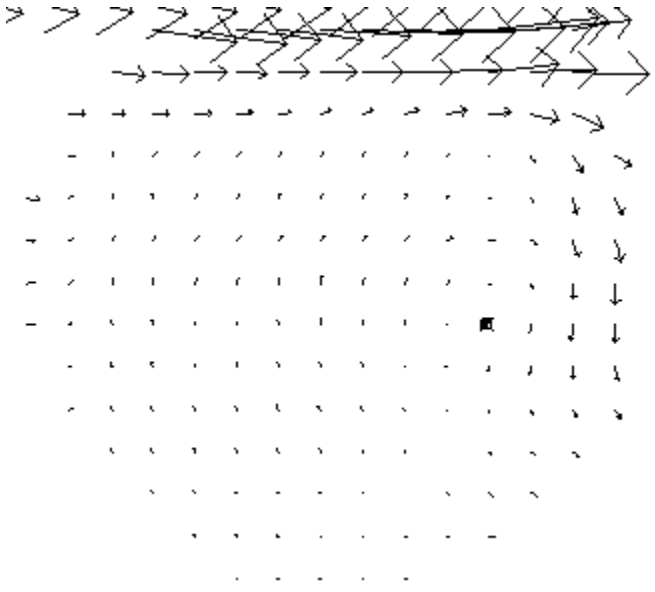

Figure 87: PIV Experiment Center of Recirculation (highlighted in black)

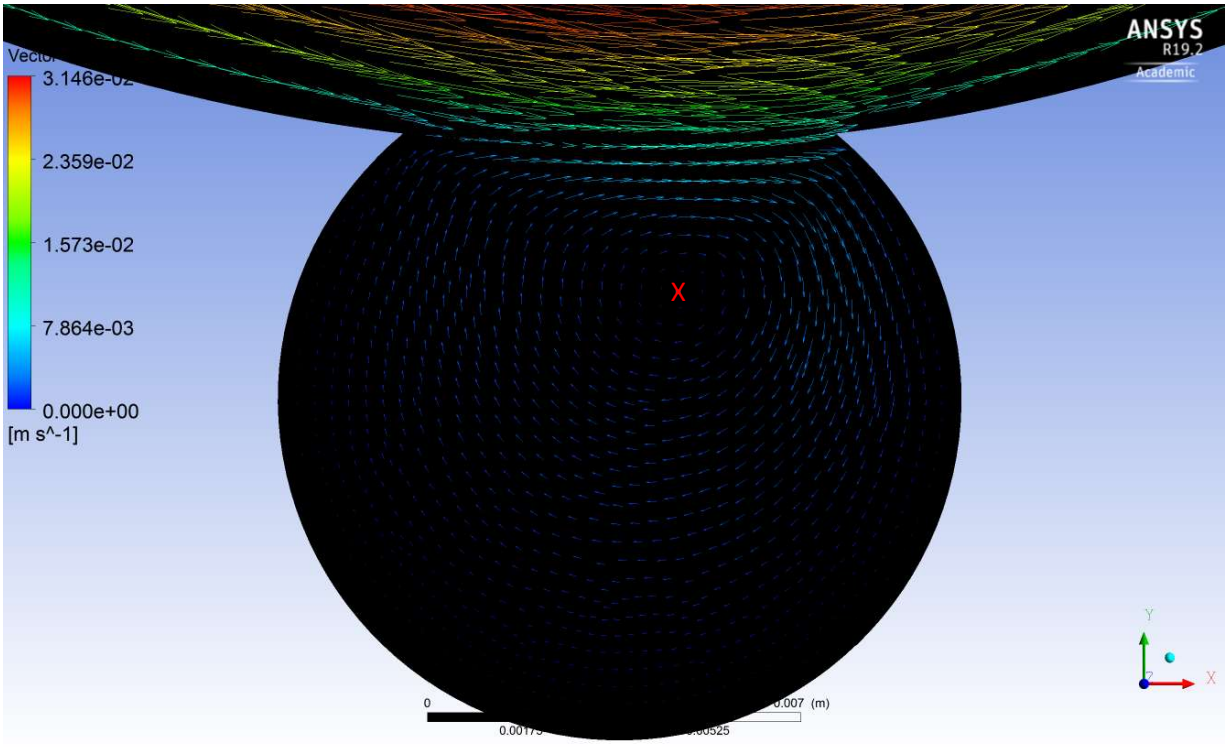

Figure 88: 2D PIV Simulation Aneurysm Zone Center of Recirculation

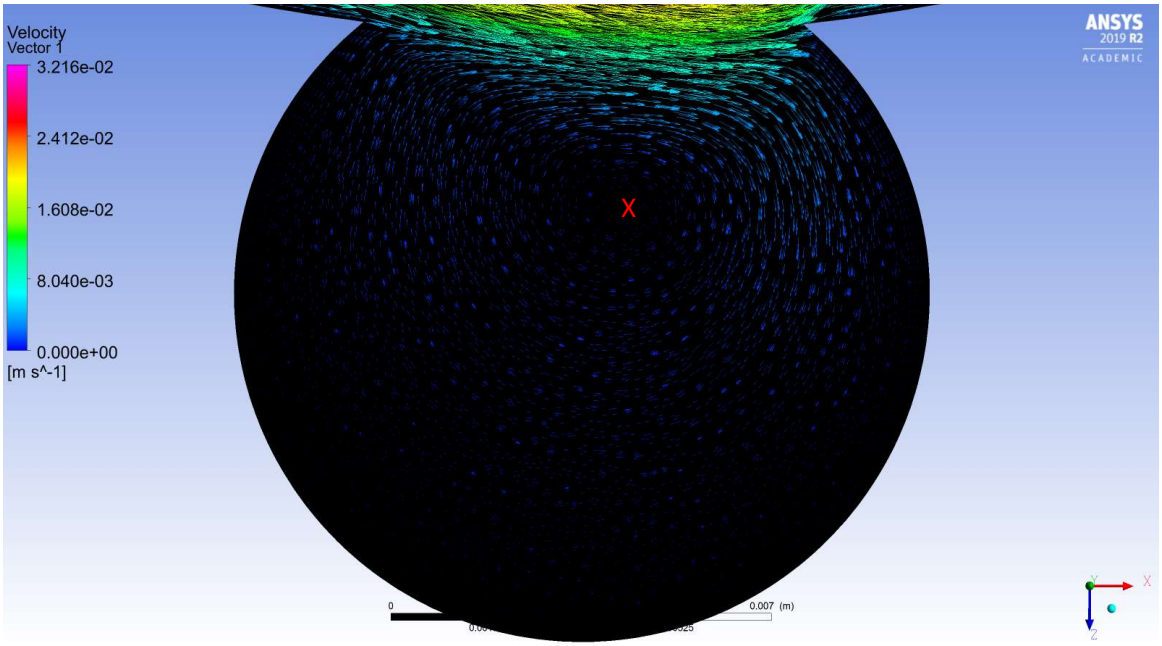

Figure 89: 3D PIV Simulation Aneurysm Zone Center of Recirculation

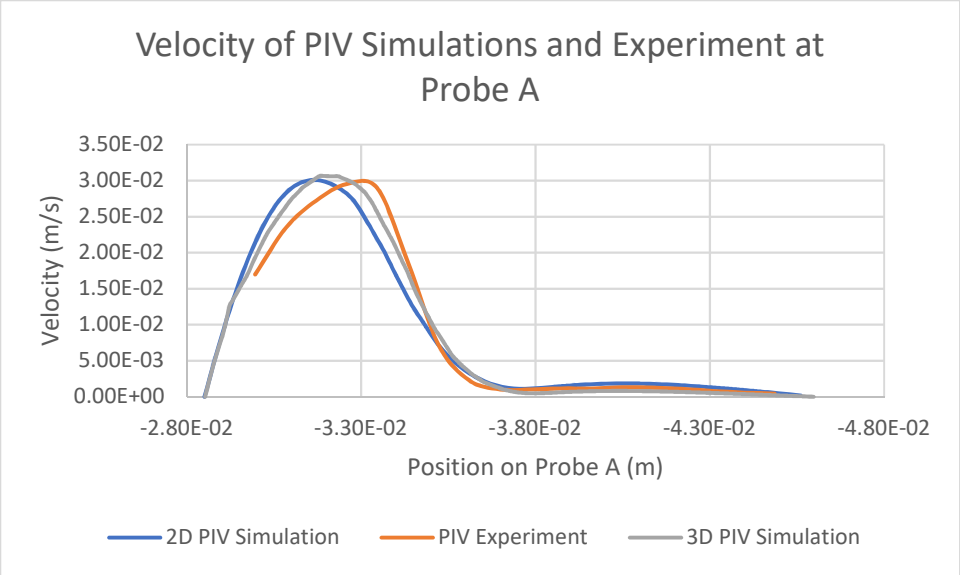

Figure 90: PIV Flow Velocity Distribution Comparison at Probe A

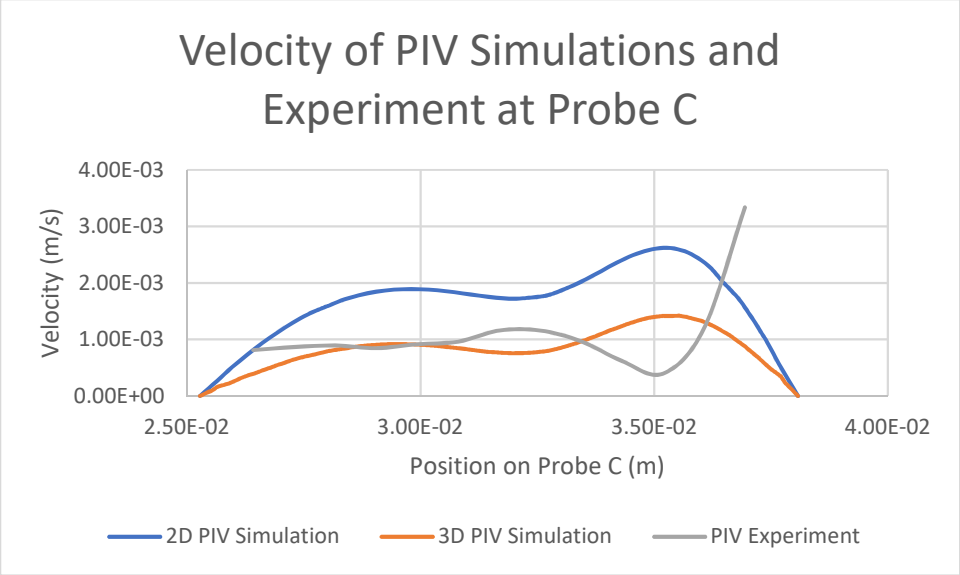

Figure 91: PIV Flow Velocity Distribution Comparison at Probe C

At Probe A the flow velocity distribution of the PIV experiment is like that of the PIV simulations, where the velocity peaks are offset from one another, and the 3D PIV simulation bears the most resemblance with. Along Probe A within the aneurysm-zone, the 3D PIV simulation results are slightly lower than the experimental results, where the 2D PIV simulation results are slightly higher. Figure 91 shows that the 2D

and 3D PIV simulation are similar in profile shape to one another, but do not represent the flow profile of the PIV experiment results.

8. Discussion

8.1. Pulsatile Flow

Flow within the artery fluctuates, and areas of high and low velocity reliably shift dependent upon the time within a pulse. The flow profile within the aneurysmal geometry fluctuates drastically. When the pulsatile velocity function hits its low peak, flow velocity is almost uniformly low within the aneurysmal sac. During high velocity peaks however, flow increases significantly within the aneurysm, creating a flow profile of similar shape to the steady flow function with nearly double the velocity.

The average thrombin concentration scalar exhibits a quasi-periodic behavior, in which the lower peak of the thrombin concentration scalar occurs between the lower and upper pressure peaks, and the upper peak of the thrombin concentration scalar occurs just after the upper pressure peak. This theoretically would cause clotting equations to activate and then deactivate twice before activating permanently in this simulation.

Also, of note, is the reversal in the gradient of pressure just after the lower pressure peak. This implies that flow velocity is briefly influenced by pressure to decrease, rather than solely by the velocity inlet function. It is worth noting that the timesteps at which the reversal happens are convergent, and do not themselves indicate anything peculiar about this behavior.

8.2. Thrombin Concentration Scalar Comparison Between Pulsatile and Steady Flow

The thrombin concentration scalar value required to activate clotting within the aneurysm is reached in about half the time when using pulsatile flow over steady flow. Factors that may contribute to this are related to diffusion of the thrombin concentration scalar and recirculation within the aneurysm. In the pulsatile flow simulation, velocity magnitude periodically goes from low to high, causing variable flow patterns within the aneurysm geometry by comparison to the steady flow function. This results in a less evenly distributed flow within the aneurysm for pulsatile flow, as well as lower average velocity near the walls of the aneurysm. Since pulsatile flow results in less flow near the aneurysm wall, it may aid the mass-flux defined scalar within the aneurysm in recirculating within the aneurysmal sac rather than being pushed out into the main flow-stream in the artery.

Figures 77 and 80 show that in the region where the aneurysm meets the artery, velocity is highest at the upper peak of pulsatile flow. Referencing Figure 66, it is around this peak that the average thrombin concentration scalar value within the aneurysm plunges. Looking back at Figures 77 and 80, as well as 78 and 81, this is when the distribution of velocity within the cerebral aneurysm of the pulsatile flow simulation most closely represents the shape of the distribution of velocity in the steady flow simulation, where velocity is notably highest across the aneurysm neck and at the aneurysm wall proximal to the outlet, and velocity is notably well distributed across the y-axis. This indicates that higher, more distributed flow within the aneurysm at the upper velocity peak pushes thrombin that was recirculating within the aneurysm outside into the artery, causing a thrombin concentration drop within the aneurysm. It is conceivable that if this occurs continuously in steady flow, it would take significantly longer for enough thrombin to build up within the aneurysm to activate the clotting process than with pulsatile flow. It should be noted that the upper-peak velocity poorly represents the velocity distribution of steady flow across Probe A shown in Figures 80-81. This appears to suggest that the distribution of flow across the y-axis of the aneurysm is a more important factor when considering the rate at which thrombin generates within the aneurysm, where better distributed flow appears to correlate with lower thrombin retention within the aneurysm.

There is little research against which these results can easily be compared, though Oured et al.'s intracranial aneurysm thrombosis model using a lattice Boltzmann numerical algorithm utilizes a pulsatile pressure outlet, and appears to have a similar distribution of thrombin throughout a similarly shaped ideal large aneurysm. However, available data from Oured et al. does not mention the amount of time taken to reach this concentration. Regardless, the available results give insight into the possible clotting outcome for the presented cerebral aneurysm model inclusive of pulsatile flow.

From the data gathered pulsatile flow likely has a significant effect on Ngoepe et al.'s overall computational model of thrombosis for cerebral aneurysms. Aside from causing the fibrin clots to begin development significantly faster, pulsatile flow may similarly trap and concentrate the fibrin clots (proteins responsible for biochemical reactions) and antithrombin. This conceivably could cause the clotting process to start and finish significantly faster than under steady flow conditions. It is also possible that the area of clot development would shift if pulsatile flow was applied with Ngoepe et al.'s computational model.

Ngoepe et al. present a figure comparing the surface bound tissue factor results vs time against the tissue factor results of Buetenas et al.'s experimental work. The surface-bound tissue factor results of Ngoepe

et al. have a steeper curve than that of Buetenas et al. Barring the 2D nature, complicated biochemical processes, and other unknown quantities that may not be entirely accounted for in Ngoepe et al.'s computational model, the difference between Buetenas et al.'s experimental work, and Ngoepe et al.'s computational model is that the generated surface-bound tissue factor occurred in two different environments; a static environment and steady flow environment, respectively. Should this difference be a major factor in the shape of the curve of surface-bound tissue factor, the same experiment with pulsatile flow may produce a steeper curve than with steady flow. This in turn would mean it would take less time to reach the surface-bound tissue factor peak value if a pulsatile waveform was applied in the idealized geometry.

8.3. PIV Simulation and Experimental Comparison

According to the comparison of the 3D PIV simulation results to the PIV experiment results, the steady flow model applied for the thrombin concentration scalar comparison is accurate with 8.36% deviation from realistic flow when considering the average of velocity magnitude, 1.52% when considering the average of U-direction velocity, and 162.83% when considering the average of V-direction velocity. The points that make up location 6 on Figure 27 indicate that the aneurysm zone some deviation from realistic flow. When compared to the corresponding vector plots in Figures 87 & 89, this deviation makes sense, since the center of recirculation is in a different place in each vector plot. Inconsistency between the simulation and the experimental distribution of velocity within the artery zone is likely due to the no-slip condition applied to the wall boundaries for the steady flow model. This may also explain the large deviation at location 10 in Figure 27, since it lacks enough points to aptly compare the average experimental velocity with the average velocity of the computational results across that cross-section. This occurred because points near the boundary walls were omitted from evaluation due to their questionable accuracy in PIV studies.

The 2D PIV simulation has similar overall accuracy to the 3D PIV simulation, where the average of velocity magnitude has 8.5% deviation from the PIV experiment average, with a 26.6% deviation of V-velocity values, and a 2.2% deviation of U-velocity values. It has deviation from the experiment values in similar places to the 3D PIV simulation, particularly at the outlet. It differs, however, within the aneurysm zone, where the recirculation zone is similarly close to that of the PIV experiment results, but velocity on average deviates significantly more, as can be seen in location 6 on table 9. This suggests that 2D simulations provide a similarly accurate representation of flow velocity within the artery zone but not in the aneurysm zone. Since the recirculation zones are not significantly different between the 2D PIV simulation and the

PIV experiment, there may be value in performing 2D simulations in determining the rate at which thrombin scalar concentration increases for steady flow and potentially pulsatile flow; presuming that this rate is not entirely dependent upon fluid velocity alone.

It is worth noting that upon inspection of Figure 88, it appears that the center of recirculation of the steady flow model is in a similar location to that of the PIV experiment. It would be useful to repeat the PIV experiment with a flow velocity at the inlet like that used in the steady flow model, to see if the center of recirculation within the aneurysm zone shifts significantly. This would help to determine if 2D simulation recirculation zones are more representative of realistic flow across a range of flow velocities within the aneurysm zone, or only relatively low flow velocity within the aneurysm zone.

The PIV experiment and PIV simulation results are like the work produced by Mulder et al. insofar as the 3D PIV Simulation results are a reasonable representation of that produced by the PIV experiment, with an overall 8.36% deviation from the experimental results. It should be noted that the center of circulation within the aneurysm differs slightly more in location between the experimental results and PIV results in the dissertation comparison than in Mulder et al.'s research. To a degree this may be attributed to the difference between the comparison made in this dissertation and that of Mulder et al., being that Mulder et al.'s PIV method captured the flow profile of the entire flow phantom, allowing for easier comparison between the experiment and simulation output, where the PIV method employed for the dissertation captured a plane for comparison to a 3D PIV simulation output. This may also be related to the fact that the flow within the aneurysm of Mulder et al.'s research is significantly higher than that applied in the collaboration PIV experiment. This is significant since large deviation between the PIV simulations and the PIV experiment is consistently located in low velocity areas, which potentially means that more accuracy may be achieved should the PIV experiment be repeated with a higher velocity flow at the inlet.

8.4. Limitations

Limitations for the pulsatile to steady flow comparison include the simplification of Buetenas et al.'s model from an exponential based function to a sinusoid-based function, and the lack of inclusion of other idealized and realistic geometries. The sinusoid does not capture the lag time of Buetenas et al.'s model, and provides a less steep curve for thrombin generation, and in turn results in a less realistic representation of the thrombin generation process. The inclusion of multiple aneurysm geometries, including geometries derived from patients would provide a much more encompassing comparison of thrombin generation between pulsatile and steady flow. It would furthermore provide a more robust comparison of pulsatile and steady flow outcomes to have a variety of pulsatile flow functions available.

Exploration of a Windkessel boundary element, and derivations of flow and pressure from wave propagation and reflection is also worth consideration.

Limitations of the PIV experiment include the lack of a full 3D profile, the lack of variation of inlet velocity in the PIV experiment, and the lack of a pulsatile comparison. The lack of a 3D profile for the PIV experiment prevents a more thorough comparison of the 3D PIV simulation results. A variation of inlet flow velocities in the PIV experiment would allow for a better understanding of how accurate the PIV simulations are over a range of inlet velocities. In particular, an inlet velocity similar to that applied in Mulder et al.'s work would have allowed for a more robust comparison of the PIV simulation and PIV experiment results to that achieved by Mulder et al., and thereby a more robust prediction of how thrombin generation may occur in the steady conditions presented by Mulder et al. The lack of inclusion of pulsatility in the PIV experiment prevents a more robust discussion of the accuracy of the pulsatile thrombin generation outcome in this research.

Conclusion and Recommendations

The pulsatile-flow model clearly influences the rate at which conditions for clotting are met in thrombosis model; almost doubling the rate at which the conditions for clotting are met within the aneurysm geometry model, and may potentially cause the recirculation of other components for clotting that circulate through the blood. This suggests that pulsatile-flow may have a significant effect on clotting outcomes for other thrombosis models where the effects of pulsatile-flow have not been thoroughly considered and forgone in favor of steady flow.

The steady flow results are validated insofar as the velocity magnitude are overall relatively accurate, though according to the comparisons made in this study, it should be expected that the center of recirculation within the aneurysm zone of the steady flow simulation may differ slightly from actual flow. This in turn may cause a difference in the rate at which clotting occurs in a simulation vs a physical setting. It should however remain noted, that according to the conclusions made from the comparisons of the rate of increase of thrombin generation between steady and pulsatile flow, that the rate at which thrombin concentration increases appears to be more closely related to the steadiness and rate of flow into the aneurysm zone than the flow pattern itself. Since flow is incompressible, flow into and out of the aneurysm occurs at a consistent rate, which in turn means that thrombin enters and exits the aneurysm proportionally. It is uncertain whether this trend can be significantly altered by where recirculation occurs within the aneurysm. It is furthermore suggested that the PIV experiment be repeated with pulsatile-flow

conditions to properly validate the pulsatile-flow model. The steady flow model validation gives insight into how accurate the pulsatile model may be, but it is important that further validations are made for the pulsatile model with a similar method.

Overall the problem should be further explored by completing the implementation of full clotting model inclusive of biological functions into the ANSYS® Fluent pulsatile simulation, so full clotting outcomes under pulsatile flow may be explored and compared to full outcomes under steady flow.

In parallel, there is a strong need for a validation experiment that confirms the difference between thrombosis under pulsatile and steady flow conditions. It is possible that PIV experimentation can answer this call with the implementation of a fluid capable of mimicking the effects of clotting. Until this is accomplished, computational models designed with the intention to accurately simulate thrombosis in-vivo should be designed with consideration to how pulsatile flow conditions may affect clotting functions and outcomes.

References

Adrian, Ronald J., & Westerweel, Jerry. (2011). *Particle Image Velocimetry*. 32 Avenue of the Americas, New York, NY 10013-2473, USA: Cambridge University Press.

ANSYS® Fluent 19.1, Help System, Fluent Theory Guide Chapter 1: Basic Fluid Flow | 1.2. Continuity and Momentum Equations | 1.2.2. Momentum Conservation Equations, Chapter 1: Basic Fluid Flow | 1.3. User-Defined Scalar (UDS) Transport Equations | 1.3.1. Single Phase Flow, Chapter 21: Solver Theory | 21.2. General Scalar Transport Equation: Discretization and Solution, Chapter 21: Solver Theory | 21.3. Discretization | 21.3.1. Spatial Discretization, Chapter 21: Solver Theory | 21.3. Discretization | 21.3.1.3. Second-Order Upwind Scheme, Chapter 21: Solver Theory | 21.3. Discretization | 21.3.2. Temporal Discretization, Chapter 21: Solver Theory | 21.3. Discretization | 21.3.2.1. Implicit Time Integration, Chapter 21: Solver Theory | 21.3. Discretization | 21.3.3. Evaluation of Gradients and Derivatives, Chapter 21: Solver Theory | 21.3. Discretization | 21.3.3.4. Least Squares Cell-Based Gradient Evaluation, Chapter 21: Solver Theory | 21.3. Discretization | 21.3.4. Gradient Limiters, Chapter 21: Solver Theory | 21.3. Discretization | 21.3.4.1. Standard Limiter, Chapter 21: Solver Theory | 21.4. Pressure-Based Solver, Chapter 21: Solver Theory | 21.4. Pressure-Based Solver | 21.4.1. Discretization of the Momentum Equation, Chapter 21: Solver Theory | 21.4. Pressure-Based Solver | 21.4.1.1. Pressure Interpolation Schemes, Chapter 21: Solver Theory | 21.4. Pressure-Based Solver | 21.4.2. Discretization of the Continuity Equation, Chapter 21: Solver Theory | 21.4. Pressure-Based Solver | 21.4.3.1.1. SIMPLE, Chapter 21: Solver Theory | 21.4. Pressure-Based Solver | 21.4.3.1.2. SIMPLEC, Chapter 21: Solver Theory | 21.4. Pressure-Based Solver | 21.4.3.1.3. PISO, Chapter 21: Solver Theory | 21.4. Pressure-Based Solver | 21.4.3.1.3.1. Neighbor Correction, Chapter 21: Solver Theory | 21.4. Pressure-Based Solver | 21.4.3.1.3.2. Skewness Correction, Chapter 21: Solver Theory | 21.4. Pressure-Based Solver | 21.4.3.1.3.3. Skewness - Neighbor Coupling, Chapter 21: Solver Theory | 21.4. Pressure-Based Solver | 21.4.4.1. Under-Relaxation of Variables, Chapter 21: Solver Theory | 21.4. Pressure-Based Solver | 21.4.4.2. Under-Relaxation of Equations, Chapter 21: Solver Theory | 21.4. Pressure-Based Solver | 21.4.5. Time-Advancement Algorithm, Chapter 21: Solver Theory | 21.4. Pressure-Based Solver | 21.4.5.1. Iterative Time-Advancement Scheme, Chapter 21: Solver Theory | 21.7. Multigrid Method | 21.7.1.1. The Need for Multigrid, Chapter 21: Solver Theory | 21.7. Multigrid Method | 21.7.1.2. The Basic Concept in Multigrid, Fluent Theory Guide Chapter 21: Solver Theory | 21.7. Multigrid Method | 21.7.1.3. Restriction and Prolongation, Chapter 21: Solver Theory | 21.7. Multigrid Method | 21.7.2.1. The V and W cycles, Chapter 21: Solver Theory | 21.7. Multigrid Method | 21.7.3.1. AMG Restriction and Prolongation Operators, Chapter 21: Solver Theory | 21.7. Multigrid Method | 21.7.3.2. AMG Coarse Level Operator. ANSYS®, Inc.

Augsburger, Luca., Farhat, Mohamed., Reymond, Philippe., Fonck, Edouard., Kulcsar, Zsolt., Stergiopulos, Nikos., & Rüfenacht, Daniel A. (2009). Effect of Flow Diverter Porosity on Intraaneurysmal Blood Flow | SpringerLink. *Clinical Neuroradiology, 19*(3), 204-214. doi:10.1007/s00062-009-9005-0

Bavinzski, Gerhard, Talazoglu, Volkan, Killer, Monika, Richling, Bernd, Gruber, Adreas, Gross, Cordell E., & Plenk Jr., Hanns. (2009). Gross and microscopic histopathological findings in aneurysms of the human brain treated with Guglielmi detachable coils. *Journal of Neurosurgery, 91*(2), 284-293.

doi:10.3171/jns.1999.91.2.0284

Becske, Tibor, Kallmes, David F., Saatci, Isil, McDougall, Cameron G., Szikora, István, Lanzino, Giuseppe, . . . Nelson, Peter K. (2013). Pipeline for Uncoilable or Failed Aneurysms: Results from a Multicenter Clinical Trial. *Neuroradiology, 267*(3). doi:10.1148/radiol.13120099

Bouzeghrane, F., Naggara, O., Kallmes, D.F., Berenstein, A., Raymond, J., & Centres, The International Consortium of Neuroendovascular. (2010). In Vivo Experimental Intracranial Aneurysm Models: A Systematic Review. *American Journal of Neuroradiology, 31*(3), 418-423. doi:10.3174/ajnr.A1853

Brinjikji, Waleed, Murad, Mohammad H., Lanzino, Giuseppe, Cloft, Harry J., & Kallmes, David F. (2013). Endovascular Treatment of Intracranial Aneurysms With Flow Diverters. *Stroke, 44*(2), 442-447. doi:10.1161/STROKEAHA.112.678151

Brinkman, Herm-Jan M., Mertens, Koen., Holthius, Joost., Zwart-Huinink, Lineke A., Grijm, Karin., & Van Mourik, Jan A. (1994). The activation of human blood coagulation factor X on the surface of endothelial cells: a comparison with various vascular cells, platelets and monocytes - Brinkman - 1994 - British Journal of Haematology. *British Journal of Haematology*. doi:10.1111/j.1365-2141.1994.tb04918.x

Brisman, Jonathan L., Song, Joon K., & Newell, David W. (2006). Cerebral Aneurysms. *The New England Journal of Medicine, 355*(1), 928-939. doi:NJ200608313550911

Bugge, T H, Xiao, Q, Kombrinck, K W, Flick, M J, Holmbäck, K, Danton, M j, . . . Degen, J L. (1996). Fatal embryonic bleeding events in mice lacking tissue factor, the cell-associated initiator of blood coagulation. *PNAS, 93*(13), 6258-6263. doi:10.1073/pnas.93.13.6258

Butenas, Saulius, Bouchard, Beth A., Brummel-Ziedins, Kathleen E., Parhami-Seren, Behnaz, & G., Mann Kenneth. (2005). Tissue factor activity in whole blood. *Blood, 105*(7), 2764-2770. doi:10.1182/blood-2004-09-3567

Butenas, Saulius, Orfeo, Thomas, & Mann, Kenneth G. (2009). Tissue Factor in Coagulation. *Arteriosclerosis, Thrombosis, and Vascular Biology, 29*(12), 1989-1996. doi:10.1161/ATVBAHA.108.177402

Butenas, Saulius, van't Veer, Cornelis, & Mann, Kenneth G. (1999). "Normal" Thrombin Generation. *Blood, 94*(7), 2169-2178.

Butty, V.D., Gudjonsson, K., Buchel, P., Makhijani, V.B., Ventikos, Y., & Poulikakos, D. (2002). Residence times and basins of attraction for a realistic right internal carotid artery with two aneurysms. *Biorheology, 39*(3-4), 387-393.

Byrne, J V, Hope, J K, Hubbard, N, & Morris, J H. (1997). The nature of thrombosis induced by platinum and tungsten coils in saccular aneurysms. *American Journal of Neuroradiology, 18*(1), 29-33.

Byrne, James V., Beltechi, Radu., Yarnold, Julia A., Birks, Jacqueline., & Kamran, Mudassar. (2010). Early Experience in the Treatment of Intra-Cranial Aneurysms by Endovascular Flow Diversion: A Multicentre Prospective Study. doi:10.1371/journal.pone.0012492

Calviere, L., Viguier, A., Da Silva, N. A., Cognard, C., & Larrue, V. (2011). Unruptured intracranial aneurysm as a cause of cerebral ischemia. *Clinical Neurology and Neurosurgery, 113*(1), 28-33. doi:https://doi.org/10.1016/j.clineuro.2010.08.016

Carmeliet, Peter, Mackman, Nigel, Moons, Lieve, Luther, Thomas, Gressens, Pierre, Van Vlaenderen, Lise, . . . Collen, Désiré. (1996). Role of tissue factor in embryonic blood vessel development. *Nature, 383*(6595), 73. doi:doi:10.1038/383073a0

Clauser, Johanna., Knieps, Marius S., Büsen, Martin., Ding, Andreas., Schmitz-Rode, Thomas., Steinseifer, Ulrich, . . . Cattaneo, Giorgo. (2018). A Novel Plasma-Based Fluid for Particle Image Velocimetry (PIV): In-Vitro Feasibility Study of Flow Diverter Effects in Aneurysm Model | SpringerLink. *Annals of Biomedical Engineering, 46*(6), 841-848. doi:10.1007/s10439-018-2002-1

Cohen, José E., Yitshayek, Eyal, Gomori, John Moshe Grigoriadis, Savvas, Raphaeli, Guy, Spektor, Sergei, & Rajz, Gustavo. (2007). Spontaneous thrombosis of cerebral aneurysms presenting with ischemic stroke. *Journal of the Neurological Sciences, 254*(1), 95-98. doi:10.1016/j.jns.2006.12.008

Davie, Earl W., & Ratnoff, Oscar D. (1964). Waterfall Sequence for Intrinsic Blood Clotting. *Science, 145*(3638), 1310-1312. doi:10.1126/science.145.3638.1310

de Sousa, Daniel Ribeiro, Vallecilla, Carolina, Chodzynski, Kamil, Jerez, Ricardo Corredor, Malaspinas, Orestis, Eker, Omer Faruk, . . . Boudjeltia, Karim Zouaoui. (2016). Determination of a shear rate threshold for thrombus formation in intracranial aneurysms. *Journal Neurointerventional Surgery, 8*(8). doi:10.1136/neurintsurg-2015-011737

Di Achille, P., Tellides, G., Figueroa, C. A., & Humphrey, J. D. (2014). A haemodynamic predictor of intraluminal thrombus formation in abdominal aortic aneurysms. *470*(2172). doi:10.1098/rspa.2014.0163

Einav, Shmuel, & Bluestein, Danny. (2006). Dynamics of Blood Flow and Platelet Transport in Pathological Vessels. *Annals of The New York Academy of Sciences, 1015*(1), 351-366. doi:10.1196/annals.1302.031

Eller, Theodore W. (1986). MRI demonstration of clot in a small unruptured aneurysm causing stroke. *Journal of Neurosurgery, 65*(3), 411-412. doi:10.3171/jns.1986.65.3.0411

Falati, Shahrokh, Gross, Peter, Merrill-Skoloff, Glenn, Furie, Barbara C., & Furie, Bruce. (2002). Real-time *in vivo* imaging of platelets, tissue factor and fibrin during arterial thrombus formation and in the mouse. *Nature Medicine, 8*(10), 1175-1180. doi:doi:10.1038/nm782

Ferns, S.P., Schneiders, J.J., Siebes, M., van den Berg, R., van Bavel, E.T., & Majoie, C.B. (2010). Intracranial Blood-Flow Velocity and Pressure Measurements Using an Intra-Arterial Dual-Sensor Guidewire. *American Journal of Neuroradiology, 31*(2), 324-326. doi:10.3174/ajnr.A1718

Furie, Bruce, & Furie, Barbara C. (1992). Molecular and Cellular Biology of Blood Coagulation. *The New England Journal of Medicine*. doi:NJ199203193261205

Furie, Bruce, & Furie, Barbara C. (2005). Thrombus formation in vivo. *The Journal of Clinical Investigation, 115*(12), 3355-3362. doi:10.1172/JCI26987

Furie, Bruce, & Furie, Barbara C. (2009). Mechanisms of Thrombus Formation. *The New England Journal of Medicine*. doi:NJ200808283590909

GHO | Prevalence of obesity among adults, BMI ≥ 30, crude. (2016). World Health Organization.

GHO | Mortality and global health estimates. (2016). World Health Organization.

GHO | Raised blood pressure (SBP ≥ 140 OR DBP ≥ 90), age-standardized (%). (2015). World Health Organization.

GHO | World Health Statistics data visualizations dashboard | Harmful use of alcohol. (2016). World Health Organization.

GHO | World Health Statistics data visualizations dashboard | Tobacco smoking. (2016). World Health Organization.

Giesen, Peter L. A., Rauch, Ursula, Bohrmann, Bernd, Kling, Dorothee, Roqué, Merce, Fallon, John T., . . . Nemerson, Yale. (1999). Blood-borne tissue factor: Another view of thrombosis. *PNAS, 96*(5), 2311-2315. doi:10.1073/pnas.96.5.2311

Goldsmith, Harry L., & Karino, Takeshi. (1987). Interactions of Human Blood Cells with the Vascular Endothelium. *Blood in Contact with Natural and Artificial Surfaces, 516*(1). doi:10.1111/j.1749-6632.1987.tb33067.x

Hathcock, James J., & Nemerson, Yale. (2004). Platelet deposition inhibits tissue factor activity: in vitro clots are impermeable to factor Xa. *Blood, 104*(1), 123-127. doi:10.1182/blood-2003-12-4352

Hemker, H.C., Giesen, P., Al Dieri, R., Regnault, V., de Smed, E., Wagenvoord, R., . . . Béguin, S. (2018). The Calibrated Automated Thrombogram (CAT): a universal routine test for hyper- and hypocoagulability. *Pathophysiology of Haemostasis and Thrombosis, 32*(5-6), 249-253. doi:10.1159/000073575

Hockin, Matthew F., Jones, Kenneth C., Everse, Stephen J., & Mann, Kenneth G. (2002). A Model for the Stoichiometric Regulation of Blood Coagulation. *Journal of Biological Chemistry, 277*(1), 18322-18333. doi:10.1074/jbc.M201173200

Hoffman, M., Whinna, H. C., & Monroe, D. M. (2006). Circulating tissue factor accumulates in thrombi, but not in hemostatic plugs. *journal of thrombosis and hemostasis, 4*(9), 2092-2093. doi:10.1111/j.1538-7836.2006.02085.x

Hoffman, Maureane. (2003). A cell-based model of coagulation and the role of factor VIIa. *Blood Reviews, 17*(1), 1-5. doi:10.1016/S0268-960X(03)90000-2

Hoffman, Maureane. (2003). Remodeling the Blood Coagulation Cascade. *Journal of Thrombosis and*

Thrombolysis, 16(1-2), 17-20. doi:10.1023/B:THRO.0000014588.95061.28

Humphrey, J.D., & Canham, P.B. (2000). Structure, Mechanical Properties, and Mechanics of Intracranial Saccular Aneurysms. *Journal of elasticity and the physical science of solids, 61*(1-3), 49-81. doi:10.1023/A:1010989418250

Ishikawa, Tatsuya, Nakayama, Naoki, Yoshimoto, Tetuyuki, Aoki, Takeshi, Terasaka, Shynsuke, Nomura, Mikio, . . . Iwasaki, Yoshinobu. (2006). How does spontaneous hemostasis occur in ruptured cerebral aneurysms? Preliminary investigation on 247 clipping surgeries. *World Neurosurgery, 66*(3), 269-275. doi:10.1016/j.surneu.2006.03.030

Jones, K C, & Mann, K G. (1994). A model for the tissue factor pathway to thrombin. II. A mathematical simulation. *The Journal of Biological Chemistry, 269*(1), 23367-23373.

Kallmes, D.F., Hanel, R., Lopes, D., Boccardi, E., Bonafé, A., Cekirge, S., . . . Lylyk, P. (2015). International Retrospective Study of the Pipeline Embolization Device: A Multicenter Aneurysm Treatment Study. *American Journal of Neuroradiology, 36*(1), 108-115. doi:10.3174/ajnr.A4111

Krisht, Ali F., Gomez, Jorge, Partington, Sharon (2018). Outcome of Surgical Clipping of Unruptured Aneurysms as it Compares with a 10-Year Nonclipping Survival Period. *Neurosurgery, 58*(2), 207-216. doi:10.1227/01.NEU.0000194638.61073.FC

Kuwahara, Mitsuhiro, Sugimoto, Mitsuhiko, Tsuji, Shizuko, Matsui, Hideto, Mizuno, Tomohiro, Miyata, Shigeki, & Yoshioka, Akira. (2002). Platelet Shape Changes and Adhesion Under High Shear Flow. *Arteriosclerosis, Thrombosis, and Vascular Biology, 22*(2), 329-344.

Lanterna, Luigi A., Ospedali Riuniti, Bergamo, Tredici, Giovanni, Dimitrov, Borislav D., Ospedali, Riuniti (2018). Treatment of Unruptured Cerebral Aneurysms by Embolization with Guglielmi Detachable Coils: Case-fatality, Morbidity, and Effectiveness in Preventing Bleeding—A Systematic Review of the Literature. *Neurosurgery, 55*(4), 767-778. doi:10.1227/01.NEU.0000137653.93173.1C

Lawton, Michael T., Quiñones-Hinojosa, Alfredo, Chang, Edward F. (2018). Thrombotic Intracranial Aneurysms: Classification Scheme and Management Strategies in 68 Patients. *Neurosurgery, 56*(3), 441-454. doi:10.1227/01.NEU.0000153927.70897.A2

Li, Melissa, Ku, David N., & Forest, Craig R. (2012). Microfluidic system for simultaneous optical measurement of platelet aggregation at multiple shear rates in whole blood. *Lab Chip, 12*(1), 1355-1362. doi:10.1039/C2LC21145A

MacFarlane, R. G. (1964). An Enzyme Cascade in the Blood Clotting Mechanism, and its Function as a Biochemical Amplifier. *Nature, 202*(4931), 498. doi:10.1038/202498a0

Mann, K. G. (2005). Adding the vessel wall to Virchow's triad. *journal of thrombosis and haemostasis*. doi:10.1111/j.1538-7836.2005.01738.x

Morel, Olivier, Jesel, Laurence, Freyssinet, Jean-Marie, & Toti, Florence. (2010). Cellular Mechanisms Underlying the Formation of Circulating Microparticles. *Arteriosclerosis, Thrombosis, and Vascular Biology, 31*(1), 15-26. doi:10.1161/ATVBAHA.109.200956

Morel, Olivier, Toti, Florence, Hugel, Bénédicte, Bakouboula, Babé, Camoin-Jau, Laurence, Dignat-George, Françoise, & Freyssinet, Jean-Marie. (2006). Procoagulant Microparticles. *Arteriosclerosis, Thrombosis, and Vascular Biology, 26*(12), 2594-2604. doi:10.1161/01.ATV.0000246775.14471.26

Morita, Akio, Fujiwara, Satoru, Hashi, Kazuo, Ohtsu, Hiroshi, & Kirino, Takaaki. (2009). Risk of rupture associated with intact cerebral aneurysms in the Japanese population: a systematic review of the literature from Japan. *Journal of Neurosurgery, 102*(4), 601-606. doi:10.3171/jns.2005.102.4.0601

Mortality and causes of death in South Africa, 2015: Findings from death notification. (2015). Statistics South Africa Retrieved from http://www.statssa.gov.za/publications/P03093/P030932015.pdf.

Mulder, G. B., Arjen C. B. Rongen, Peter. van de Vosse, Frans N. (2009) On automated analysis of flow patterns in cerebral aneurysmsbased on vortex identification. *J Eng Math*, 391–401.

Naggara, Olivier N., White, Phil M., Guilbert, François, Roy, Daniel, Weill, Alain, & Raymond, Jean. (2010). Endovascular Treatment of Intracranial Unruptured Aneurysms: Systematic Review and Meta-Analysis of the Literature on Safety and Efficacy. *Radiology, 256*(3). doi:10.1148/radiol.10091982

Ngoepe, M. N., & Ventikos, Y. (2015). Computational modelling of clot development in patient-specific cerebral aneurysm cases - Ngoepe - 2016 - Journal of Thrombosis and Haemostasis - Wiley Online Library. *journal of thrombosis and haemostasis, 14*(2), 262-272. doi:10.1111/jth.13220

Ngoepe, Malebogo N., Frangi, Alejandro F., Byrne, James V., & Ventikos, Yiannis. (2018). Thrombosis in Cerebral Aneurysms and the Computational Modeling Thereof: A Review. *Frontiers in Physiology, 9*(306). doi:doi:10.3389/fphys.2018.00306

Okorie, Uzoma M., Denney, William S., Chatterjee, Manash S., Neeves, Keith B., & Diamond, Scott L. (2008). Determination of surface tissue factor thresholds that trigger coagulation at venous and arterial shear rates: amplification of 100 fM circulating tissue factor requires flow. *Blood, 11*(7), 3507-3513. doi:10.1182/blood-2007-08-106229

Orfeo, Thomas, Butenas, Saulius, Brummel-Ziedins, Kathleen E., & Mann, Kenneth G. (2005). The Tissue Factor Requirement in Blood Coagulation. *The Journal of Biological Chemistry, 280*, 42887-42896. doi:10.1074/jbc.M505506200

Ouared, R., Chopard, B., Stahl, B., Rüfenacht, D. A., Yilmaz, H., & Courbebaisse, G. (2008). Thrombosis modeling in intracranial aneurysms: a lattice Boltzmann numerical algorithm. *Computer Physics Communications, 179*(1), 128-131. doi:https://doi.org/10.1016/j.cpc.2008.01.021

Peach, Thomas, Cornhill, J. Fredrick, Nguyen, Anh, Riina, Howard, & Ventikos, Yiannis. (2014). The 'Sphere': A Dedicated Bifurcation Aneurysm Flow-Diverter Device. *Cardiovascular Engineering and Technology, 5*(4), 334-347. doi:10.1007/s13239-014-0188-4

Piano, Mariangela, Valvassori, Luca, Quilici, Luca, Pero, Guglielmo, & Boccardi, Edoardo. (2013). Midterm and long-term follow-up of cerebral aneurysms treated with flow diverter devices: a single-center experience. *Journal of Neurosurgery, 118*(2), 408-416. doi:2012.10.JNS112222

Raghavan, Madhavan L., Ma, Baoshun, & Harbaugh, Robert E. (2009). Quantified aneurysm shape and rupture risk. *Journal of Neurosurgery, 102*(2), 355-362. doi:10.3171/jns.2005.102.2.0355

Rana, K. & Neeves, K. B. (2016) Blood flow and mass transfer regulation of coagulation. *Blood Reviews*, 30(5), 357-368.

Rayz, V. L., Boussel, L., Ge, L., Leach, J. R., Martin, A. J., Lawton, M. T., . . . Saloner, D. (2010). Flow Residence Time and Regions of Intraluminal Thrombus Deposition in Intracranial Aneurysms | SpringerLink. *Annals of Biomedical Engineering, 38*(10), 3058-3069. doi:10.1007/s10439-010-0065-8

Rosing, J, van Rijn, JL, Bevers, EM, van Dieijen, G, Comfurius, P, & Zwaal, RF. (1985). The role of activated human platelets in prothrombin and factor X activation. *blood, 65*(2), 319-332.

Sadasivan, Chander, Lieber, Baruch B., Gounis, Matthew J., Lopes, Demetrius K., & Hopkins, L. N. (2002). Angiographic Quantification of Contrast Medium Washout from Cerebral Aneurysms after Stent Placement. *American Journal of Neuroradiology, 23*(7), 1214-1221.

Sakariassen, K. S., Bolhuis, P. A., & Sixma, J. J. (1979). Human blood platelet adhesion to artery subendothelium is mediated by factor VIII–Von Willebrand factor bound to the subendothelium. *Nature, 279*(5714), 636. doi:doi:10.1038/279636a0

Scanarini, M., Mingrino, S., Giordano, R., & Baroni, A. (1978). Histological and ultrastructural study of intracranial saccular aneurysmal wall | SpringerLink. *Acta Neurochirurgica, 43*(3-4), 171-182. doi:10.1007/BF01587953

Sorensen, Erik N., Burgreen, Greg W., Wagner, William R., & Antaki, James F. (1999). Computational Simulation of Platelet Deposition and Activation: I. Model Development and Properties | SpringerLink. *Annals of Biomedical Engineering, 27*(4), 436-448. doi:10.1114/1.200

Stel, HV, Sakariassen, KS, de Groot, PG, van Mourik, JA, & Sixma, JJ. (1985). Von Willebrand factor in the vessel wall mediates platelet adherence. *Blood, 1985*(65), 85-90.

Sutherland, Garnette R., King, Martin E., Peerless, S. J., Vezina, William C., Brown, G. William, & Chamberlain, Mike J. (2009). Platelet interaction within giant intracranial aneurysms. *Journal of Neurosurgery, 56*(1), 53-61. doi:10.3171/jns.1982.56.1.0053

Toomey, JR, Kratzer, KE, Lasky, NM, Stanton, JJ, & Broze, GJ Jr. (1996). Targeted disruption of the murine tissue factor gene results in embryonic lethality. *Blood, 88*(1), 1583-1587.

Vanninen, Ritva, Manninen, Hannu, & Ronkainen, Antti. (2003). Broad-Based Intracranial Aneurysms: Thrombosis Induced by Stent Placement. *American Journal of Neuroradiology, 24*(2), 263-266.

Wagenvoord, R., Hemker, P. W., & Hemker, H.C. (2006). The limits of simulation of the clotting system. *journal of thrombosis and haemostasis, 4*(6), 1331-1338. doi:10.1111/j.1538-7836.2006.01967.x

Wardlaw, J. M., & White, P. M. (2018). The detection and management of unruptured intracranial aneurysms. *Brain, 123*(2), 205-221. doi:10.1093/brain/123.2.205

Wermer, Marieke J.H., van der Schaaf, Irene C., Algra, Ale, & J.E. Rinkel, Gabriël. (2007). Risk of Rupture of Unruptured Intracranial Aneurysms in Relation to Patient and Aneurysm Characteristics. *Stroke, 38*(4), 1404-1410. doi:10.1161/01.STR.0000260955.51401.cd

Whittle, I R, Dorsch, N W, & Besser, M. (1982). Spontaneous thrombosis in giant intracranial aneurysms. *Neurology, Neurosurgery & Psychiatry, 45*(11). doi:10.1136/jnnp.45.11.1040

Wiebers, David O. (2003). Unruptured intracranial aneurysms: natural history, clinical outcome, and risks of surgical and endovascular treatment. *The Lancet, 362*(9378), 103-110. doi:https://doi.org/10.1016/S0140-6736(03)13860-3

Wiebers, David O. (2009). The risk of rupture of unruptured cerebral aneurysms in the Japanese population: a systematic review of the literature from Japan by Morita, et al. *Journal of Neurosurgery, 102*(4), 597-598. doi:10.3171/jns.2005.102.4.0597

Womersley, J. R. (1955). Method for the calculation of velocity, rate of flow and viscous drag in arteries when the pressure gradient is known. *J Physiol, 127*(3), 553-563.

You, S-H, Kong, D-S, Kim, J-S, Jeon, P, Kim, K H, Roh, H K, . . . Hong, S-C. (2010). Characteristic features of unruptured intracranial aneurysms: predictive risk factors for aneurysm rupture. *Neurology, Neurosurgery, & Psychiatry, 81*(5), 479-484. doi:10.1136/jnnp.2008.169573

Appendix

1. Womersley Flow

Pulsatile velocity in the space domain:

$$U(y) = -P_z' \frac{1}{j\rho\omega}[1 - \frac{J_0(j^{3/2}\alpha y)}{J_0(j^{3/2}\alpha)} \quad (1)$$

Where:

$-P_z'$	pressure gradient function $\left(\frac{pa}{m}\right)$
j	imaginary number $(dimensionless)$
ρ	fluid density $\left(\frac{kg}{m^3}\right)$
ω	angular frequency - 1st harmonic of a Fourier series of pressure gradient (rad)
$J_0(x)$	Bessel Function of the first kind and order zero $(dimensionless)$
$\alpha = r_0\sqrt{\frac{\rho\omega}{\mu}}$	Womersley number $(dimensionless)$
r_0	cylindrical radius (m)
μ	dynamic viscosity $(Pa * s)$
r	radial distance from centerline of longitudinal axis (m)

Pulsatile velocity in the time domain:

$$u(y,t) = |U(y)|\cos[\omega t + \angle(U(y)) \quad (2)$$

The Bessel functions of first kind and zero-order are the most complex part of Womersley flow and are represented by an unsolvable integral. For this reason, they had to be converted to the time-domain using series-approximation.

Bessel function J_0:

$$J_0(x) = \sum_{n=0}^{\infty} \frac{(-1)^n (x)^{2n}}{(2)^{2n}(n!)^2} \quad (3)$$

$$J_0(x) = 1 - \frac{x^2}{4} + \frac{x^4}{64} - \frac{x^6}{2304} + \frac{x^8}{147456} - \frac{x^{10}}{14745600} \cdots \frac{(-1)^n (x)^{2n}}{(2)^{2n}(n!)^2}$$

For $x = j^{3/2}\alpha$:

$$J_0\left(j^{3/2}\alpha\right) = 1 - \frac{j^3\alpha^2}{4} + \frac{j^6\alpha^4}{64} - \frac{j^9\alpha^6}{2304} + \frac{j^{12}\alpha^8}{147456} - \frac{j^{15}\alpha^{10}}{14745600} \ldots \frac{(-1)^n(j^{3/2}\alpha)^{2n}}{(2)^{2n}(n!)^2}$$

Where, $x^2 = -j\alpha^2,\ x^4 = -\alpha^4,\ x^6 = j\alpha^6,\ x^8 = \alpha^8, x^{10} = -j \propto^{10}$

$$J_0\left(j^{3/2}\alpha\right) \cong 1 + \frac{j\alpha^2}{4} - \frac{\alpha^4}{64} - \frac{j\alpha^6}{2304} + \frac{\alpha^8}{147456} + \frac{j\alpha^{10}}{14745600}$$
$$= \left(1 - \frac{\alpha^4}{64} + \frac{\alpha^8}{147456}\right) + j\left(\frac{\alpha^2}{4} - \frac{\alpha^6}{2304} + \frac{\alpha^{10}}{14745600}\right)$$

$$J_0\left(j^{3/2}\alpha\right) = a_{j^{3/2}\alpha} + jb_{j^{3/2}\alpha} \tag{4}$$

For $x = j^{3/2}\alpha y$ where $y = \frac{r}{r_0}$:

$$J_0\left(j^{3/2}\alpha y\right) = 1 - \frac{j^3\alpha^2y^2}{4} + \frac{j^6\alpha^4y^4}{64} - \frac{j^9\alpha^6y^6}{2304} + \frac{j^{12}\alpha^8y^8}{147456} - \frac{j^{15}\alpha^{10}y^{10}}{14745600} \ldots \frac{(-1)^n(j^{3/2}\alpha y)^{2n}}{(2)^{2n}(n!)^2}$$

$x^2 = -j\alpha^2y^2 \quad x^4 = -\alpha^4y^4 \quad x^6 = j\alpha^6y^6 \quad x^8 = \alpha^8y^8 \quad x^{10} = -j \propto^{10} y^{10}$

$$J_0\left(j^{3/2}\alpha y\right) \cong 1 + \frac{j\alpha^2y^2}{4} - \frac{\alpha^4y^4}{64} - \frac{j\alpha^6y^6}{2304} + \frac{\alpha^8y^8}{147456} + \frac{j\alpha^{10}y^{10}}{14745600}$$
$$= \left(1 - \frac{\alpha^4y^4}{64} + \frac{\alpha^8y^8}{147456}\right) + j\left(\frac{\alpha^2y^2}{4} - \frac{\alpha^6y^6}{2304} + \frac{\alpha^{10}y^{10}}{14745600}\right)$$

$$J_0\left(j^{3/2}\alpha y\right) = a_{j^{3/2}\alpha y} + jb_{j^{3/2}\alpha y} \tag{5}$$

So:

$$\frac{J_0(j^{3/2}\alpha y)}{J_0(j^{3/2}\alpha)} = \frac{a_{j^{3/2}\alpha y} + jb_{j^{3/2}\alpha y}}{a_{j^{3/2}\alpha} + jb_{j^{3/2}\alpha}}$$
$$= \frac{(a_{j^{3/2}\alpha y} + jb_{j^{3/2}\alpha y}) * (a_{j^{3/2}\alpha} - jb_{j^{3/2}\alpha})}{(a_{j^{3/2}\alpha} + jb_{j^{3/2}\alpha}) * (a_{j^{3/2}\alpha} - jb_{j^{3/2}\alpha})}$$

$$= \frac{a_{j^{3/2}\alpha y}a_{j^{3/2}\alpha} + b_{j^{3/2}\alpha y}b_{j^{3/2}\alpha}}{{a_{j^{3/2}\alpha}}^2 + {b_{j^{3/2}\alpha}}^2} + j\frac{a_{j^{3/2}\alpha}b_{j^{3/2}\alpha y} - a_{j^{3/2}\alpha y}b_{j^{3/2}\alpha}}{{a_{j^{3/2}\alpha}}^2 + {b_{j^{3/2}\alpha}}^2}$$

$$\frac{J_0(j^{3/2}\alpha y)}{J_0(j^{3/2}\alpha)} = a_{bess} + jb_{bess} \tag{6}$$

The pressure gradient function must be constructed from input data in the time domain and had to be converted into the space domain before the Womersley flow function could be further simplified into rectangular form.

Pressure gradient rectangular form:

$$-P'_z = |-P'_z|\cos(\emptyset) + j|-P'_z|\sin(\emptyset) \tag{7}$$

Where, $\emptyset$ is the phase difference between pressure waveforms

$$-P'_z = a_{press.grad.} + jb_{press.grad.} \tag{8}$$

Afterwards the parts were combined and converted into rectangular form, and finally into the time domain.

Pulsatile velocity in the space domain:

$$U(y) = -P'_z\frac{1}{j\rho\omega}[1 - \frac{J_0(j^{3/2}\alpha y)}{J_0(j^{3/2}\alpha)}] \tag{9}$$

$$= (a_{press.grad.} + jb_{press.grad.})\frac{1}{j\rho\omega}[1 - (a_{bess} + jb_{bess})]$$

$$= \frac{(a_{press.grad.} + jb_{press.grad.}) * ((1 - a_{bess}) - jb_{bess})}{j\rho\omega}$$

$$= \left(\frac{(a_{press.grad.}(1 - a_{bess}) + b_{press.grad.}b_{bess}) + j((1 - a_{bess})b_{press.grad.} - a_{press.grad.}b_{bess})}{j\rho\omega}\right) * \frac{j}{j}$$

$$U(y) = \frac{\left((1 - a_{bess})b_{press.grad.} - a_{press.grad.}b_{bess}\right)}{\rho\omega} - j\frac{\left(a_{press.grad.}(1 - a_{bess}) + b_{press.grad.}b_{bess}\right)}{\rho\omega}$$

$$U(y) = (Re) + j(Im) \tag{10}$$

Pulsatile velocity in the time domain:

$$u(y,t) = |U(y)|\cos[\omega t + \angle(U(y))]$$

$$\boldsymbol{u(y,t) = \sqrt{Re^2 + Im^2}\, cos\left(\omega t + \tan^{-1}\frac{Im}{Re}\right)} \tag{11}$$

2. Spatial Discretization

ANSYS® Fluent works based-on cell-centered numeric's, where discrete scalar values are stored at the cell centers. These cell values are then interpolated to yield face values for convection terms by means of an upwind scheme, where a cell-face value is derived from values in the cell upstream from it relative to the direction of normal velocity (ANSYS® Academic Research Fluent 19.1, Help System, Fluent Theory Guide Chapter 21: Solver Theory | 21.3. Discretization | 21.3.1. Spatial Discretization).

Because a strong level of accuracy is desired in the simulation, the second-order upwind scheme has been applied. This computes cell-face values through a multidimensional reconstruction approach, which achieves greater accuracy by means of a Taylor series expansion of the cell-centered solution about the cell centroid.

In the second-order upwind scheme, cell face ϕ_f is computed as follows:

$$\phi_f = \phi + \nabla\phi \cdot \vec{r}$$

Where:

ϕ	Cell-centered value
$\nabla\phi$	Cell-centered value gradient in upstream cell
$\vec{r}$	displacement vector from upstream cell to the face centroid

(ANSYS® Academic Research Fluent 19.1, Help System, Fluent Theory Guide Chapter 21: Solver Theory | 21.3. Discretization | 21.3.1.3. Second-Order Upwind Scheme)

3. Temporal Discretization

Because the problem being explored is transient, the governing equations of the simulation must be discretized in both space and time.

The expression for the change of the variable ϕ over time is as follows:

$$\frac{\partial \phi}{\partial t} = F(\phi)$$

Where:

F A function that incorporates spatial discretization.

ϕ A scalar quantity

The integration of every term in this differential equation over a time-step yields the following first-order temporal discretization (ANSYS® Academic Research Fluent 19.1, Help System, Fluent Theory Guide Chapter 21: Solver Theory | 21.3. Discretization | 21.3.2. Temporal Discretization):

$$\frac{\phi^{n+1} - \phi^n}{\Delta t} = F(\phi)$$

Where:

$n+1$ Value at the next time level, $t + \Delta t$

n Value at the current time level

Implicit time integration scheme is applied to evaluate $F(\phi)$ at the future time level, and was selected due to it being unconditionally stable with respect to the size of a time-step.

The implicit equation is represented as follows:

$$\frac{\phi^{n+1} - \phi^n}{\Delta t} = F(\phi^{n+1})$$

This equation can be iteratively solved for every time level before advancing to the next time-step (ANSYS® Fluent 19.1, Help System, Fluent Theory Guide Chapter 21: Solver Theory | 21.3. Discretization | 21.3.2.1. Implicit Time Integration).

4. General Transport Equation Discretization

Discretization of the general scalar transport equation yields the following:

$$\frac{\partial \rho \phi}{\partial t} V + \sum_{f}^{N_{faces}} \rho_f \vec{v}_f \phi_f \cdot \vec{A}_f = \sum_{f}^{N_{faces}} \Gamma_\phi \nabla_{\phi_f} \cdot \vec{A}_f + S_\phi V$$

Where:

N_{faces} number of faces enclosing cell

ϕ_f value of ϕ convected through face f

$\rho_f \vec{v}_f \cdot \vec{A}_f$ mass flux through the face

$\vec{A}_f$ area of face f

∇_{ϕ_f} gradient of ϕ at face f

V cell volume

$\frac{\partial \rho \phi}{\partial t}$ The expression for the change of the variable ϕ over time

5. Momentum Equation Discretization

The discretization scheme applied for the scalar transport system is also used to discretize momentum in the x, y and z directions where ϕ is equal to u, v, and w respectively (ANSYS® Fluent 19.1, Help System, Fluent Theory Guide Chapter 21: Solver Theory | 21.4. Pressure-Based Solver | 21.4.1. Discretization of the Momentum Equation).

The discretized momentum equation is as follows:

$$a_p u = \sum_{nb} a_{nb} u_{nb} + \sum p_f A \cdot \hat{\imath} + S$$

Where:

p_f pressure face value

6. Continuity Equation Discretization

The steady-state integral-form of the continuity equation for the pressure-based solver is as follows

$$\oint \rho \vec{v} \cdot d\vec{A} = 0$$

The continuity equation yields the following discrete equation when integrated over a control volume (ANSYS® Academic Research Fluent 19.1, Help System, Fluent Theory Guide: Chapter 21: Solver Theory | 21.4. Pressure-Based Solver | 21.4.2. Discretization of the Continuity Equation).

$$\sum_{f}^{N_{faces}} J_f A_f = 0$$

Where J_f is the mass flux through face f, ρv_n

The velocity face values are averaged via momentum-weighting, where weight factors are based upon the a_p coefficient from the discretized momentum equation.

The equation for face mass flux J_f is as follows:

$$J_f = \rho_f \frac{a_{p,c_0} v_{n,c_0} + a_{p,c_1} v_{n,c_1}}{a_{p,c_0} + a_{p,c_1}} + d_f \left(\left(p_{c_0} + (\nabla p)_{c_0} \cdot \vec{r}_0 \right) - \left(p_{c_1} + (\nabla p)_{c_1} \cdot \vec{r}_1 \right) \right) = \hat{J}_f + d_f \left(p_{c_0} - p_{c_1} \right)$$

Where:

p_{c_0}, p_{c_1}	pressures in cells on either side of a face
v_{n,c_0}, v_{n,c_1}	velocities in cells on either side of a face
d_f	A function of $\bar{a}_P$
$\bar{a}_P$	the average of momentum equation a_P coefficients on either side of face f